Deep Exclusive π^0 Electroproduction Measured in Hall A at Jefferson Lab with the Upgraded CEBAF

A dissertation presented to
the faculty of
the College of Arts and Science of Ohio University of Ohio University

In partial fulfillment
of the requirements for the degree
Doctor of Philosophy

Bishnu Karki
August 2020

This dissertation titled

Deep Exclusive π^0 Electroproduction Measured in Hall A at Jefferson Lab with the Upgraded CEBAF

by

BISHNU KARKI

has been approved for
the Department of Physics and Astronomy
and the College of Arts and Science of Ohio University by

Julie Roche
Professor of Physics and Astronomy

Florenz Plassmann
Dean, College of Arts and Sciences

ABSTRACT

KARKI, BISHNU, Ph.D., August 2020, dissertation

Deep Exclusive π^0 Electroproduction Measured in Hall A at Jefferson Lab with the Upgraded CEBAF (179 pp.)

Director of Dissertation: Julie Roche

Our understanding of the proton's structure in terms of its fundamental degrees of freedom, quarks and gluons, is incomplete. Generalized Parton Distributions (GPDs) can enhance our understanding of the partonic structure of the proton as it includes the correlation between the momentum and transverse position of partons. Exclusive electroproduction of the pion ($ep \rightarrow e'p'\pi^0$) is one of the potential channels to access the GPDs. GPDs are defined at the Bjorken limit where the total amplitude can be factorized in a hard scattering of the photon off the quark and a soft part described by the GPDs. At sufficiently high Q^2, a factorization scheme for exclusive meson production processes exists but only for longitudinally polarized virtual photons. As long as the longitudinally polarized virtual photons dominate the cross-section, we can have factorization and extract the GPDs. But the existing data for π^0 production at low Q^2 and low x_B show the dominance of transverse part of the cross-section over the longitudinal one. Some transversity GPD models have found that an effective way to factorize the contribution from transversely polarized virtual photons to explain the dominance of σ_T over σ_L, shown by existing data. The experiment E12-06-114 ran in experimental Hall A during 2014-2016. The primary goal of this experiment was to measure the DVCS cross-section but the experimental configuration also allows the measurement of deep exclusive π^0 production. Taking advantage of the upgraded CEBAF at Jefferson Lab, we explored the high Bjorken-x (0.60) and high Q^2 regime for the first time. The extracted cross-section terms for π^0 production helps us to test the validity of QCD factorization in our kinematic regime. Our π^0 production results can be used to test and improve the existing models of

proton structure. Cross-section results will be presented at two different Q^2 values for fixed x_B of 0.60.

DEDICATION

I would like to dedicate this to my lovely mom, dad and my three wonder girls.

ACKNOWLEDGMENTS

First, I would like to thank Dr. Julie Roche, my Ph.D. advisor, for her endless support, advice, and trust in me. While working with her for the past five years, I learned not only the scientific aspects but also other good aspects of decent human being. I am grateful to have her as my mentor.

I am thankful to all members of DVCS collaboration for their constant support and feedback. Being a part of DVCS collaboration, I got the opportunity to work with some wonderful physicist: Carlos Muñoz Camacho, Charles Hyde-Wright, Paul King, and Alexandre Camsonne. I have learned so many things from them which I can not express in my words. Thank you Mongi Dlamini (ECAL calibration), Frédéric Georges (HRS Optics), Alexa Johnson (R-Function), Hashir Rashad (e^- selection), Salina Ali (dead time) and Gulakshan Hamad (R-Function) for working together to achieve a common goal. I worked with Dave Mack and Thir Narayan Gautam in BCM and Unser calibration. They were terrific people, and I enjoyed working with them. I also got a chance to work with Dr. Eric Christy on Deep inelastic cross-section extraction and optics re-calibration. I admire his suggestions and time. I also would like to thank Jacob and Miranda for their help and company through my Ph.D.

I spent most of part of my Ph.D. career at Ohio University, Physics and Astronomy Department. Spending six years over here, many people either faculty or staff have directly or indirectly helped me in different aspects. Thank you all for making me feel like home. Especial thanks to Som Nath Paneru for helping me out to solve the problem in the first year and Abinash Pun for making the homely environment at the office. Help I got from all the Nepalese community (NEPSA) is much appreciated.

I want to thank my parents, who have done everything in bringing me to this stage to write this scientific paper. Special thanks to my two little princesses Aryana and Ava, for re-energizing me whenever I was exhausted. Last precious sentence for my lovely wife Sarita, for her endless support and sacrifice for making this happen.

TABLE OF CONTENTS

LIST OF TABLES

LIST OF FIGURES

INTRODUCTION

The visible matter we see around us is made up of atoms. Each atom consists of electrons orbiting around a nucleus. The atomic nucleus consists of protons and neutrons collectively known as the nucleons. When the nucleons were first discovered, they were classified as elementary particles like the electron. Later in the 1960s, Deep Inelastic Scattering (DIS) experiments confirmed that protons/neutrons are composite objects. Nucleons belong to a broader class of particles called hadrons, which are made up of quarks and gluons collectively known as partons. Quarks and gluons always stick together via the strong force to form a bound state hadron. The dynamics between quarks and gluons inside the hadron are described within the mathematical framework called Quantum Chromodynamics (QCD). QCD is not yet a fully understood theory in the sense that the QCD problem can not be solved numerically, especially at a larger distance scale (relative to proton's size). Even 100 years after the discovery of the proton, there are still open questions like, "How a proton (hadron) gets its mass from almost massless quarks and gluons?" or "From where does the total spin of the proton come from?"

The strong force has a unique aspect, which makes it more difficult to understand completely. The coupling constant of the strong force depends strongly on the energy scale of interactions. At a large energy (short distance) scale, the force between the quarks is very small, and can be treated as if free; this phenomenon is called asymptotic freedom. In this energy scale, interactions between quarks and gluons can be treated perturbatively, and hence calculations can be made from the first principles. But at small energy (larger distance about the dimension of a nucleon) scale, the force between the quarks becomes strong enough that they can not be isolated. This phenomenon is called confinement. In this regime, we cannot rely on perturbation theory. One of the best ways to understand QCD in the confinement regime is to infer from experimental results.

There are several approaches to understand the strong interaction and how its dynamics describes the observed properties in a hadron. One of them is to probe the internal structure of hadrons in terms of their fundamental degrees of freedom: quarks and gluons. So far, we have gathered different pieces of information about how partons are distributed inside the nucleon. For instance, Form Factors (FFs) give the spatial distribution of partons in the transverse plane inside the nucleon. Parton Distribution Functions (PDFs) give the longitudinal momentum distribution of partons. However, these two objects are uncorrelated and cannot provide a complete description of the nucleon. In the mid-'90s new functions called Generalized Parton Distributions (GPDs) were introduced [1–3]. GPDs contain the correlation between spatial and momentum information of a parton and give a more complete, 3-dimensional picture of a nucleon. GPDs can be experimentally accessed through deep exclusive processes like Deep Virtual Compton Scattering (DVCS) and Deep Virtual Meson Production (DVMP).

Scattering of an energetic electron beam on a nucleon target is one of the common approaches to study the internal structure of a nucleon. This is firstly because electrons are structureless, and their interaction with matter is well understood. Secondly, they can be easily produced, accelerated, and detected. The Continuous Electron Beam Accelerator Facility (CEBAF) at Jefferson Lab, Virginia, is one of the appropriate facilities for studying nucleon structure. The E12-06-114 experiment (DVCS3), the subject of this document, ran in the experimental Hall A at Jefferson Lab between Fall 2014 and Fall 2016. The main goal of this experiment was to measure the DVCS and DVMP (π^0) production cross-sections at the wide range of kinematics accessible by an upgraded CEBAF. These cross-sections will help to constraint the GPDs and thus improve our understanding of QCD. This document will be mainly focused on exclusive π^0 production, and cross-section results for one of the Bjorken x. This document is organized as follows:

- Chapter 1: This chapter is a review of the study of nucleon structure through the GPDs framework, experimental approaches, and the world GPDs program.

- Chapter 2: This chapter gives the description of the facility used by this experiment, Jefferson lab. It also describes Hall A and its standard detectors, the DVCS3 dedicated detector, and DVCS3 experimental setup.

- Chapter 3: This chapter describes the extraction of the deep inelastic scattering cross-section from the data taken concurrently to the exclusive DVCS3 data.

- Chapter 4: This chapter is the description of the analysis of the DVCS3 electromagnetic calorimeter and of the Monte Carlo simulation of the experiment based on the Geant4 toolkit.

- Chapter 5: This chapter describes the procedure adopted for the extraction of exclusive π^0 production cross-section, presents results, conclusion, and outlook.

1 NUCLEON STRUCTURE THROUGH THE ELECTROMAGNETIC PROBE

The proton and neutron are the fundamental building blocks of nuclei. Information about the distribution of quarks and gluons, the elementary particles of which nucleons are made up of, inside the nucleon can answer many fundamental questions related to nucleons' properties. Understanding the internal structure of the nucleon in terms of its basic unit, quarks and gluons, is one of the important and challenging problems in today's nuclear physics community. 3-D nucleon imaging is considered one of the top priorities that the nuclear physics community should pursue [4]. The scattering of an energetic lepton beam off the nucleon target has revealed many secrets about the nucleon. But the current information about the proton is still incomplete to fully understand the proton. In this chapter, I will focus on the electron beam to probe a proton[1].

Elastic scattering and Deep Inelastic Scattering (DIS) of the electron beam off the proton have given some insight into the partonic structure of the nucleon. However, the information that can be obtained through these scatterings is limited. Generalized Parton Distributions (GPDs) were introduced to improve our understanding of the nucleon structure. GPDs contain a wealth of information about the partons inside the nucleon. In this chapter, I will summarize what we have learned about the nucleon through Elastic scattering and DIS scattering, how much more we can learn through GPDs, and how GPDs can be experimentally accessed via deep exclusive processes. The past and future GPDs programs around the world is briefly discussed. The main focus will be given to the DVMP, especially π^0 electroproduction channel.

---

[1] alternative to an electron beam can be a muon beam.

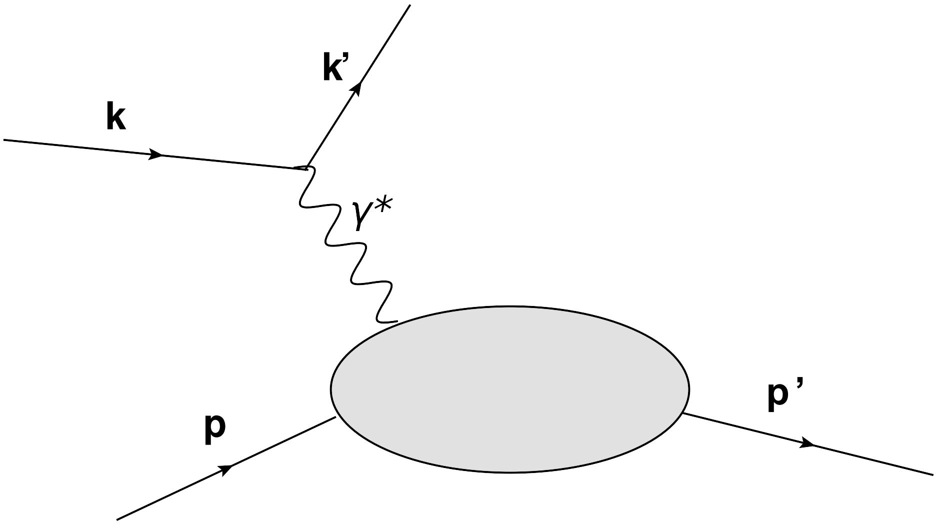

Figure 1.1: Elastic scattering off nucleon. The bold notation are four-momentum vector (E, $\vec{k}$), and the regular one refers to the magnitude of the variable.

1.1 Elastic Scattering

Elastic scattering is the process in which an electron scatters off a nucleon and the recoiling nucleon remains intact. This process is dominant at low energies and probes the global properties of nucleons, such as their charge radii.

Figure 1.1 represents the elastic scattering of the electron of the nucleon. If E and $\vec{k}$ are initial energy and momentum of incoming electron and E', $\vec{k'}$ are final energy and momentum of the scattering electron, then the kinematic variables related to elastic scattering can be defined as:

- **k**: four-momentum of beam i.e **k**($\vec{k}$, E)
- **k’**: four-momentum of scattered beam i.e. **k’**($\vec{k'}$, E')
- θ: Angle between the initial beam and scattered electron
- ν = E-E' = energy transfer

- **q**= **k** - **k'** = four-momentum of the virtual photon exchanged i.e **q** ($\vec{q}$, ν)
- Q^2 = -$\mathbf{q}^2$=virtuality or resolution of the probe = $4EE' \sin^2\left(\frac{\theta}{2}\right)$
- t = $(\mathbf{p} - \mathbf{p'})^2$ = momentum transferred to recoiled proton

Hofstadter and his team used the electron beam from Standford Linear Accelerator (SLAC) to elastically scatter off the proton. Their observation established that the proton is not a point-like object; instead, it is composite [5]. The electron-proton elastic cross-section for $Q^2 >> M_p$ (mass of the proton) can be written using the Rosenbluth formula [6] as:

$$\frac{d\sigma}{d\Omega} = \frac{\alpha^2}{4E^2 \sin^4\left(\frac{\theta}{2}\right)} \frac{E'}{E} \left(\frac{G_E^2 + \tau G_M^2}{1+\tau} \cos^2\frac{\theta}{2} + 2\tau G_M^2 \sin^2\frac{\theta}{2} \right) \tag{1.1}$$

where

$$\tau = \frac{Q^2}{4M_p^2}. \tag{1.2}$$

The finite size of a proton is taken into account by introducing two forms factors: $G_E(Q^2)$ related to the charge distribution and $G_M(Q^2)$ related to magnetic moment distribution within the proton. Sachs form factors, $G_E(Q^2)$ and $G_M(Q^2)$, can be separated by measuring the cross-section at a given Q^2 over a large range of scattering angles (θ). This method is also called Rosenbluth separation. One can also measure the ratio ($G_E(Q^2)/G_M(Q^2)$) through polarization transfer to the recoil proton. $G_E(Q^2)$ and $G_M(Q^2)$ can be parameterized by the empirically determined dipole function (G_D).

$$G_E^p(Q^2) = G_D = \frac{1}{(1 + Q^2/0.71GeV^2)^2} \tag{1.3}$$

$$G_E^p(Q^2) = \frac{G_M(Q^2)}{\mu_p} \tag{1.4}$$

where μ_p is the magnetic moment of the proton. Figure 1.2 shows the existing world data for $G_E(Q^2)$ and $G_M(Q^2)$ from e-p scattering experiments normalized to the dipole form

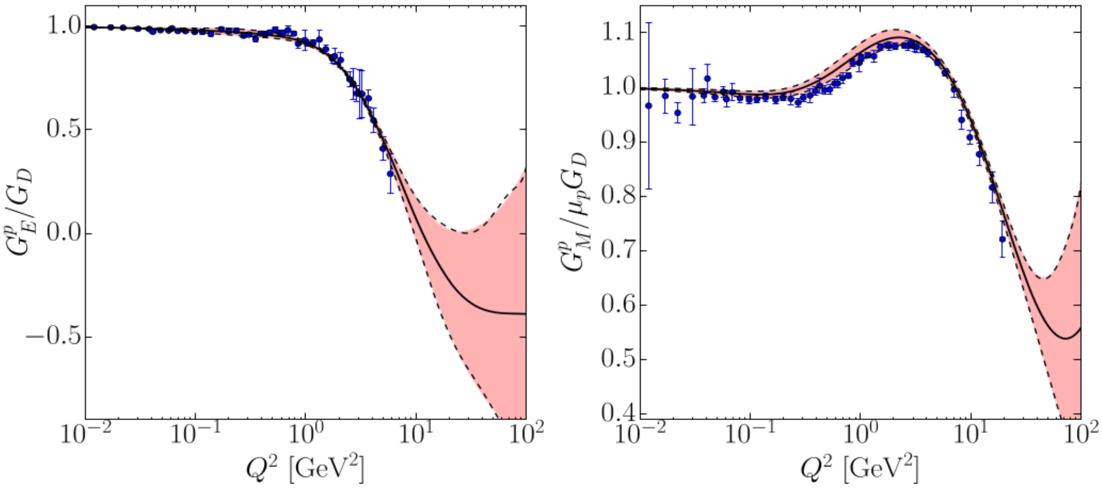

Figure 1.2: World existing data for the Sachs form factors normalized by the dipole form factor. The black line is fit performed by Ye et al. in 2018 [7]. The red shaded band indicates the systematic uncertainty. The figure is adapted from Ref. [7]. See the reuse permission in Appendix C.

factor. The uncertainties in both $G_E(Q^2)$ and $G_M(Q^2)$, grow with Q^2. The larger uncertainty at high Q^2 has generated interest in measuring the form factors at high Q^2. Currently, the data are limited to Q^2 <8 GeV^2. One of the interesting aspects of $G_E(Q^2)$ is its connection with the proton charge radius, as shown by Equation 1.5 [8]. The charge radius of a proton is still an ongoing debate in the nuclear physics community.

$$\langle r^2 \rangle = -6 \frac{dG_E(Q^2)}{dQ^2}\bigg|_{Q^2=0} \tag{1.5}$$

1.2 Deep Inelastic Scattering (DIS)

If a highly energetic electron beam is scattered off the proton, it is highly likely the proton will break up. The process in which the proton no longer remains intact is termed as DIS for e.g., $e^- p \rightarrow e^{-'} X$, where X represents the final hadronic system resulting from the break-up of the proton. Based on the final state particle detected, DIS is classified into three categories:

- Inclusive DIS: Only the scattered electron in the final state is detected
- Semi-Inclusive DIS (SIDIS): Along with the scattered electron, one of the hadrons in the final state is detected.
- Exclusive process: All the final state particles are detected.

The kinematics of the DIS process can be described by using any two of the following Lorentz-invariant quantities:

- Bjorken x (x_B): It is the fraction of momentum of proton carried by struck parton

$$x_B = \frac{Q^2}{2M_p\nu} \tag{1.6}$$

- W^2: It is the invariant mass squared of the hadronic system

$$W^2 = M_p^2 + Q^2\left(\frac{x_B}{1-x_B}\right) \tag{1.7}$$

- y: It is the fractional energy lost by an electron in scattering

$$y = 1 - \frac{E'}{E} \tag{1.8}$$

The Lorentz invariant expression for inclusive DIS cross-section ($Q^2 >> M_p^2 y$) mediated by single virtual photon can be written as:

$$\frac{d^2\sigma}{dx_B dQ^2} = \frac{4\pi\alpha^2}{Q^4}\left[(1-y)\frac{F_2(x_B,Q^2)}{x_B} + y^2 F_1(x_B,Q^2)\right] \tag{1.9}$$

where $F_1(x_B, Q^2)$ and $F_2(x_B, Q^2)$ are the structure functions such that $F_1(x_B, Q^2)$ has purely magnetic origin, while $F_2(x_B, Q^2)$ has both magnetic and electric contributions. The inclusive DIS cross-section was first measured at SLAC in the 1970s by Kendall et al. [9]. Later, a series of experiments were performed to measure the DIS structure functions. The results from these experiments revealed two interesting features of the proton:

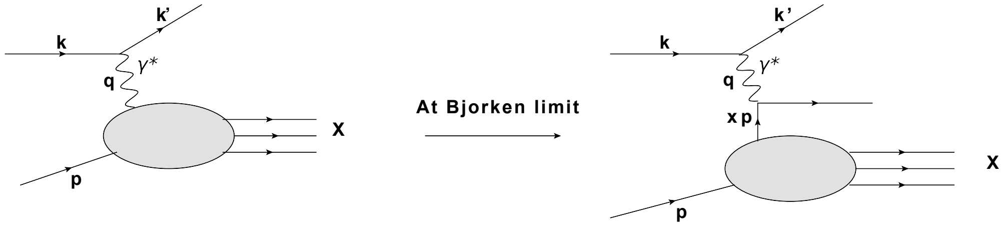

Figure 1.3: Representation of the DIS process through Feynman diagrams. At the Bjorken limit, it can be interpreted as elastic scattering off a single quark.

- Both structure functions $F_1(x, Q^2)$ and $F_2(x_B, Q^2)$ are almost independent of Q^2 at moderate values of x_B

  i.e $F_1(x_B, Q^2) \rightarrow F_1(x_B)$ and $F_2(x_B, Q^2) \rightarrow F_2(x_B)$. This observed feature was used as the basis for the idea that the proton is a composite particle consisting of point-like entities later called quarks.

- In the deep inelastic regime ($Q^2 >$ few GeV^2), $F_1(x_B)$ and $F_2(x_B)$ are related as:

  $$F_2(x_B) = 2x_B F_1(x_B) \tag{1.10}$$

  This relation is called Callan-Gross relation. It suggests that quarks are spin $\frac{1}{2}$ fermions.

1.2.1 Quark-parton model

The quark-parton model of DIS is formulated in an infinite momentum frame where the incident proton energy $E >> M_p$. In the Bjorken limit (Q^2 and ν sufficiently large), inclusive DIS can be interpreted as elastic scattering from one of the spin half quarks carrying a fraction of the momentum of the proton, as shown in Figure 1.3. The quarks inside the proton will interact with each other. The dynamics of this interacting system leads to a distribution of quark momenta within the proton. This momentum distribution is characterized by Parton Distribution Functions (PDFs). PDFs cannot yet be calculated from

QCD first principles, since the strong force coupling constant is large at a long-distance scale[2], α_s $O(1)$. At this scale, the perturbation technique can not be used. PDFs are rather extracted from the experimentally measured structure functions:

$$F_2(x_B) = x_B \sum_f e_f^2 q_f(x_B) \tag{1.11}$$

where $q_f(x_B)$ is the parton distribution function for quark of flavor f, and e is the electric charge of each quark flavor f. A proton is a dynamic system; quarks inside interact with the exchange of virtual gluons, which can fluctuate into a $q\bar{q}$ pair. Therefore the PDFs not only have the contribution from quarks (uud) for protons but also have a contribution from gluons, sea quarks, and anti-quarks. Figure 1.4 (left) is the global fit to many different experimental data at a scale of $Q^2 = 10\ GeV^2$ for quarks of flavor u, d, s, $\bar{d}$ + $\bar{u}$, $\bar{d}$ - $\bar{u}$ and gluons by the CJ collaboration [10]. It is worth noting that the gluon's contribution is very high at low x_B and small at high x_B. This is due to the fact that high momentum gluons are suppressed by the $\frac{1}{q^2}$ gluon propagator. Anti-quark and quark s contribution is relatively small at large x_B as they originate from $g \rightarrow q\bar{q}$. The difference in contributions from u and d quarks increases with x_B, which is one of the surprising facts. The spin information is encoded in the polarized PDFs, which can be extracted from polarized DIS cross-section data. Figure 1.4 (right) shows the polarized PDFs for the proton. The polarized PDFs have larger uncertainty due to limited polarized data. The striking outcome of polarized PDFs analysis is that the total contribution from valence quarks[3] to the proton's spin is only 33% ±3% (Stat.) ±5% (Syst.) [11]. The total contribution to the proton's spin from sea quarks, gluons, and valence quarks do not add up to spin $\frac{1}{2}$ (the proton spin). This result has attracted a lot of attention to the orbital angular momentum of quarks and gluons, which have not been measured so far.

---

[2] compared to dimension of a proton

[3] in figure represented by subscript v

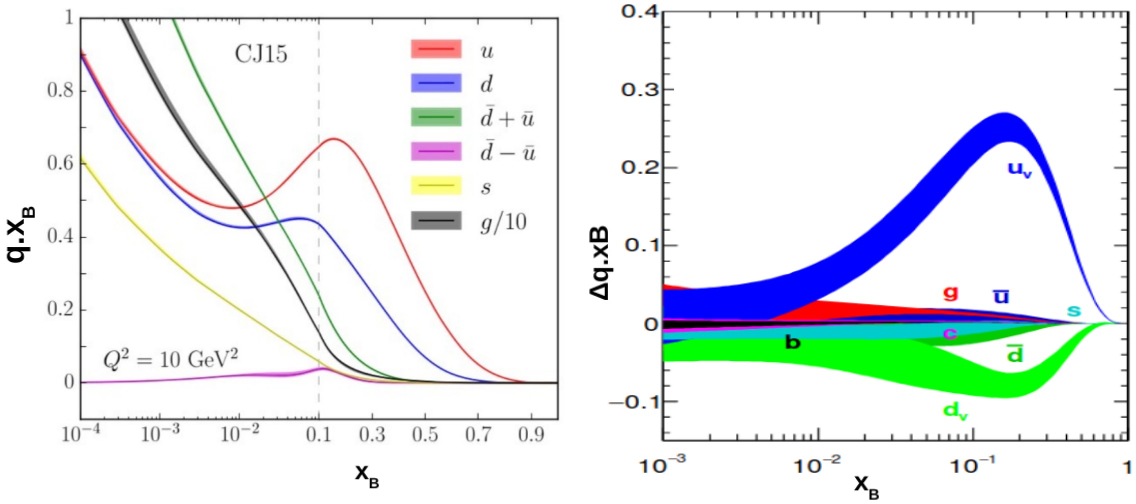

Figure 1.4: Extracted unpolarized and polarized proton's PDFs from a global analysis of world data. Left: Contribution from different flavors of quarks and anti-quarks to the proton's PDFs. The flavor decomposition is extracted with a global analysis of unpolarized DIS data [10]. Right: The spin-dependent or polarized PDFs for different quarks flavor in a proton. The polarized PDFs were extracted using world polarized data from pp collision and ep scattering [12]. See re-use permission (1) in Appendix C.

1.3 Generalized Parton Distribution Functions (GPDs)

FFs and PDFs discussed in section 1.1 and 1.2, respectively provide the microscopic structure of the nucleon. Both FFs and PDFs contain limited information about the partons inside the nucleon. FFs do not contain any dynamical information of partons. On the other hand, PDFs tell nothing about the spatial distribution of quarks. A complete picture of a nucleon lies in the correlation between space and momentum coordinates. In 1932, Wigner proposed a distribution, which is a function of both space and momentum coordinates [13]. These distributions have been used in various areas like signal analysis, quantum information, optics, image processing, etc. [14]. Later, the concept of a Wigner distribution was introduced in QCD, and a more natural interpretation in the infinite momentum frame was given by Lorce and Pasquini [15]. Its matrix elements describe the 5-dimensional distribution of partons (3 in momentum and 2 in position). The Wigner distribution is regarded as the "mother distribution," as it contains a full correlation between partons transverse position and momentum in a single distribution. However, no process has been realized yet to extract the Wigner distributions. Instead, a lot of experimental efforts are made to measure some special cases of the Wigner distributions like Transverse Momentum Distributions (TMDs) [16, 17] and Generalized Parton Distributions (GPDs). The experimentally extracted observables can be related to GPDs and TMDs. GPDs give the 3-D image of the nucleon in impact parameter space, while TMDs give in momentum space. Figure 1.5 shows the connections between different distribution (GPDs, FFs, TMDs, PDFs) with the Wigner distribution. In this document, I will focus on Generalized Parton Distributions (GPDs) only.

In the mid-'90s, a new formalism called Generalized Parton Distributions was introduced for describing the internal structure of the nucleon [1–3]. GPDs encapsulate the correlation between the spatial distribution and momentum distribution of quarks inside a nucleon. In an infinite momentum frame, GPDs give the distribution of partons in the transverse plane for a given longitudinal momentum of a parton.

1.3.1 Experimental access to GPDs and factorization

GPDs can be accessed experimentally through a suitable exclusive process like Deep Virtual Compton Scattering (DVCS) or Deep Virtual Meson Production (DVMP). These exclusive processes can be represented by the so-called "handbag diagram." The handbag diagrams for DVCS and DVMP processes at leading order and leading twist (twist/higher-order will be discussed in section 1.3.2) are shown in Figure 1.6. In this formalism, the virtual photon scatters off a single parton inside a nucleon. The kinematic variables involved in these processes are defined below:

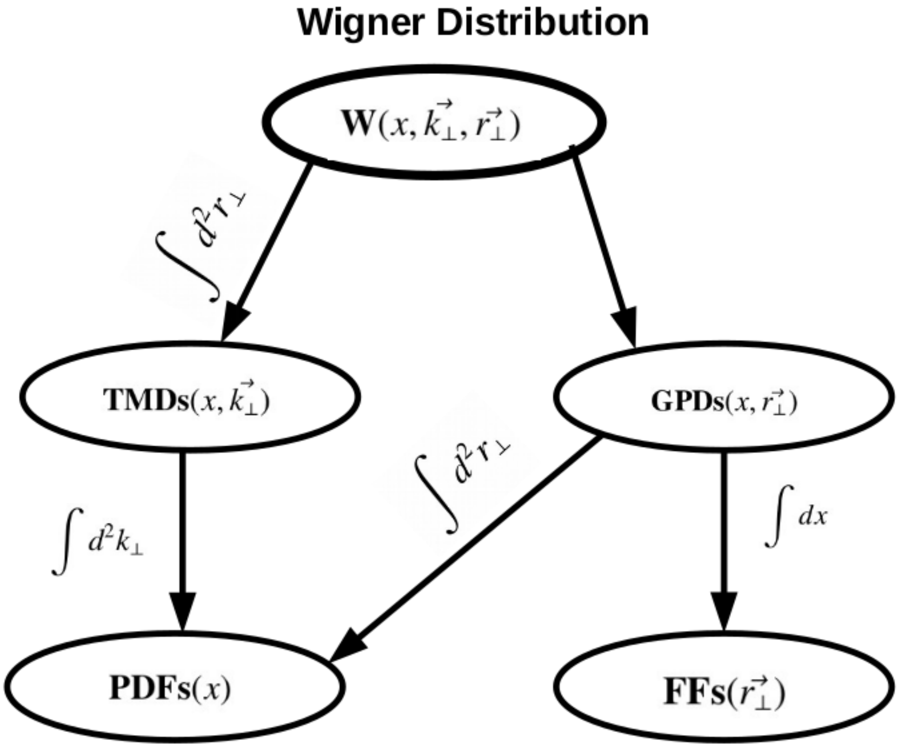

Figure 1.5: Projection of Wigner distribution on different phase space [18]. Here x is a fraction of nucleon's momenta carried by struck quark, $r_\perp$ is a transverse position coordinate, and $k_\perp$ is transverse momentum coordinate.

- **k**, **k'**, **p**, and **p'** : Same as in section 1.1.
- x: The longitudinal momentum fraction of the proton carried by a struck quark
- ξ : The longitudinal fraction of momentum transfer to the nucleon $\xi \cong \frac{x_B}{2-x_B}$
- t: Squared of 4-momentum transfer to the proton (its Fourier conjugate is an impact parameter ($r_\perp$) i.e,
  t= $-\Delta^2 = (\mathbf{p}' - \mathbf{p})^2$

For DVCS (ep→ $e'p'\gamma$), the incoming electron gets scattered, emitting a virtual photon of virtuality Q^2. The virtual photon is then absorbed by a quark inside the nucleon with

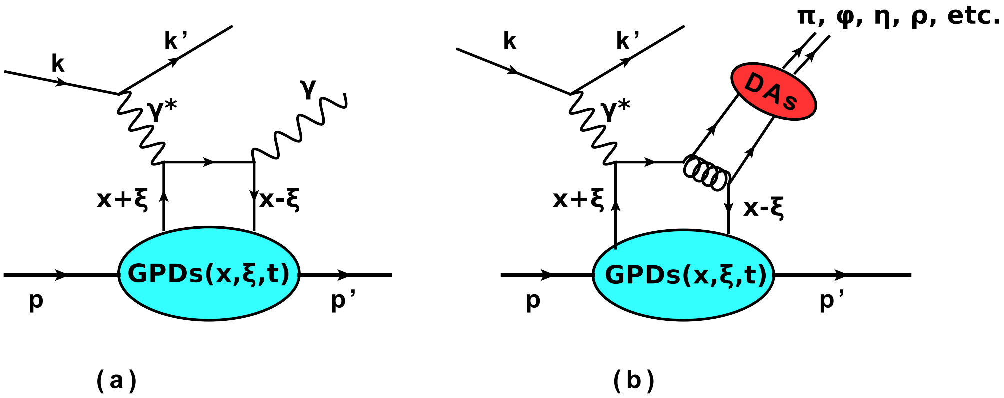

Figure 1.6: Handbag representations for exclusive processes at leading order and a leading twist [19]. On the left (a) is a handbag diagram for the DVCS process and on right (b) is for DVMP.

a momentum fraction $x + \xi$ of a nucleon. The struck quark is later reabsorbed by the nucleon with different momentum fraction $x - \xi$. This is possible due to the emission of a real photon in the final state. In the case of DVMP instead of a real photon, a meson is produced in the final state, leaving the nucleon intact in both of the processes. In the DVMP, there is an additional strong vertex due to meson production. This additional non-perturbative object describes the structure of the produced meson, called the Distribution Amplitudes (DAs) [19]. For both DVCS and DVMP, the handbag diagram consists of two distinct processes, a short-distance/hard process and a long-distance/soft process.

At the Bjorken limit,

$$\left.\begin{aligned} Q^2 &\to \infty \\ \nu &\to \infty \end{aligned}\right\} \text{at} \quad \text{fixed} \quad \mathrm{x_B} \tag{1.12}$$

the handbag diagram shown in 1.6, can be factorized into two parts: a hard perturbative and a soft non-perturbative part [20] [21]. The hard part can be analytically calculated from the first principles. The soft part contains the hadron structure and can be parametrized by the GPDs. But in the case of DVMP, factorization only holds for the longitudinally

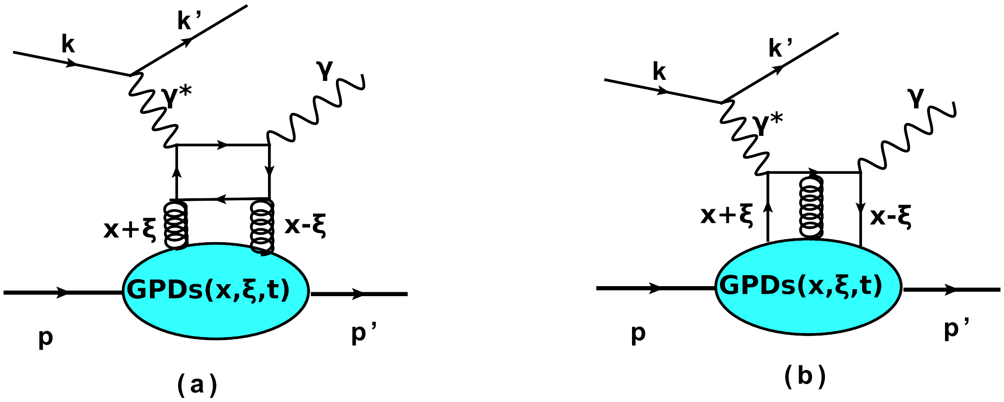

Figure 1.7: Higher-order and higher twist handbag diagram for DVCS process. On the left (a) is the higher-order, and on the right (b) is a higher twist-3.

polarized virtual photons but not for transverse polarization. In GPDs formalism, the nucleon structure is parametrized by eight sets of GPDs, which are a function of 3 variables x, ξ, and t. Each GPD describes a unique process based on quark-nucleon helicity.

1.3.2 Higher-twist/higher-order

The first approach to solve any scattering processes using perturbation theory is to solve the Feynman diagram at tree-level. But in most cases, tree-level or leading-order diagrams are not enough to describe the full experimental process. So one has to add corrections from higher-order diagrams. The strong coupling constant α_s strongly depends on Q^2, so one can use a perturbation treatment only when $\alpha_s << 1$. Contributions from higher level-diagrams to the amplitude goes on decreasing as the power of α_s in the perturbative regime. A second-order diagram for the DVCS process is shown in Figure 1.7a, where the virtual photon absorbs a quark/anti-quark produced from the splitting of gluon (g→ q$\bar{q}$) and is reabsorbed by the nucleon.

The DVCS (DVMP) amplitude consists of both hard perturbative and soft non-perturbative parts. As in the perturbative part, a higher-order correction has to be made in the non-perturbative part, to describe the full experimental process. For this one can use the Operator Product Expansion (OPE) to expand the product of two operators as the sum of local operators at different positions. Then one can introduce "twist" to sort out the terms according to the magnitude of contributions to the soft process. The twist is a difference in mass dimension and spin. Leading twist (twist-2) has the highest contribution to the scattering amplitude. Contributions of twist-3 in the scattering amplitude are suppressed by a factor of $\frac{1}{Q}$ relative to leading twist likewise twist-4 by a factor of $\frac{1}{Q^2}$ and so on. Figure 1.7b shows a higher twist diagram for the DVCS process where the struck quark interacts with other quarks before getting reabsorbed. The higher-order or higher-twist has a relatively lower contribution as compared to leading order/leading twist. But depending on the Q^2 the probe, one needs to take into account those contributions. In the Q^2 regime accessible at Jefferson Lab, before the 12 GeV upgrade, a significant contribution from the lowest twist/order was reported by M. Defurne et al. [22]. The same result also showed a sizable contribution either coming from a higher twist or next to leading order. Their formalism was unable to distinguish between higher twist vs. next to leading order contributions.

1.3.3 GPDs nomenclature

The DVCS is regarded as one of the cleanest processes to access the GPDs because it involves only one non-perturbative object, which makes this process theoretically less challenging. In the valence regime, at leading twist and leading order, the DVCS is sensitive to 4 sets of chiral even GPDs for each quark flavor f: $\mathrm{H}_f(\mathrm{x}, \xi, \mathrm{t})$, $\mathrm{E}_f(\mathrm{x}, \xi, \mathrm{t})$, $\widetilde{H_f}(\mathrm{x}, \xi, \mathrm{t})$, and $\widetilde{E_f}(\mathrm{x}, \xi, \mathrm{t})$. Figure 1.8 is a classification of chiral even GPDs based on the quark-nucleon helicity [23]. GPDs H and E are averages over quark helicities[4], also called "unpolarized"

---

[4] the subscript f is dropped off for simplicity but in practice we have GPDs for each quark flavor f

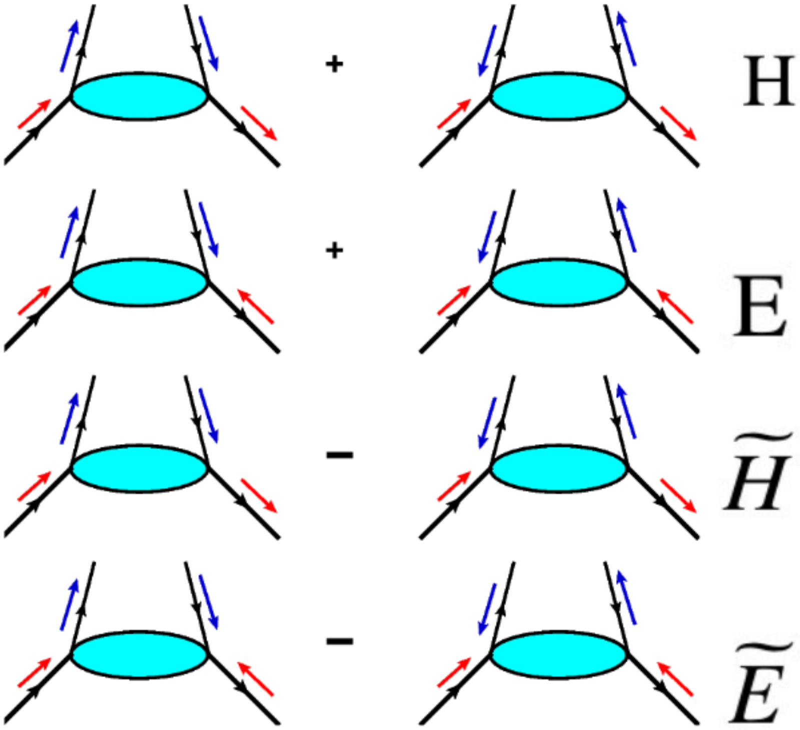

Figure 1.8: Definition of GPDs based on quark-nucleon helicity state [23]. The red arrows represent the nucleon spin while the blue arrows are of the struck quark helicity.

GPDs. GPDs $\widetilde{H}$ and $\widetilde{E}$ are the difference between quark helicities, also called “polarized” GPDs. The GPDs E and $\widetilde{E}$ do not conserve the nucleon spin, but H and $\widetilde{H}$ do.

1.3.4 Compton form factors

GPDs depend on the three variables: x, ξ, and t. The variables ξ and t can be accessed by measuring the kinematics of the scattered electron and the final state photon/proton, but the variable x is not experimentally accessible. Therefore, GPDs are not directly accessible from the experiment. Instead, we measure Compton Form Factors (CFFs), which are a function of ξ and t only. The GPD H_f of quark flavor f is connected to CFFs $\mathcal{H}_f(\xi, t)$ as:

$$\mathcal{H}_f(\xi, t) = \mathcal{P}\int_{-1}^{1} \frac{H_f(x, \xi, t)}{\xi - x} dx - i\pi H_f(\xi, \xi, t) \tag{1.13}$$

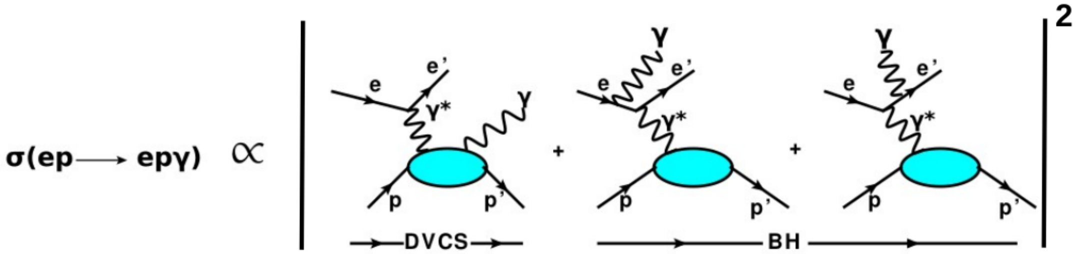

Figure 1.9: Contribution to the ep → $ep\gamma$ from DVCS and the Bethe-Heitler processes. In DVCS (left most), the photon is radiated from proton, while in Bethe-Heitler (two figures on right), the photon is either radiated from an the incoming or outgoing electron.

where $\mathcal{P}$ is the principal value integral. For each GPD, there are two (real + imaginary) CFFs that can be accessed through the DVCS cross-section. The dispersion relation connects the real and imaginary part of CFFs as:

$$Re\mathcal{H}(\xi,t) = \mathcal{P}\int_{-1}^{1} dx \frac{Im\mathcal{H}(\xi,t)}{\xi - x} + D(t) \tag{1.14}$$

where the D-term D(t) is given as:

$$D(t) = \frac{1}{2}\int_{-1}^{1} \frac{D(z,t)}{1-z} dz \tag{1.15}$$

$$D(z,t) = (1-z^2)\left[d_1(t) C_1^{3/2}(z)\right] \tag{1.16}$$

such that, -1 < $z = \frac{x}{\xi}$ <1. The D-term is related to the Gravitational Form Factor $d_1(t)$ through a Gegenbauer coefficient $C_1(z)$. The D-term is interpreted in terms of shear force and pressure inside the nucleon in the infinite momentum frame [24].

1.3.5 Accessing GPDs from DVCS

Experimentally the photo-electroproduction (ep → $ep\gamma$) process is measured. This channel has a contribution from two experimentally indistinguishable processes: DVCS and Bethe-Heitler (BH). Figure 1.9 (left) shows the DVCS process where the photon is

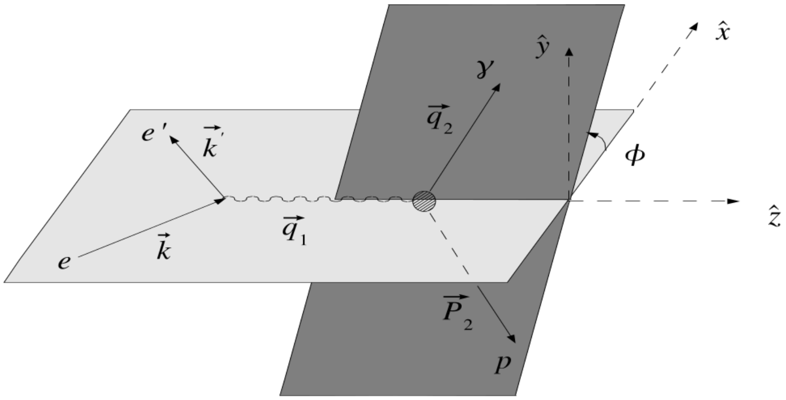

Figure 1.10: Kinematics for electroproduction of photon in the target rest frame. The azimuthal angle ϕ is the angle between the electron scattering plane and the hadronic production plane. This figure is adapted from Ref. [26]. See the re-use permission in Appendix C.

radiated from the proton and the BH process (right two) where the photon is either radiated by an incoming or outgoing electron. The 5-fold differential cross-section for photon-electroproduction can be written as [25]:

$$\frac{d^5\sigma}{dQ^2 dt dx_B d\phi_e d\phi} = \frac{\alpha^3 x_B y}{16\pi^2 Q^2 \sqrt{1 + 4x_B^2 M^2/Q^2}} \mid \frac{\mathcal{T}}{e^3} \mid^2 \tag{1.17}$$

where angle ϕ_e is electron azimuthal angle with respect to the horizontal plane around the beamline direction, ϕ is the angle between leptonic and hadronic planes. Figure 1.10 shows the definition of angle ϕ as by the Trento Convention [26]. The total amplitude ($\mathcal{T}$) is the sum of the DVCS ($\mathcal{T}_{DVCS}$) amplitude, the BH amplitude ($\mathcal{T}_{BH}$), and the interference between these two processes ($\mathcal{I}$).

$$\mid \mathcal{T} \mid^2 = \mid \mathcal{T}_{DVCS} \mid^2 + \mid \mathcal{T}_{BH} \mid^2 + \mathcal{I} \tag{1.18}$$

where interference term can be written as

$$\mathcal{I} = \mathcal{T}^{\dagger}_{DVCS}\mathcal{T}_{BH} + \mathcal{T}^{\dagger}_{BH}\mathcal{T}_{DVCS}. \tag{1.19}$$

The ϕ dependence of the electroproduction cross-section can be exploited to expand each term $\mathcal{T}_{DVCS}$, $\mathcal{T}_{BH}$, and $\mathcal{I}$ as a harmonic in ϕ. Harmonic expansion up to twist 3 terms is developed by Belitsky and collaborators [25].

1.3.6 Bethe-Heitler term

Bethe-Heithler is a purely electromagnetic process and can be computed from the existing knowledge of electromagnetic FFs. By using the FF parametrization proposed by Kelly [27], the BH contribution can be computed within 1% precision for the kinematic setting of this experiment. Its harmonic expansion on ϕ can be written as:

$$\mid \mathcal{T}_{BH} \mid^2 = \frac{e^6}{x_B^2 y^2 (1+\epsilon^2)^2 \Delta^2 \mathcal{P}_1(\phi)\mathcal{P}_2(\phi)} \left\{ C_0^{BH} + \sum_{n=1}^{2} C_n^{BH} cos(n\phi) + \mathcal{S}_1^{BH} sin(\phi) \right\} \tag{1.20}$$

where $\mathcal{P}_1(\phi)$ and $\mathcal{P}_2(\phi)$ are lepton propagators. Further details can be found in Appendix A.

1.3.7 DVCS term

The harmonic expansion of DVCS term can be written as:

$$\mid \mathcal{T}_{DVCS} \mid^2 = \frac{e^6}{y^2 Q^2} \left\{ C_0^{DVCS} + \sum_{n=1}^{2} \left[C_n^{DVCS} cos(n\phi) + \mathcal{S}_n^{DVCS} sin(n\phi) \right] \right\} \tag{1.21}$$

The harmonic coefficients C_i^{DVCS} and $\mathcal{S}_i^{DVCS}$ are connected to the bi-linear combinations of CFFs [28]. The connection is shown in detail in Appendix A.

1.3.8 Interference term

The interference between DVCS and BH process can be written as:

$$\mathcal{I} = \frac{\pm e^6}{x_B y^3 \Delta^2 \mathcal{P}_1(\phi)\mathcal{P}_2(\phi)} \left\{ C_0^{I} + \sum_{n=1}^{3} \left[C_n^{I} cos(n\phi) + \mathcal{S}_n^{\mathcal{I}} sin(n\phi) \right] \right\} \tag{1.22}$$

where +(-) case stands for negatively (positively) charged lepton beam. The harmonic coefficients of interference terms can be written as a linear combination of CFFs [28].

1.3.9 Properties of GPDs

There are many properties of GPDs which make them exciting subjects in the nuclear physics community. Some of those interesting properties will be discussed in this section.

1. Nucleon tomography: GPDs allow simultaneous measurement of the longitudinal momentum and transverse position (impact parameter) distribution of partons inside the nucleon. The set transverse position representation at different longitudinal momentum provides a tomographic image of the nucleon, as represented in Figure 1.11. The probability density of finding a parton of flavor f, with longitudinal momentum fraction x with respect to its transverse distance $b_\perp$ is given by

   $$q^f(x, \vec{b_\perp}) = \int \frac{d^2 q_\perp}{(2\pi)^2} e^{i\vec{q_\perp}\vec{b_\perp}} H_f(x, -\vec{q_\perp}^2) \tag{1.23}$$

   where $\vec{q_\perp}$ is transverse momentum transfer.

2. Connection to PDFs and FFs: GPDs can be regarded as the generalized form of PDFs and FFs. In a forward limit, t → 0 and $\xi \to 0$, GPDs reduce to PDFs,

   $$\begin{aligned} H^f(x, 0, 0) &= q_f(x) \\ \widetilde{H}^f(x, 0, 0) &= \Delta q_f(x) \end{aligned} \tag{1.24}$$

   where f is a flavor of quark and $q_f(x)$ and $\Delta q_f(x)$ are unpolarized and polarized quark densities. The GPDs E and $\widetilde{E}$ do not have any connection to PDFs which makes them even more interesting.

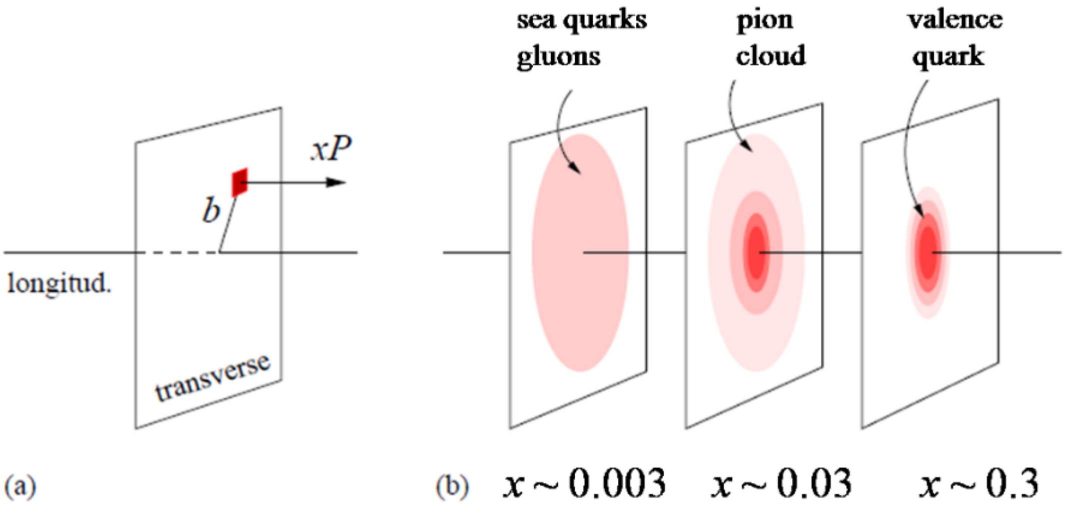

Figure 1.11: Cartoon showing the sketch of the tomographic view of the transverse spatial parton distribution for the given longitudinal momentum fraction x. The figure is adapted from Ref [29]. See the re-use permission in Appendix C.

The first moments of GPDs are related to the FFs [30] as :

$$\begin{aligned} \int_{-1}^{1} H^f(x,\xi,t)dx &= F_1^f(t) \\ \int_{-1}^{1} E^f(x,\xi,t)dx &= F_2^f(t) \\ \int_{-1}^{1} \widetilde{H}^f(x,\xi,t)dx &= G_A^f(t) \\ \int_{-1}^{1} \widetilde{E}^f(x,\xi,t)dx &= G_p^f(t) \end{aligned} \tag{1.25}$$

where $F_1^f(t)$, $F_2^f(t)$, $G_A^f(t)$, and $G_p^f(t)$ are Dirac, Pauli, axial, and pseudoscalar form factors respectively. As PDFs and FFs are well known, the above connections between GPDs and FFs/PDFs are crucial to test the measured GPDs.

3. Connection to the orbital angular momentum of quarks: Spin is regarded as a fundamental quantity in quantum physics. The total nucleon's spin can be written

as the sum of the contribution from gluon and quarks. However, the measured contribution to the proton's spin from the quarks and gluons spin do not add up to total proton's spin. The observed spin crisis in the proton is famously known as the "spin crisis" [31].

$$\frac{1}{2} = \underbrace{\frac{1}{2}\Delta\Sigma + L_q}_{J^q} + J_g$$

where J_q and J_g are the total angular momentum of quarks and gluons respectively, L_q is the orbital angular momentum of quarks, and $\frac{1}{2}\Delta\Sigma$ is the sum of the intrinsic spin of quarks, which is measured to be around 33 ±6% of the total spin of proton [11]. Through the Ji's sum rule [1], the total contribution from the quarks can be related to the GPDs as:

$$J^q = \int_{-1}^{1} x[H^f(x,\xi,0) + E^f(x,\xi,0)]dx \tag{1.26}$$

Knowledge of GPDs can play a crucial role in extracting the contribution of orbital angular momentum of quarks to the proton spin. The orbital angular momentum of quarks has not been measured so far and can be a significant step toward solving the proton spin puzzle. One of the top priorities for the future accelerator facility, the Electron-Ion Collider, is to study the orbital angular momentum of quarks and gluons [32].

4. Connection to mechanical properties: GPDs indirectly allow accessing the basic mechanical properties of the nucleon like shear force and the pressure distribution inside a proton [33]. The Gravitational Form Factor (GFF) which encodes the shear force on quarks and pressure distribution in a proton is connected to GPDs as:

$$\int_{-1}^{1} xH(x,\xi,t)dx = M_2(t) + \frac{4}{5}\xi^2 d_1(t) \tag{1.27}$$

where $M_2(t)$ and $d_1(t)$ are components of the energy-momentum tensor. The GFF $d_1(t)$ is connected to D-term as described in Equation 1.15 and 1.16. Burkert

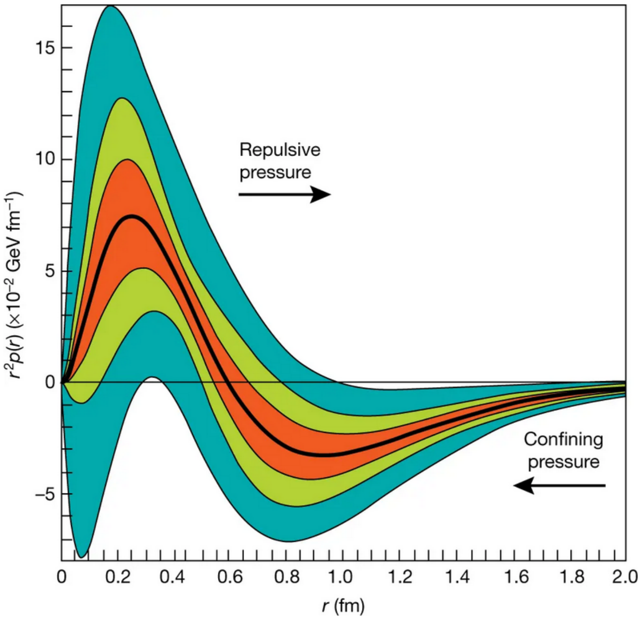

Figure 1.12: The pressure distribution inside the proton as a function of distance from the center of proton. The black line corresponds to the extracted pressure from the D-term with the estimated uncertainties represented by the light green shaded region. The blue shaded region shows the uncertainty without JLab 6 GeV data, and the red shaded region shows the projected uncertainty from future experiments at 12 GeV. The figure is taken from Ref. [33]. See the re-use permission in Appendix C.

et al. [33] recently measured the pressure distribution inside the proton using the GPD data. Their measurement has opened a new area of research on fundamental gravitational properties of subatomic particles through the electromagnetic probe. However, their result is subjected to large systematic and simplifying assumptions. Figure 1.12 shows the quarks pressure distribution inside the proton obtained in this analysis. Burkert et.al. found the strong repulsive pressure near the center of the proton (up to 0.6 fm) and binding pressure at a larger distance from the center of the proton.

1.3.10 Deep virtual meson production

The Deep Virtual Meson Production (DVMP) process at leading twist and leading order can be represented by a handbag diagram shown in Figure 1.6b. In this process, the struck quark hadronizes before getting reabsorbed. The final stage of this process is a recoiling nucleon, a scattered electron, and one of the mesons ($\pi^{\pm}$, π^0, ϕ,η, etc.). The structure of the nucleon is encoded by GPDs, which is in the soft part of the handbag diagram. GPDs are universal, irrespective of the process used for extraction. Theoretically, DVMP is challenging due to the presence of one additional soft part from hadronization. The meson structure is described by Distribution Amplitudes (DAs), and we have very limited information about DAs to date [34]. The DVMP allows accessing the chiral odd GPDs. Chiral odd or Transversity GPDs describe the processes where a quark helicity is flipped, and these GPDs cannot be accessed through the DVCS process at leading order. So far, existing experimental knowledge about the chiral odd GPDs is limited, as the quark helicity flipping processes are suppressed. For each of the chiral even GPDs described in Figure 1.8 there is a corresponding chiral odd GPD namely: $H_T(x,\xi,t)$, $E_T((x,\xi,t)$, $\widetilde{H}_T(x,\xi,t)$, $\widetilde{E}_T(x,\xi,t)$.

The cross-section for exclusive meson production can be written as [35]:

$$\begin{aligned}\frac{d^4\sigma}{dQ^2dx_Bdtd\phi} &= \frac{1}{2\pi}\Gamma_\gamma(Q^2,x_B,E)\left[\frac{d\sigma_{\mathrm{T}}}{dt}+\epsilon\frac{d\sigma_{\mathrm{L}}}{dt}+\sqrt{2\epsilon(1+\epsilon)}\frac{d\sigma_{\mathrm{TL}}}{dt}\cos(\phi)\right. \\ &\left.+\epsilon\frac{d\sigma_{\mathrm{TT}}}{dt}\cos(2\phi)+h\sqrt{2\epsilon(1-\epsilon)}\frac{d\sigma_{\mathrm{TL'}}}{dt}\sin(\phi)\right]\end{aligned} \tag{1.28}$$

where h (=±1) is the helicity of the lepton probe. For the unpolarized case, h=0 the last term can be dropped out from Equation 1.28. Γ_γ is virtual photon flux intensity,

$$\Gamma_\gamma(Q^2,x_B,E)=\frac{\alpha}{8\pi}\left(\frac{1-\epsilon}{\epsilon}\right)\left(\frac{1-x_B}{x_B^3}\right)\left(\frac{Q^2}{M_p^2E_0^2}\right) \tag{1.29}$$

and ϵ is degree of polarization

$$\epsilon = \frac{1 - y - \frac{Q^2}{4E_0^2}}{1 - y + \frac{y^2}{2} + \frac{Q^2}{4E_0^2}} \tag{1.30}$$

The cross-section terms σ_{L} is the contribution from the longitudinal polarized virtual photon, σ_{T} is the contribution from the transversely polarized virtual photon, σ_{TL} is the interference between longitudinal and transversely polarized virtual photon, σ_{TT} is transverse-transverse interference, and $\sigma_{\mathrm{TL'}}$ is the polarized cross-section term. For DVMP, the factorization is only established for longitudinally polarized virtual photons but not for the transverse polarization [36]. In the regime where the leading twist handbag formalism is applicable, QCD factorization predicts that the σ_{L} scales as Q^{-6} and σ_{T} as Q^{-8} [20]. At sufficiently high Q^2, the transverse contribution could be neglected. But the minimum value of Q^2 at which this prediction holds must be tested through experiments. However, the existing data for meson production measured at different facilities suggest that transversely polarized virtual photons have a significant contribution to the total cross-section [37] [38] for the Q^2 between 1.5 to 2 GeV^2. For instance, Figure 1.13 is the L/T separated cross-section data for deep exclusive π^0 production from Hall A Jefferson Lab [37] showing a dominance of σ_{T} over σ_{L}. Currently the available data are limited to a small range of Q^2 ranging (1.5 -2 GeV^2) and at a fixed value of Bjorken-x (x_B=0.36). Experiment E12-06-114 aims to expand the π^0 data to higher Q^2 and high x_B and test the QCD factorization prediction.

The observed dominant contribution of σ_{T} opens new and unique opportunities to access the transversity GPDs of the nucleon. On the theory aspect, some advancement has been made to factorize the transverse amplitude in meson production. It has been suggested in Goldstein Hernandez and Luiti (GL) [39] and Goloskokov and Kroll (GK) [40] models that the observed large cross-section for σ_{T} relative to σ_{L} can be explained by the coupling of twist 3 DA with the transversity GPDs of the proton without violating the factorization theorem. These transversity GPD models introduce the chiral odd GPDs to explain the experimentally observed contribution from transversely polarized virtual photons as:

$$\frac{d\sigma_T}{dt} = \frac{4\pi\alpha}{2k'Q^4}\left[(1-\xi^2)\,|\langle \widetilde{H}_T\rangle|^2 - \frac{t'}{8M_P^2}\,|\langle \widetilde{E}_T\rangle|^2\right] \tag{1.31}$$

$$\frac{d\sigma_{TT}}{dt} = \frac{4\pi\alpha}{k'Q^4}\frac{t'}{16M_P^2} - |\langle \widetilde{E}_T\rangle|^2 \tag{1.32}$$

But Goldstein, Hernandez and Luiti (GL) and Goloskokov and Kroll (GK) uses different parameterization of the GPDs. For instance, Goloskokov and Kroll uses double distribution representation for GPDs [40] while GL model uses experimental evidence to constrain the various theoretical aspects of GPDs [39]. Different meson productions (π^+, π^0..) exhibit the sensitivities to different sets of GPDs. For instance, π^0 production is sensitive to H_T and $\widetilde{E_T}$. Transversity based GPDs models are able to explain the extracted σ_T and σ_L fairly well (see Figure 1.13). This agreement between data and model is one of the motivations to test these models over a wide range of kinematic that can be accessed with an upgraded e^- beam facility at Jefferson Lab.

Depending on the meson produced, the final state can have different quarks in combination. This feature allows one to disentangle the various flavor of GPDs. Due to a relatively larger cross-section for exclusive vector mesons, it is mostly studied experimentally as compared to pseudoscalar meson production. Vector meson production at leading order is primarily sensitive to the gluon chiral even GPDs [34]. This document is focused on the exclusive pseudoscalar meson production, more specifically, π^0 production. In exclusive π^0 production ($ep \to e'p'\pi^0$), the quark helicity flipping amplitude is relatively larger than the quark helicity conserving amplitude [35]. Due to this fact, the exclusive π^0 production channel is more sensitive to transversity GPDs. This fact makes this channel suitable for studying the transversity GPDs. Moreover, the π^0 channel does not have pion pole contributions like in $\pi^\pm$, hence data interpretation is relatively easy. Despite its significance, π^0 cross-section data are not available over a large kinematic range mainly due

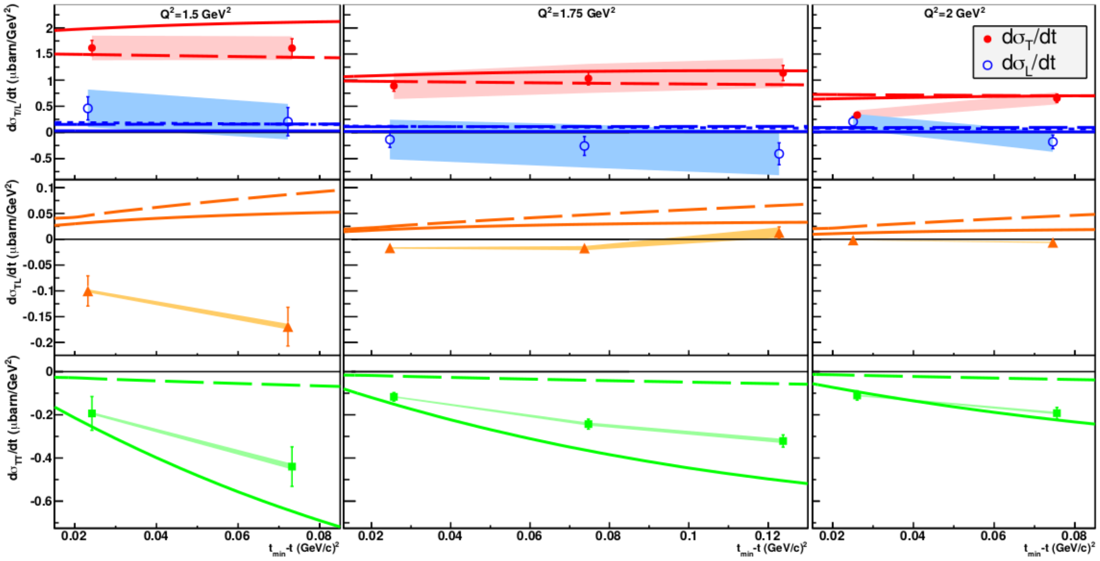

Figure 1.13: Different cross-section terms σ_{T}, σ_{L}, σ_{TT}, and σ_{TL} for π^0 electroproduction measured at Hall A. This measurement shows the dominance of σ_{T} over σ_{L} for 3 different Q^2 (1.5, 1.75, and 2 GeV^2) and at fixed x_B of 0.36. The prediction from different transversity GPDs models full line from [40] and dashed lines from [39] are in fair agreement with data. The figure was adapted from [37]. See the re-use permission in Appendix C.

to two reasons: the cross-section is relatively low as compared to π^+, and clean detection of π^0 requires the measurement of two decayed photons.

The current goal for exclusive π^0 production is to measure the cross-section over a wide kinematic range and test the validation of the existing transversity GPDs models by comparing cross-section data with model predictions. The document reports exclusive π^0 production cross-section at high Q^2(5.4 and 8.4 GeV^2) at fixed x_B of 0.60, exploiting the upgraded e^- beam facility at Jefferson Lab. The extracted cross-sections are compared with the Goloskokov and Kroll (GK) [40] GPDs model for the first time in this kinematic regime[5].

1.3.11 Experimental status

Since the connection of GPDs with deep exclusive processes was found, several experimental efforts have been made, and several are ongoing to extract the GPDs. As DVCS is one of the cleanest channels to extract the GPDs, most of the experimental efforts are focused on it. To extract the GPDs, several observables have to be measured with the polarized/unpolarized beam, positively/negatively charged beam, and different target polarization at the different kinematic regimes. For measurement of various observables related to GPDs, an extensive GPDs program has been planned. Figure 1.14 shows the kinematic coverage of the worldwide DVCS program. Most of the meson production experiments ran or will be running contemporaneously with the DVCS experiments. Further detailed information about the past and future GPDs program can be found in the review article by N.d'Hose [41]. In this section, I will describe various experimental programs to measure the GPDs through DVCS and DVMP.

1.3.11.1 H1 and ZEUS

The H1 and ZEUS collaborations measured the beam charge asymmetries exploiting the positron and electron beam at high energy (30 < W < 140 GeV) , over a Q^2 range, $2 < Q^2 < 100$ GeV^2. They used the 820 GeV proton beam from HERA (Hadron-Elektron-Ring-Anlage) accelerator facility to collide with electron/positrons with energy of 27.5 GeV. H1 and ZEUS collaboration [43, 44] measured the total DVCS cross-section dependence on different kinematic variables like Q^2, W^2, and t.

H1 and ZEUS also measured the vector meson production (ρ, ϕ, J/ψ, ω) cross-section as a function of Q^2, W and t over a wide range of kinematics [45] [46] [47].

---

[5] Goldstein Hernandez and Luiti (GL) [39] and Goloskokov model calculations are pending

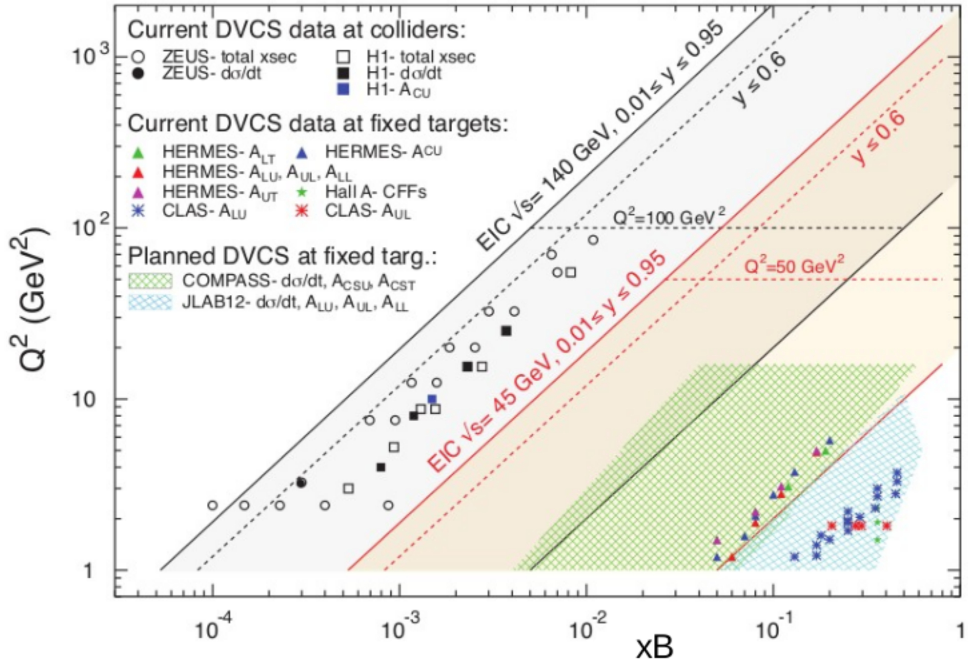

Figure 1.14: Kinematic coverage in x_B and Q^2 for past and future GPDs experiments around the world. The figure is taken from Ref. [42]. See the re-use permission in Appendix C.

Their measurement covers a wide kinematic range from threshold up to W~200 GeV and 0< $Q^2 < 100 GeV^2$. The ratio $\frac{\sigma_L}{\sigma_T}$ for ρ^0 and ϕ production from H1 and ZEUS experiment is well described by the GPDs model taking the transverse momenta of parton into account [48]. Taking advantage of the collider H1 and ZEUS exploited the low x_B about 10^{-3} regime where the gluons dominate.

1.3.11.2 HERMES

HERMES used the beam from HERA facility and ran between 1995 to 2007. They have measured wide sets of DVCS observables like beam charge asymmetries [49], single beam spin asymmetries [50], and double beam asymmetries with both longitudinally and transversely polarized targets [51] [52]. The large measured number of DVCS observables were crucial to unfold the different CFFs contribution.

The HERMES collaboration also measured the cross-section for electroproduction of π^+. Their result was not described by the regular GPDs model [53], which predicts the dominance of σ_L. HERMES explored the intermediate x_B of about 10^{-1} where the sea quarks play a dominant role.

1.3.11.3 CLAS

CLAS is the CEBAF Large Acceptance Spectrometer installed in Hall B at Jefferson Lab. It covers a larger solid angle (about 4π) compared to the Hall A setup (about 6 msr). But Hall B only operates at smaller luminosity (about the order of 10^3) smaller as compared to Hall A for the same target configurations. CLAS collaboration measured various DVCS observables in the valence regime, for instance, the beam spin asymmetries [54] using the longitudinally polarized electron beam with a liquid hydrogen target and double spin asymmetries with a longitudinally polarized NH_3 target. They also reported the unpolarized and polarized DVCS cross-section at beam energy of 5.75 GeV [55]. With many assumptions, these measurements helped to put constraints on GPD H^f.

The CLAS collaboration is also active in search of transversity GPDs. Figure 1.15 [38] shows the extracted cross-section parameters for η and π^0 electroproduction measured by the CLAS collaboration at two different values of x_B and Q^2 [x_B=0.17 , Q^2=1.38 GeV^2] and [x_B=0.28 , Q^2=2.21 GeV^2]. The extracted cross-section parameters are compared with the transversity GPDs model by Goloskokov and Kroll (GK). The GK model describes the $\sigma_\mathrm{T} + \epsilon\sigma_\mathrm{L}$ term fairly well for both π^0 and η production.

1.3.11.4 COMPASS

The COMPASS collaboration (Common Muon and Proton Apparatus for Structure and Spectroscopy) also has a GPDs program. They use the primary proton beam from

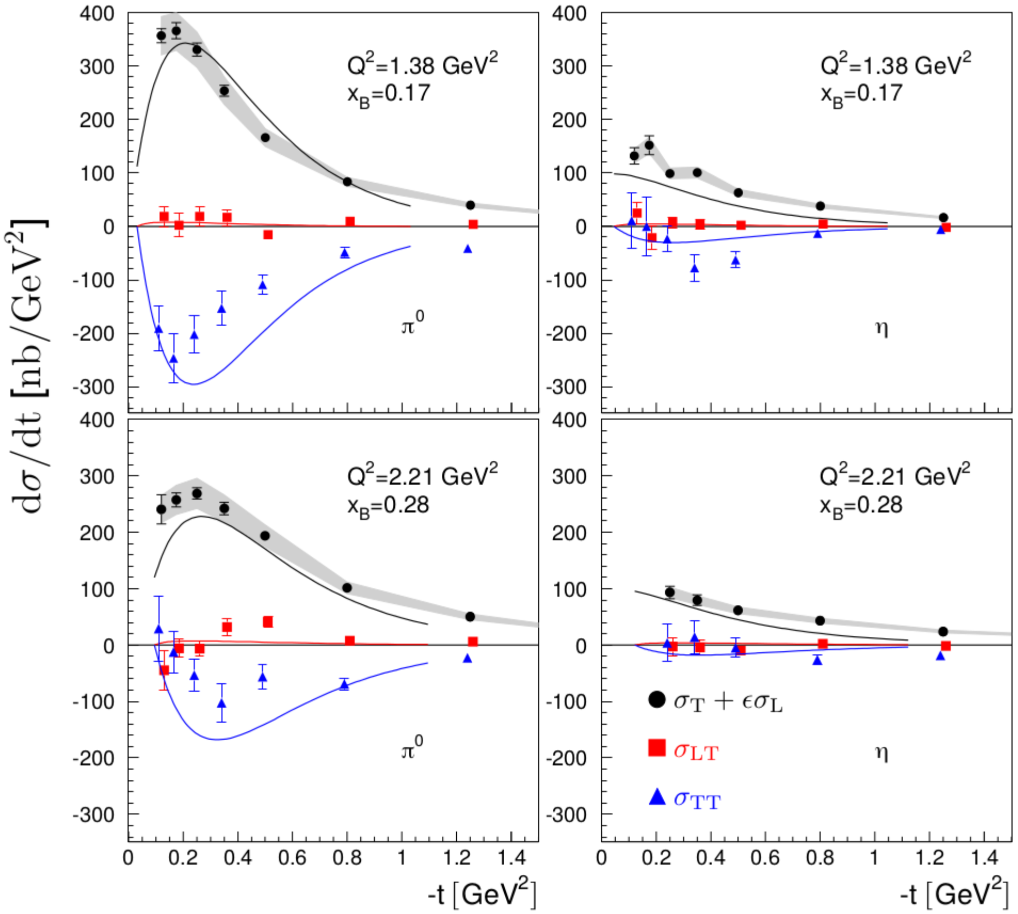

Figure 1.15: The extracted cross-section parameters for exclusive π^0 (left) and η (right) production at two different kinematic points. Black points are $\sigma_{\mathrm{T}} + \epsilon\sigma_{\mathrm{L}}$, red σ_{TL}, and blue σ_{TT}. Solid lines are the prediction by the GK model. The GK model underestimates the $\sigma_{\mathrm{T}} + \epsilon\sigma_{\mathrm{L}}$ especially in η production. Error bars are statistical only, and the grey band is systematic uncertainties for $\sigma_{\mathrm{T}} + \epsilon\sigma_{\mathrm{L}}$. This figure is taken from Ref. [38]. See the re-use permission in Appendix C.

the Super Proton Synchrotron (SPS) accelerator to produce a muon beam of both μ^- and μ^+. Their main program is to measure the charge and helicity-dependent cross-section to

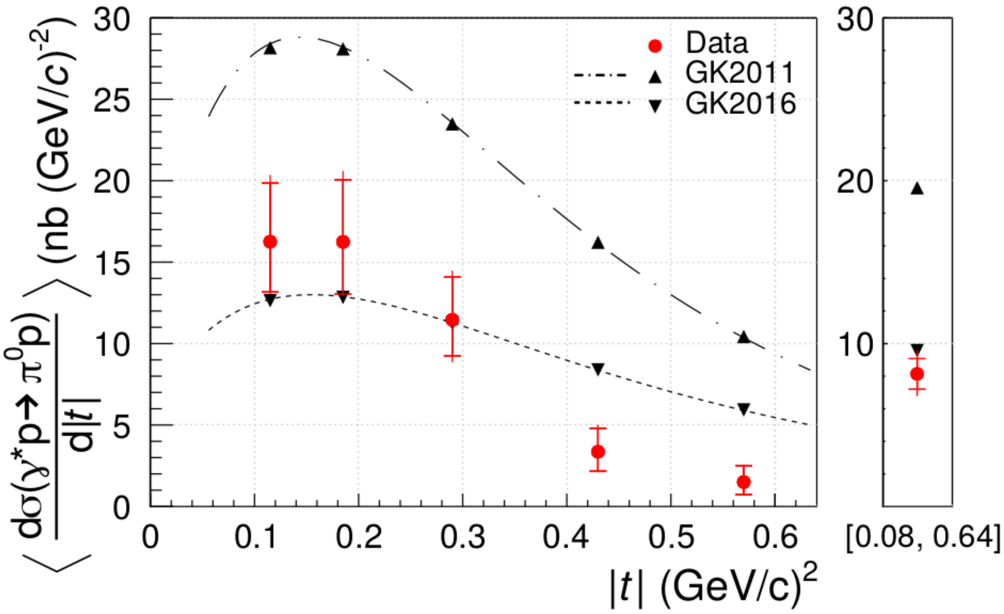

Figure 1.16: Exclusive muon π^0 production cross-section measured by COMPASS collaboration. GK model calculations inspired by the COMPASS results agree with data better than the original calculations made by GK [40]. This figure is taken from Ref. [56]. See the re-use permission in Appendix C.

separate the DVCS and interference terms. The kinematic range that COMPASS can cover is shown in Figure 1.14. They recently took DVCS data, and analysis is underway.

The COMPASS collaboration has also measured the exclusive π^0 production at Q^2=2 GeV^2 and x_B=0.0093 [56]. Figure 1.16 shows COMPASS collaboration cross-section data compared with the Goloskokov and Kroll model. In the kinematic regime covered by this experiment, the Goloskokov and Kroll model [40] overshoots the data. Later calculations by Goloskokov and Kroll (GK) [56] inspired by COMPASS results fairly agree with data. The ρ meson production data on a transversely polarized target from the COMPASS collaboration [57] shows a dominant contribution from the chiral odd GPD relative to chiral even GPD. Their result is consistent with the transversity GPDs model (GK).

1.3.11.5 Hall C

Hall C at JLab has measured exclusive π^+ production cross-section at Q^2 up to 2.5 GeV^2[58]. Their results show a sizeable contribution from σ_T. In the future, Hall C will utilize the new super high momentum spectrometer and a new electromagnetic calorimeter to measure DVCS and π^0 production cross-sections at different kinematic ranges exploiting the upgraded CEBAF facility at Jefferson Lab [59].

1.3.11.6 Hall A

Hall A at Jefferson Lab has conducted three different generations of dedicated DVCS experiments on both proton and neutron targets. The DVCS results from the first generation of DVCS on the proton showed the dominance of the handbag diagram in the DVCS process at moderate Q^2 (about 2 GeV^2) [60]. The second generation of DVCS results pointed out that there is a significant contribution from the higher twist term [22]. The same collaboration has published the DVCS results for the neutron target [61].

Hall A also measured exclusive π^0 production data on both proton and neutron targets. These experiments were before the energy upgrade. The results for the proton target is shown in Figure 1.13. The π^0 result for both the proton and neutron from an earlier generation of the experiment is in good agreement with the transversity GPD models [40]. The third generation of the experiment ran after the accelerator was upgraded to deliver a maximum beam energy up to 12 GeV. The analysis is ongoing both for DVCS and π^0 production. This document will present the results on π^0 production for x_B=0.60.

1.3.11.7 Electron-Ion collider

Measurement of GPDs with a hard exclusive process to access the 3D image of the nucleon is one of the important science programs for the future facility Electron-Ion Collider (EIC). The kinematic range that the EIC potentially can cover is shown in

Figure 1.14. This facility will be crucial in exploring the gluon and sea quarks GPDs and flavor separation of GPDs [62].

Integrating the information from past and future experiments, the GPDs in a wide kinematic range from gluons, sea quarks, and to valence quarks can be extracted. These measurements help to build the nucleon's tomographic image. The DVCS is a promising channel to extract the chiral even GPDs. For meson production, if the experiment finds the dominance of transversely polarized virtual photons, then it would open the unique opportunity to access the chiral odd GPDs through meson production. On the theory front, the contribution from transverse photons is included in the handbag approach (Goldstein Hernandez and Luiti [39] and Goloskokov and Kroll [40] models). The work presented in this document will be helpful to constrain the transversity GPDs models at higher x_B and Q^2 where data are not available.

2 THE E12-06-114 EXPERIMENT

In this chapter, I will discuss the experiment of interest “E12-06-114”. Experiment E12-06-114 took data at the Thomas Jefferson National Accelerator Facility (TJNAF), Newport News, VA. TJNAF is also commonly known as JLab. It was founded in 1985 with the primary goal of understanding the structure of nuclei and nucleons. Jefferson Lab is comprised of 4 different experimental halls: A, B, C, and D, each with different detector systems. All of these experimental halls receive the electron beam from the Continuous Electron Beam Accelerator Facility (CEBAF), which can deliver electron beams up to 12 GeV in energy[6]. E12-06-114 is the third generation of DVCS experiments. It ran in Hall A between 2014-2016. “DVCS3” will often be used to refer to this experiment in this document. DVCS3 is one of the first experiments to take data after the 12 GeV upgrade of CEBAF. The first two generations ran in 2004 and 2010 with maximum beam energy up to 6 GeV. The kinematic coverage of the DVCS3 experiment is shown in Figure 2.1.

2.1 Physics Goals

Experiment E12-06-114 had two major physics goals [63]. The primary goal was to measure both helicity-dependent and helicity-independent cross sections of DVCS process ($ep \to e'p'\gamma$) at fixed x_B over a wide range of Q^2 with high precision (about 5% relative precision). The extracted DVCS cross-section over a wide range of Q^2 provides a scaling test of cross-section, and will help to validate the GPD formalism if it is appropriate to describe the nucleon structure in this kinematic regime. Measuring both the polarized and unpolarized cross-sections allows a separation of the real and imaginary part of the DVCS-BH interference terms. The unpolarized and polarized cross-sections are connected with

---

[6] Only one experimental Hall D, can reach up to 12 GeV. The other halls can get a maximum beam energy of 11 GeV.

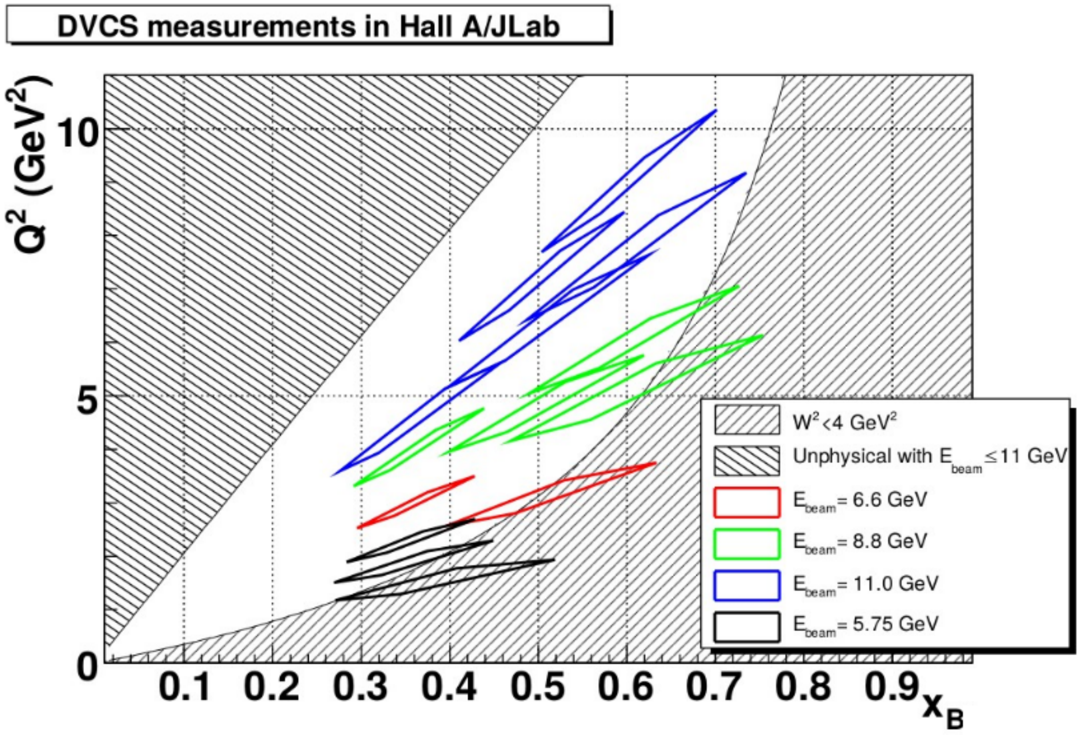

Figure 2.1: The phase space in x_B and Q^2 covered by three generations of the DVCS experiments at Hall A JLab. The black diamonds represent the phase space covered by the first two generations of the DVCS experiments at Hall A. The red, Green, and Blue diamonds represent the phase space that experiment E12-06-114 proposed to cover using three different beam energies. However, experiment E12-06-114 missed two kinematic points, one green and one blue at Bjorken-x 0.60 due to scheduling issues. The boundary of the unphysical region ($W^2 < 4$) corresponds to the maximum value of Q^2 at fixed x_B and beam energy of 11 GeV. The figure is adapted from Ref. [63].

the real and imaginary part of the DVCS amplitude as:

$$\sigma_{pol} = \overrightarrow{d}\sigma - \overleftarrow{d}\sigma = 2 \cdot \mathcal{T}_{BH} \cdot \mathcal{I}m(\mathcal{T}_{DVCS}) \tag{2.1}$$

$$\sigma_{unp} = \overrightarrow{d}\sigma + \overleftarrow{d}\sigma = | \mathcal{T}_{BH} |^2 + 2 \cdot \mathcal{T}_{BH} \cdot \mathcal{R}e(\mathcal{T}_{DVCS}) \tag{2.2}$$

where $\overrightarrow{d}\sigma$ and $\overleftarrow{d}\sigma$ are differential cross-sections with opposite beam polarization.

The experimental setup used to measure the DVCS cross-section also allows us to measure the cross-section of deep exclusive electroproduction of π^0 ($ep \to e'p'\pi^0$). The π^0 events are complimentary in this experimental setup. The lifetime of a π^0 is very small (about 10^{-17}s); therefore, it decays immediately into two photons ($\pi^0 \to \gamma\gamma$) with a branching ratio of about 99%. From the energy and momentum information of the decay photons, the π^0 can be reconstructed.

The primary physics motivation behind the π^0 production cross-section extraction is to test the QCD factorization prediction for meson production. In the factorization regime, σ_{L} scales as Q^{-6} and σ_{T} as Q^{-8}. In order to separate σ_{L} and σ_{T} from the total meson production cross-section, the cross-sections need to be measured at two different beam energies with the same Q^2 and x_B. Unfortunately, this experiment can not separate σ_{L} and σ_{T} cross-sections for π^0 production. Due to the lack of a cross-section measurement at multiple beam energies for a fixed x_B and Q^2, our result will be reported as a sum of σ_{L} and σ_{T} that is an unseparated cross-section (σ_U).

$$\sigma_U = \sigma_{\mathrm{T}} + \epsilon\sigma_{\mathrm{L}} \tag{2.3}$$

Along with σ_U, the interference terms σ_{TL}, σ_{TT}, and $\sigma_{\mathrm{TL'}}$ (only for polarized cross-section) are also extracted. The extracted cross-section terms can give a hint if σ_{L} is dominant over σ_{T} in our kinematic regime. The hard exclusive π^0 production cross-section terms will be compared against existing transversity GPDs model predictions. Our result at high x_B and Q^2 can potentially improve the existing transversity GPDs models. If data show the dominance of transversely polarized virtual photons in exclusive meson production cross-sections then transversity GPD models are very crucial to extract GPDs .

As DVCS3 was one of the first experiments after the 12 GeV upgrade of CEBAF, we encountered several technical difficulties related to accelerator performance. As a consequence, data taking for DVCS3 extended from 2014 to 2016. Table 2.1 shows

Table 2.1: Actual kinematics covered by E12-06-114 experiment. Data taking started in the Fall 2014 and was completed at the end of 2016. No useful data were taken in 2015. The data cover wide range in Q^2 ($2 < Q^2 < 9\ GeV^2$) for different values of x_B.

Period	Kinematics	Beam Energy (GeV)	Q^2 (GeV^2)	x_B
Fall 2014	36-1	6.66	3.2	0.36
Fall 2016	36-2	8.52	3.6	0.36
Fall 2016	36-3	10.62	4.47	0.36
Spring 2016	48-1	4.48	2.7	0.48
Spring 2016	48-2	8.84	4.37	0.48
Spring 2016	48-3	8.84	5.33	0.48
Spring 2016	48-4	11.02	6.90	0.48
Fall 2016	60-1	8.52	5.54	0.60
Fall 2016	60-3	10.62	8.4	0.60

different kinematic variables (beam energy, Q^2, and x_B) for all of the kinematics covered by DVCS3. For each of three different x_B (0.36, 0.48, and 0.60), cross-sections were measured at many Q^2 values. Out of these 9 different kinematics, this document will mainly focus on kinematic with x_B=0.60 for π^0 production cross-section analysis.

2.2 Continuous Electron Beam Accelerator Facility (CEBAF)

DVCS3 used the longitudinally polarized beam from CEBAF at JLab. The source of electrons is a Gallium Arsenide crystal doped with Phosphorus (GaAsP), which is placed at an ultra vacuum chamber. A Ti-Sapphire laser operated at 850 nm is used for optical pumping of electrons from the valence band to the conduction band. To deliver the polarized beam, a circularly polarized laser is used for optical pumping. The circularly

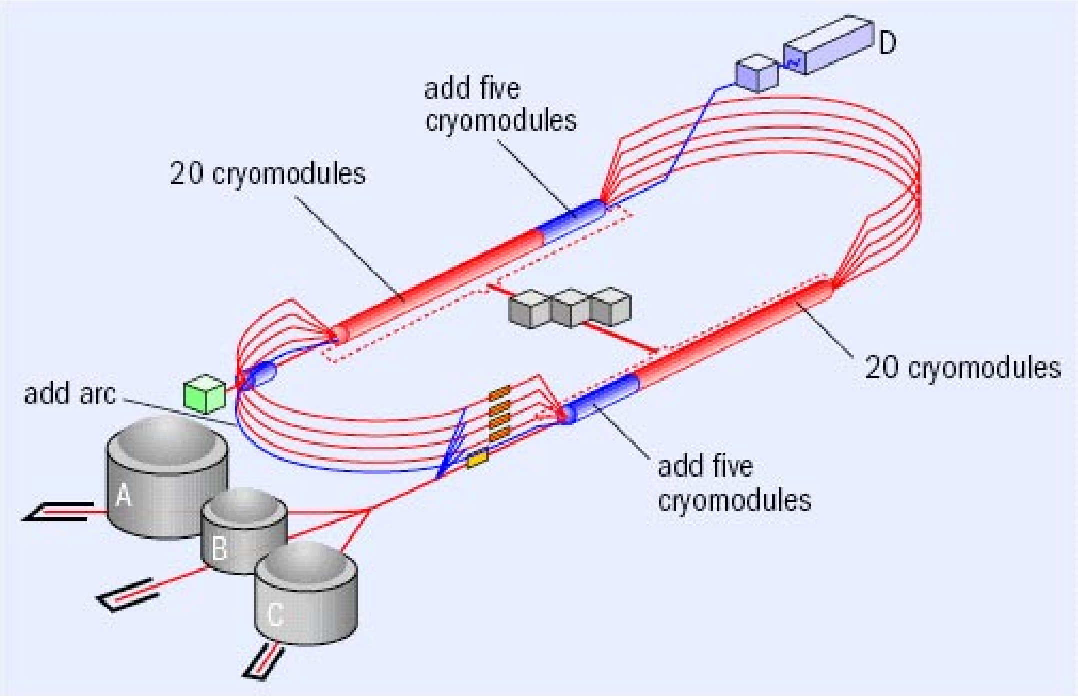

Figure 2.2: Schematic layout of upgraded CEBAF at Jefferson Lab. Upgraded CEBAF can deliver maximum beam energy up to 12 GeV. 10 cryomodules has been added, 5 in each linacs and additional arc has been built to recirculate the beam into the linac. This figure was taken from Jefferson website (https://www.jlab.org).

polarized laser beam is achieved by passing through voltage controlled wave plates called the Pockels cell. The beam helicity is flipped at the rate of 30 Hz by flipping the sign of voltage applied to Pockels cell [64]. The electrons in the conduction band are extracted by applying a potential difference, then accelerated to 45 MeV using the electric field before being injected into the North linac.

CEBAF is comprised of two linacs: North and South. Each consists of 25 superconducting cryomodules. Each of these cryomodules consist of 8 radio frequency cavities made of Niobium. The electrons from the source are injected into the North linac where they get accelerated and steered to the South linac through the magnetic arcs, as shown in Figure 2.2. Once the beam travels through the South linac, it is re-injected into the North linac through another magnetic arc, completing one pass. The beam is accelerated up to 2.2 GeV as it completes one pass (North + South linac). The beam can be recirculated in the linacs maximally up to 5 complete passes, thereby reaching the maximum beam energy of 11 GeV. But due to the position of the new experimental Hall D, the beam can be passed through one extra linac and reaches to 12 GeV before getting to Hall D. At the end of South linac, the accelerated beam is extracted using Radio Frequency (RF) separators. It can then be delivered to one of the three experimental halls (A, B, and C). The beam current sent to each hall can be controlled independently. CEBAF used to deliver the maximum beam energy up to 6 GeV. Thanks to the upgrade to 12 GeV, this enables us to explore new kinematics that was not possible for the first two generations of DVCS experiments.

CEBAF has many distinct features but some of the crucial features that make it proper to take data for experiment E12-06-114 are:

- CEBAF has a high duty factor

  Accelerator facilities deliver pulsed beam separated by some time interval. In a non-cryogenic accelerator the time gap between the two pulses is required to cool the machine because of the heating caused by the electric field necessary to accelerate the particles. The duty factor is a measure of how continuous the beam is. The higher duty factor means more continuous beam while a low duty factor beam will be more pulsed. CEBAF can deliver an almost continuous beam, thanks to its superconducting radio frequency cavity technology. Continuous beams help coincidence experiments like DVCS3[7] to reduce the accidental background rate. The signal to noise ratio for the coincidence experiment is related to the average beam

---

[7] for DVCS3 photon(s) are detected in coincidence with e^-

current (I_{avg}) and duty factor (df) as:

$$\frac{N_{signal}}{N_{noise}} \propto \left(\frac{df}{I_{avg}}\right) \tag{2.4}$$

Experimentalists desire to have a high value of the signal to noise ratio at a given beam current. For the given beam current, facility with higher duty factor can provide a higher signal to noise ratio.

- High beam luminosity

  The upgraded CEBAF can deliver a maximum beam current up to 180 μA [65]. However, the DVCS3 ran at relatively small current (about 15 μA) as the DVCS calorimeter was placed close to the beam line. This amount of current on the 15 cm long liquid hydrogen target correspond to the total luminosity of about 10^{38} cm^{-2} s^{-1}. High luminosity is another important factor needed to measure the small DVCS cross-sections.

- High beam polarization

  CEBAF can deliver the e^- beam with polarization as high as 86%. The measured beam polarizations for kinematics 60-1 and 60-3 were 86.20 ±0.10 (Stat.) ± 1.0 (Sys.) and 85.39 ±0.11 (Stat.) ± 1.0 (Sys.), respectively [66].

2.3 Experimental Hall A

Experiment E12-06-114 ran in experimental Hall A. In this section, the beamline component and Hall A standard equipments used by DVCS3 experiment will be described. Further details of Hall A instruments can be found in a NIM paper by the Hall A collaboration [67]. Figure 2.3 shows the schematic the layout of experimental Hall A. The beamline components used by the experiment E12-06-114 will be discussed in this section.

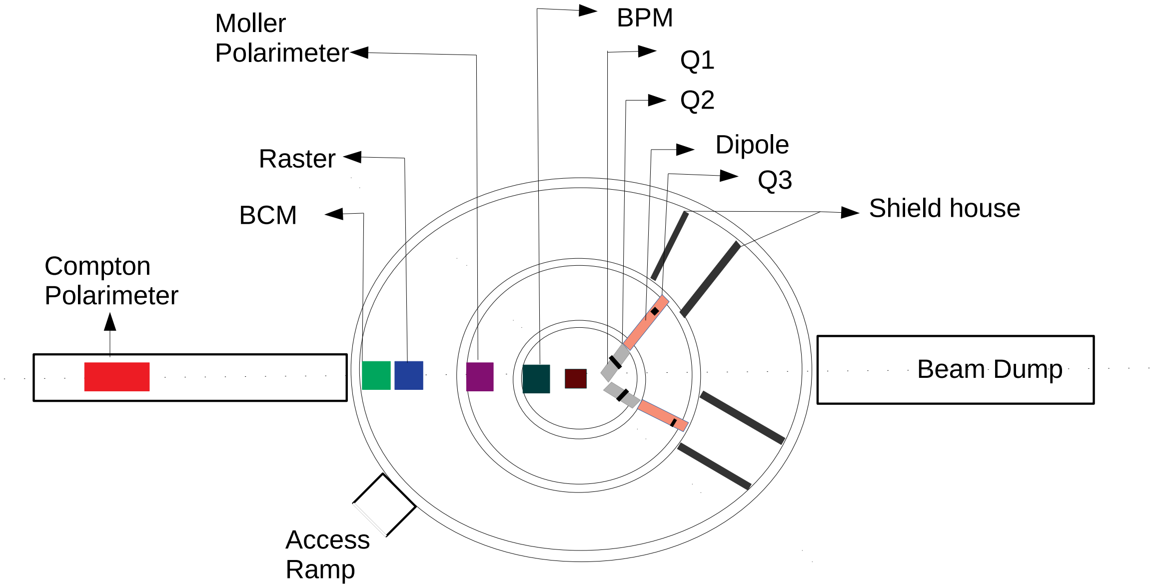

Figure 2.3: Schematic layout of experimental Hall A at Jefferson Lab. It consists of two identical High-Resolution Spectrometers (HRS): Left (LHRS) and Right (RHRS). Each spectrometer consists of three quadrupoles (Q1, Q2, and Q3) for focusing the e^- beam and a dipole (D) arranged in the Q1Q2DQ3 configuration.

2.3.1 Polarimeters

The beam polarization is measured by the two polarimeters: the Compton Polarimeter (located at the entrance of Hall A) and the Møller Polarimeter (located a few meters before the target). The Møller is an invasive[8] way of measuring the polarization of electron beam in the hall while the Compton is a non-invasive one. However, during DVCS3 the Compton detectors were not fully functional so the Compton measurements are not considered in our data analysis.

---

[8] a measurement that can not be done along with data taking process

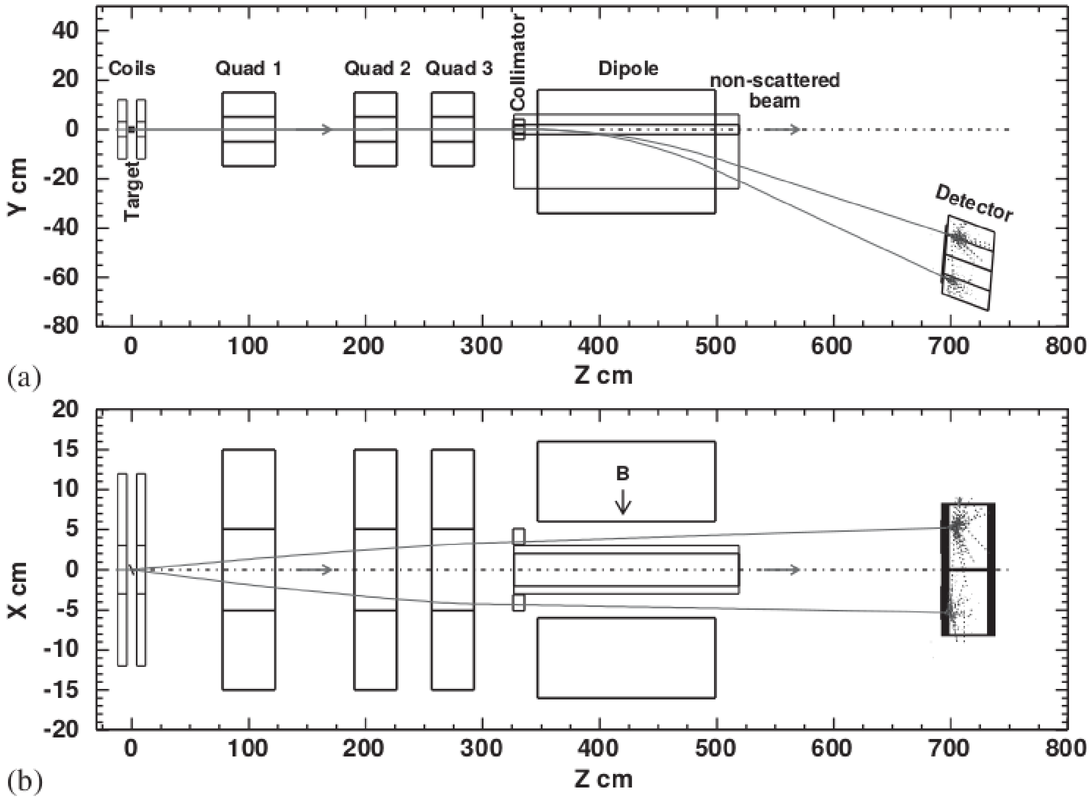

Figure 2.4: Schematic layout of the Møller polarimeter in Hall A. The top figure (a) represents the side view while the bottom figure (b) represents a top view. The paths followed by simulated Møller scattered electrons at $\theta_{CM} = 80^\circ$ and $\phi = 0^\circ$ are shown by the line. The figure is adapted from Ref. [67]. See the re-use permission in Appendix C.

The experiment E12-06-114 entirely relied on the Møller measurement for determining the beam polarization. The location of the Møller polarimeter is shown in Figure 2.3. This process is based on the scattering of an e^- beam off the atomic electrons (Møller scattering) of a ferromagnetic target polarized by a magnetic field of 24 mT. The scattered electrons are detected using the dedicated spectrometer. The e^- scattering cross-section depends on the beam polarization; hence the beam polarization can be infered by measuring the spin asymmetry. Figure 2.4 shows different components of the Møller polarimeter and simulated paths of the scattered electrons. For the Møller measurement, the target has to be inserted on the beamline, hence one cannot take data during the Møller measurement. Moreover, this process is carried out at low current (about 0.5 μA) which makes it an invasive process.

The main systematic for Møller measurement comes from the target polarization . For the experiment E12-06-114, the beam polarization was measured at least once in every kinematics. The typical beam polarization for this experiment is achieved around 85 ±0.11 (Stat.) ± 1.0 (Sys.) % [66].

2.3.2 Beam position monitors

A pair of Beam Position Monitors (BPMs) is located upstream to the target (see Figure 2.3) to measure the beam position and angle of their trajectory. Each BPM consists of a pair of antennas set up around the beam. As the beam passes through, it induces a current in the antennas. Comparing the intensities of the induced current in each antenna, the position of beam relative to antennas can be determined. The BPM can provide the relative position of the beam within 100 μm for currents above $1\mu A$ [68]. For absolute beam position, BPM is calibrated against the wire scanners called Harps, whose positions are surveyed regularly.

2.3.3 Beam current monitors

Beam Current Monitors (BCMs) are low noise and stable instruments used to measure the beam current. The BCM package consists of a Unser monitor, two RF cavities (upstream (U) and downstream (D) with respect to the beam direction), electronics, and data acquisition system. Figure 2.3 shows the positions of the upstream and downstream BCMs in Hall A. As the beam passes through the cavity, it induces the magnetic field within the cavity. The induced magnetic field is proportional to the beam current. The output signal from the BCM gives a relative measurement of beam current. For absolute current measurement, BCMs are calibrated against the Unser. The Unser monitor (or Parametric Current Transformer, P.C.T Toroids) [69] provides the absolute reference to beam current. The Unser can be calibrated against a known DC current source. Unfortunately the Unser cannot be used for a long time as its pedestal drifts in an unpredictable way over several minutes. Unlike the Unser, a BCM cannot be calibrated directly using DC current as it is an RF cavity, and the cavity does not induce a magnetic field with DC source. During experiment E12-06-114 each of the BCMs had two receivers: one analog and one digital. U1 and D1, the analog receivers, do not amplify the signal from cavities while D3 and D10 are other analog receivers that amplifies the signal from the downstream cavity by 3 and 10 times, respectively. Two new digital receivers, Unew and Dnew, were available since 2016 for development purposes. The output voltage of each receiver is sent to Voltage to Frequency (V-F) converters, and then to scalers. The rates (f_{BCM}) measured by the scalers are proportional to the current.

I was responsible for the BCM calibration during our run period. The BCM calibration is a two-step process:

- The Unser Calibration: The Unser is calibrated using known DC source current. The output of Unser is the frequency (f_{Unser}), which is linear in DC current used for calibration. The calibration coefficients relate the Unser output to the current passing through it as:

  $$I_{Unser} = f \times P1 + P0 \tag{2.5}$$

  Through the Unser calibration, the gain (P1) and offset (P0) were determined and later used to convert any f_{Unser} to the beam current in Unser (I_{Unser}).

  Figure 2.5 shows a typical fitting procedure to extract the Unser calibration coefficient. The calibration coefficients for Unser during the different run period can be found in Appendix D.

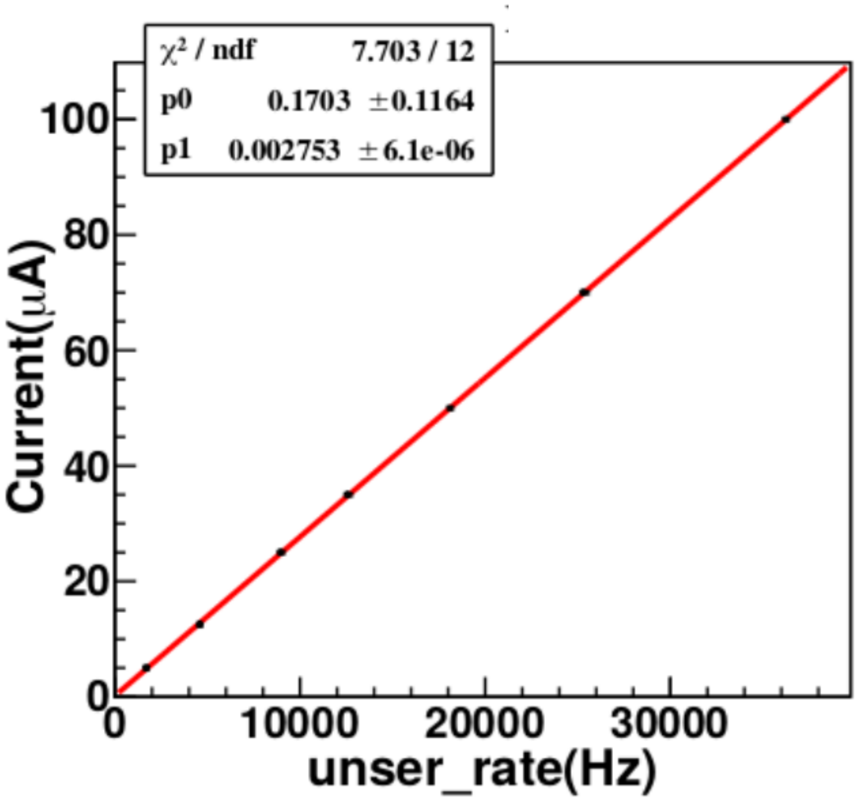

Figure 2.5: A Typical example of Unser calibration. The coefficients of a linear fit to the Unser response (frequency) against the known current source were extracted.

- The BCM calibration: Using the Unser as a reference current, the BCM is calibrated.

  The BCM output, f_{BCM} is fitted against the reference current (Unser current). A typical fitting procedure for BCM calibration is shown in Figure 2.6. The gain (G_{BCM}) and offset (I_0) were extracted by fitting the BCM output f_{BCM} as:

$$I_{Unser} = G_{BCM} \times f_{BCM} + I_0 \tag{2.6}$$

  The BCM calibration was typically done once every couple of weeks. After the series of calibrations for each run period, the gain of receiver D3 was found to be

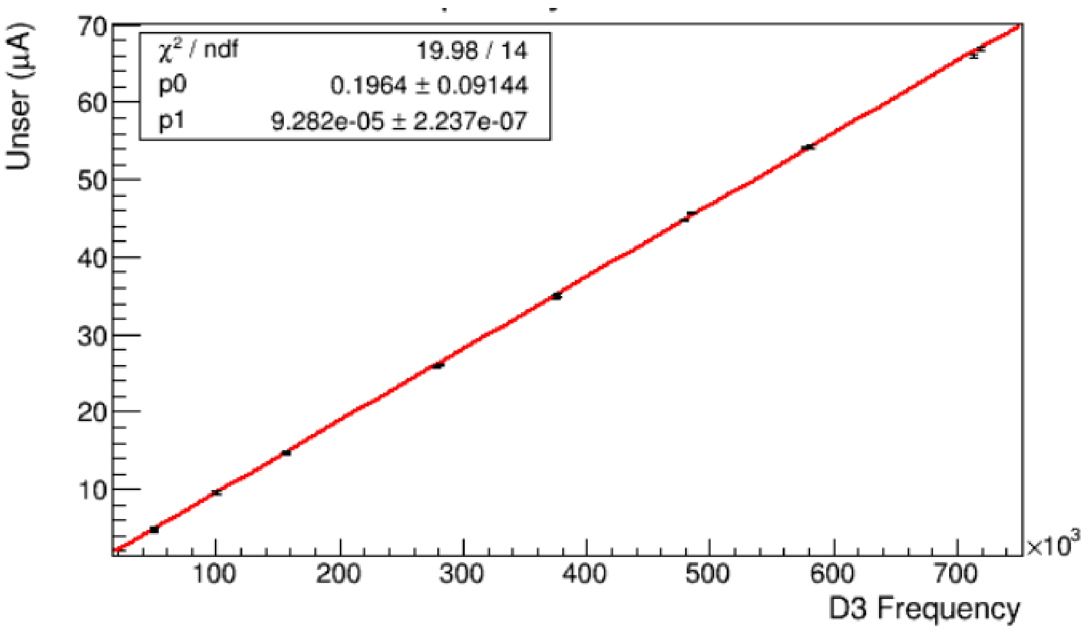

Figure 2.6: A typical fitting procedure to extract the calibration coefficients for BCM. The output of each BCM is fitted with a linear equation.

stable over a run period (see Figure 2.7 for the Spring 2016). Moreover, D3 was linear in the current range for the experiment E12-06-114 so we decided to use D3 for our current/charge measurement [70]. At the end, all those calibration runs were taken at once, and the BCM response was linearly fitted to extract the global gains and offsets. The gains and the offsets for different run periods are given in Appendix D.

BCM can measure current down to $1\mu A$ with a relative accuracy of 0.5% [67]. Equation 2.6 gives the instantaneous BCM current. Integrating Equation 2.6 over the total time (t) of the experiment yields the total charge accumulated:

$$Q = G_{BCM} \times C_{BCM} + I_0 \times t \tag{2.7}$$

where Q is charge accumulated in time t, and C_{BCM} is the total count from the scaler output.

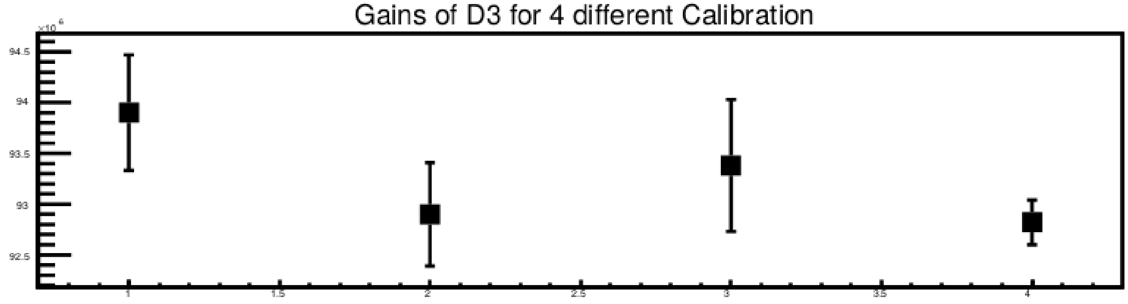

Figure 2.7: The extracted gains of BCM D3 for the Spring 2016. During the Spring 2016 BCM was calibrated 4 different times. The gain for D3 was stable for every run period, so we used D3 to measure the charge for the experiment E12-06-114.

2.3.4 Beam energy measurement

The beam energy is measured by an “Arc method.” The experimental Hall A is connected to the accelerator via a 40 m long arc section. The beam is steered through the arc section using eight dipoles. The momentum of electron beam (p) in GeV can be written as:

$$p = k \int \frac{\vec{B} \cdot \vec{dl}}{\theta} \tag{2.8}$$

where θ is deflection angle (radian), $\int \vec{B} \cdot \vec{dl}$ (Tm) is field integral and k =0.299792 GeV.rad.$T^{-1}\ m^{-1}$/c [67]. For beam energy measurement one needs to measure simultaneously the angle of deflection of beam and field integral in the arc. The magnetic field through the eight dipoles is not measured directly. Instead, a 9^{th} dipole identical to the other eight dipoles is connected in series for the measurement of the field. That 9^{th} dipole is use to extrapolate the total $\vec{B} \cdot \vec{dl}$ integral. The wire scanners located at the entrance and exit of the arc are used to measure the deflection angle. The precision in energy measurement is $\delta E/E = 10^{-4}$ [71].

2.3.5 Raster

Experiment E12-06-114 used a cryogenic target, and the beam in Hall A has high intensity with a small transverse section. So if the beam is directly passed through the target, it may locally heat the target and change its properties. To mitigate this situation a raster is used to move the beam on the target. The raster is a set of magnetic coils that can move the beam in both the horizontal and the vertical directions. The 2×2 mm rastered beam was used on the liquid Hydrogen target while running at around 20 μA. With the rastered beam, the density fluctuation from the beam heating is limited to a 1% percent at a beam current of 100 μA [72].

2.3.6 The target system

The cryogenic target system is mounted inside an evacuated target chamber. The DVCS3 took data on a Liquid Hydrogen (LH_2) target. The LH_2 was enclosed in a 15 cm long cylindrical aluminum target cell of about 15 mm thickness at entrance and exit window. The density of LH_2 target at the operating temperature of 19 K and pressure of 0.17 MPa is 0.0723 g/cm^2 [67]. Along with the cryogenic target, the target ladder consisted of another five solid targets. One of a solid target is the dummy target which is 15 cm aluminum cell without LH_2 inside it. It helps to estimate the scattering contribution from an Al window enclosing the LH_2. Another solid target is a multi-foil carbon target, which is used for optics calibration of the spectrometer. The other solid targets (carbon hole, BeO, and raster target) are used for beam centering purposes. All these targets are arranged in a vertical stack and can be moved remotely onto the beam path. Figure 2.8 shows the target ladder used for experiment E12-06-114. Further information about the Hall A target system used in this experiment can be found in Ref. [73].

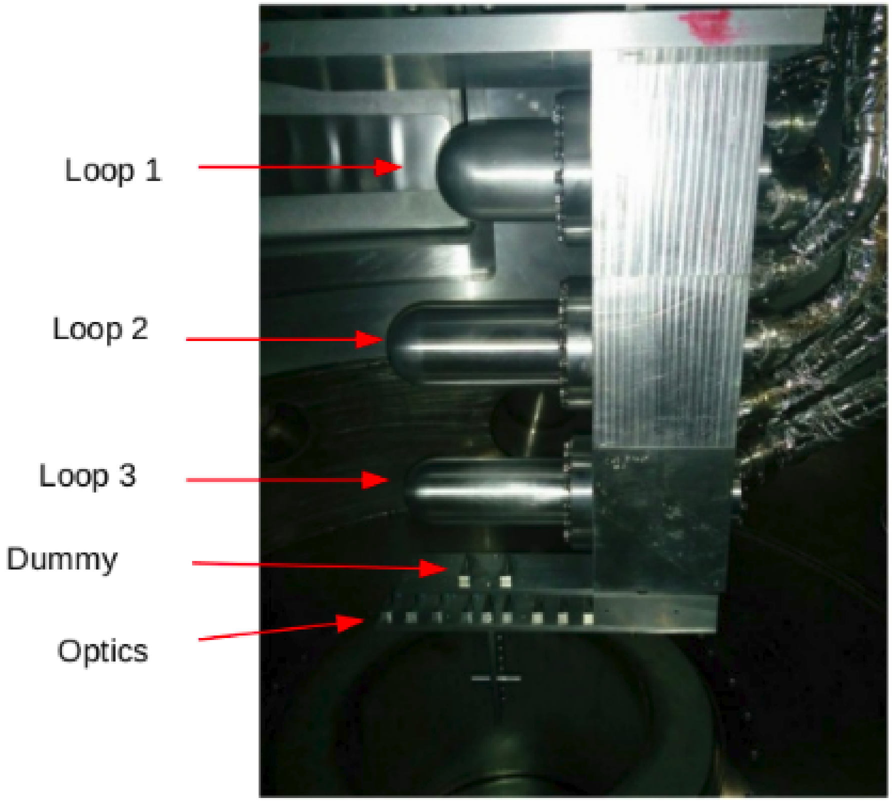

Figure 2.8: Hall A target scattering chamber during the experiment E12-06-114. Three cryotarget loops on top followed by solid targets dummy and optics (multi-foil target). During the Fall of 2016 loop 2 was used. During Spring 2016 and Fall 2014 loop 3 was used. The primary difference between the three cryotarget loops is the dimension of the entrance and the exit window of a cylinder containing the cryotarget. The other targets like carbon hole, BeO, and raster target are not shown in the figure. This figure is taken from Ref. [73].

2.3.7 The high resolution spectrometers

The Hall A contains of a pair of identical High Resolution Spectrometers (HRS), one in left (LHRS) and the other at right side (RHRS) of the beam direction. The momentum range of each of the spectrometers is 0.3 - 4.0 GeV/c with the acceptance of 4.5% with respect to the central momentum i.e -4.5% $< \delta P/P_0 <$ +4.5%. One of the main features of those spectrometers is high momentum resolution of the order of 10^{-4} between the momentum range of 0.8 to 4.0 GeV/c. The other features are a good position resolution, $\sigma_{x(y)}$ = 1mm and angular resolution, σ_θ = 0.5 mrad [67].

The HRS consists of three quadrupoles (Q) and a dipole (D) in the configuration QQDQ with a vertical bend. The first two quadrupoles focus the particles into a dipole on the way towards the detector hut. As the charged particles enter the dipole, they are deflected depending on their momentum. Based on this fact, one can tune the magnetic field of the dipole (both magnitude and polarity) to select the particles of desired charge and momentum. These particles are then focused by the third quadrupole to the detector stack.

The detector packages for each of the HRS are almost the same and shielded against background radiation by thick concrete blocks. Figure 2.9 shows the schematic representation of the spectrometer's detector package used by DVCS3. The tracking information is provided by a pair of Vertical Drift Chambers (VDCs). Each VDC consists of two wire planes oriented 90^0 to each other. The position and angular resolutions for the VDC are about 100 μm and 0.5 mrad, respectively. The detector package is equipped with scintillators, one long scintillator S0 and another plane of 32 scintillator labelled S2. The scintillators provide fast signals that are used for triggers. The gas Cherenkov filled with CO_2 at the atmospheric pressure is mounted between the two scintillators planes S0 and S2. It distinguishes between electrons and pions. The threshold for pions to create Cherenkov light is 4.8GeV/c while for electrons it is 17 MeV/c [67]. The coincidence between the Cherenkov and the scintillator, S2, forms the main electron trigger for this experiment. The electromagnetic calorimeter (Pion Rejector) is located at the end of the detector package. The pion rejector consists of two layers. Each of the layers consists of 34 identical lead glass blocks (left HRS). On the basis of the energy deposited on

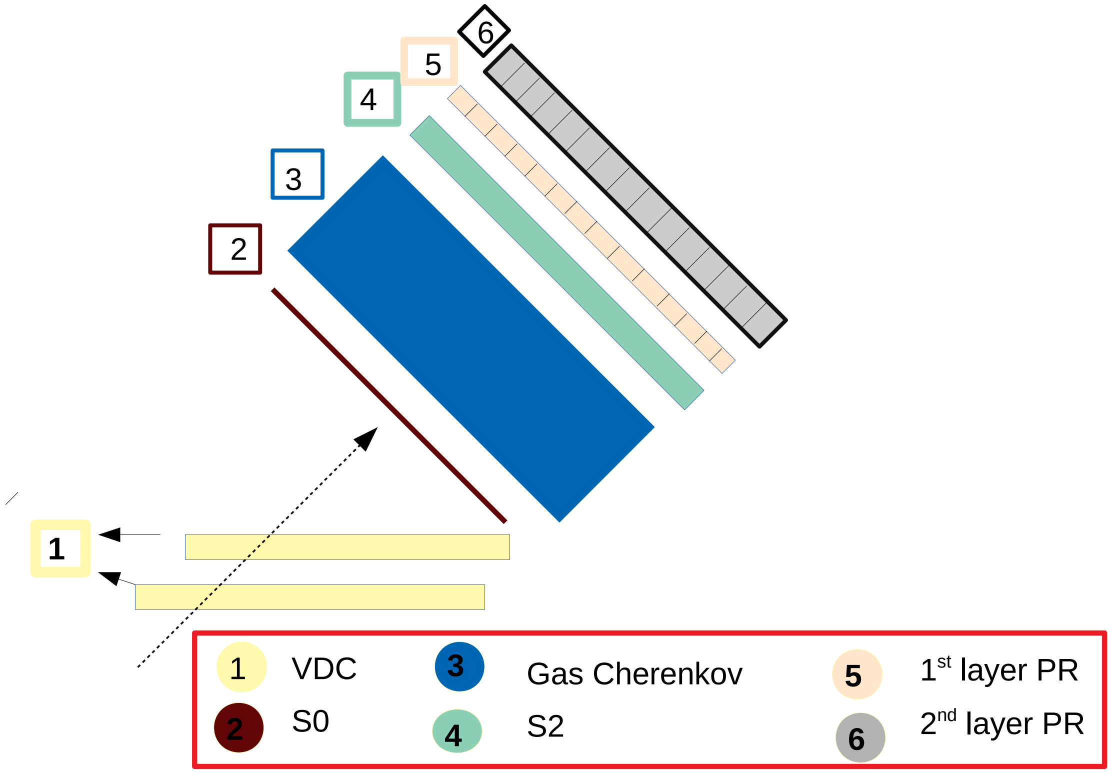

Figure 2.9: Schematic representation of HRS detector package used for DVCS3 experiment

the pion rejector, electrons and pions are discriminated. Pions being hadron deposit less energy in electromagnetic calorimeter. On the other hand, the electron deposits relatively high energy in the electromagnetic calorimeter as it interacts electromagnetically with the material of the calorimeter. The combination of the gas Cherenkov and electromagnetic shower detector select electrons with about 99% efficiency [74].

The standard Hall A detector package consists of other detectors that are not discussed in this document. This document is focused on the detectors used by the DVCS3. However, further information can be found at [67].

2.4 Experimental Setup for E12-06-114

As discussed in section 2.1, the primary purpose of this experiment is to measure the cross-section of exclusive channels: $ep \rightarrow e'p'\gamma$ and $ep \rightarrow e'p'\pi^0$. In the later channel, the lifetime of π^0 is very small (about $10^{-17}s$), so it decays into two photons immediately before reaching to detectors. The branching ratio of $\pi^0 \rightarrow \gamma\gamma$ is 98.823% [75]. During the cross-section analysis of π^0, the reconstructed π^0 events are corrected by the branching ratio. In both exclusive channels of interest, the scattered electrons are detected in Left High-Resolution Spectrometer (LHRS). The final photon(photons) is(are) detected in the DVCS dedicated electromagnetic calorimeter. In case of π^0 cross-section analysis, the π^0 events were reconstructed by the detection of two photons decayed from π^0. The recoiled proton is not directly measured. Instead, it is reconstructed using the energy and momentum information of the incident electron, the target proton, the scattered electron, and the final photon(s). The mass of the missing proton for DVCS and π^0 production is given by

$$M^2_{ep\rightarrow e'\gamma X} = (\mathbf{k} + \mathbf{p} - \mathbf{k'} - \mathbf{q})^2 \tag{2.9}$$

$$M^2_{ep\rightarrow e'\pi^0 X} = (\mathbf{k} + \mathbf{p} - \mathbf{k'} - \mathbf{q_1} - \mathbf{q_2})^2 \tag{2.10}$$

where **k**, **p**, and **k’** are the four-momentum vectors of the incident e^-, the target proton, and the scattered e^-. **q** is four-momentum of DVCS photon while $\mathbf{q_1}$ and $\mathbf{q_2}$ are the four-momentum of two decayed photons from π^0 in the case of pion production. The exclusive π^0 events can be further constrained by applying an invariant mass cut. The invariant mass of the π^0 can be reconstructed using the energy-momentum information of decayed photons,

$$m^2_{\pi^0} = m^2_{\gamma_1\gamma_2} = (\mathbf{q_1} + \mathbf{q_2})^2 \tag{2.11}$$

Figure 2.10 shows the experimental setup for experiment E12-06-114.

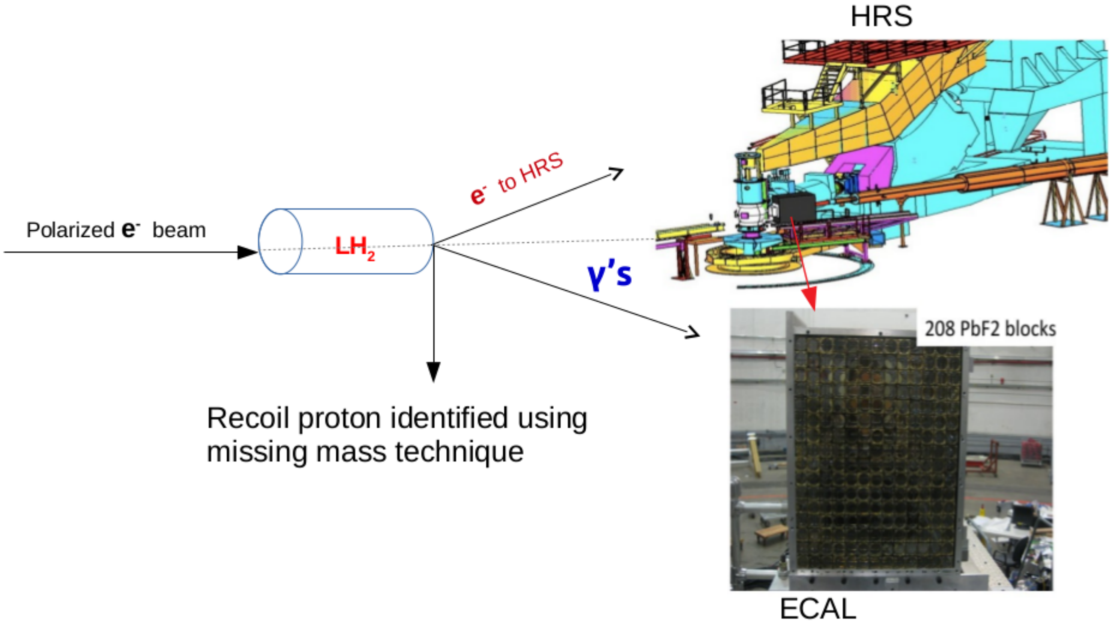

Figure 2.10: Experimental setup for the DVCS3 experiment. A longitudinally polarized e^- beam from CEBAF scatters off the Liquid Hydrogen (LH_2) target. The scattered e^- is detected by High-Resolution Spectrometer (HRS) while the photon (photons in case of π^0) is detected by the electromagnetic calorimeter (ECAL). The recoiled proton is identified indirectly using the missing mass squared technique.

2.5 Electromagnetic Calorimeter (ECAL)

Apart from the Hall A equipment, a dedicated DVCS electromagnetic calorimeter was used for a photon detection. The DVCS calorimeter consists of 208 lead-fluoride (PbF_2) blocks arranged in 16 rows and 13 columns. The dimension of each block is 3 cm × 3 cm × 18.6 cm. As the photon passes through the calorimeter, it produces showers of electron-positron pairs. Those electron-positron pairs pass through the calorimeter material and produce the Cherenkov light. This light is collected by photo-multiplier tubes (PMTs). A PMT is connected to the end of each block. The Molière radius and the radiation length of PbF_2 are 2.2 cm and 0.93 cm, respectively [63]. For the typical case of a photon hitting the center of a block, 90% of the incident energy is contained within that block. The total energy of that initial photon is absorbed within 9 adjacent blocks. Each block is wrapped in Tyvek and then in Tedlar paper to minimize the energy leakage between the blocks. However, there is small energy leakage, below 5% either from the back of block or from the space between the blocks. Due to the radiation damage, the resolution of calorimeter degrades with time, necessitating regular energy calibration. The energy resolution of a calorimeter during the data taking period of kinematics 60-1 and 60-3 was measured to be 2.39% at a beam energy of 4.2 GeV from elastic calibration [76]. The horizontal and vertical angular resolution measured during the same elastic calibration were 1.64 mrad and 1.36 mrad, respectively. During the elastic calibration the calorimeter was placed at 6m away from the target.

2.6 The Analog Ring Sampler

The DVCS calorimeter is small in size. In order to have an acceptance as large as possible, it is placed close to the target. Moreover to minimize data taking time DVCS3 ran at high luminosity (about $10^{37}\ s^{-1}\ cm^{-2}$). As a result, the raw events on the calorimeter is expected to be as high as 10 MHz [77]. This high event rate results in pile-up events where two or more events hit a given block in a narrow time window (see Figure 2.11). In this case, ADCs which typically integrate the signal within 60 ns window can not separate two signals. In order to deal with these pile-up events, the signal from each block is digitized by an Analog Ring Sampler (ARS). The ARS [78] consists of 128 capacitors that continuously samples the signal at a clock rate of 1 GHz in capacitor. If an external trigger is issued to the ARS, the sampling is stopped and the signal produced by the block in the last 128 ns preceding the stop is stored in capacitors and then digitized on demand.

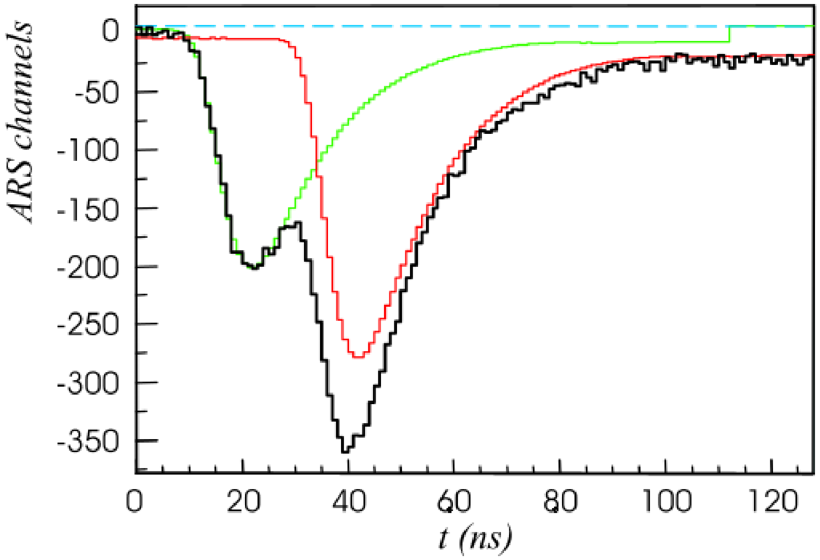

Figure 2.11: A typical example of a pile-up event recorded by ARS. ARS signals recorded in the 128 ns window. ARS takes the snapshot of the signal every 1 ns. The black signal is the sum of red and green signals arrived close in time (few ns). Offline analysis of the ARS signal allows to extract the green and red signals from the black one with good time and energy resolution. The figure is taken from Ref. [77].

2.7 Data Acquisition and Trigger

The Data Acquisition (DAQ) process uses the CEBAF Online Data Acquisition (CODA) developed by the JLab data acquisition group [67]. Each detector is connected to Analog-Digital Converters (ADCs), Time-to-Digital Converters (TDCs) or scalers. The signals are read out by VME crates. All the crates are controlled by Read-Out-Controller (ROC) which are connected to a Trigger Supervisor (TS). The TS controls the trigger: as a trigger fires, the TS orders the ROCs to gather the data, buffer them and stored in local disks. The data in the local disk are subsequently moved to the Mass Storage Tape Silo (MSS) for long term storage.

The DVCS trigger is a two-level decision logic. The first level trigger logic is formed by a scintillator (S2) signal and a Cherenkov signal in coincidence (S2&Cherenkov) in the HRS. A threshold is set on Cherenkov so that π^- events triggering S2 are rejected. Once electron is identified by the HRS, the second level decision will be to search for a photon(photons) in the calorimeter in coincidence with HRS e^-. As S2&Cherenkov trigger is fired, the TS sends a stop signal to the ARS system. The signals produced by the blocks are equally divided between the ARS and ADCs, one ARS, one ADC for each block. The calorimeter trigger module computes the sum of the integrated ADCs signal for all 2×2 neighboring blocks called towers. If an integrated ADCs tower is above a set threshold, then a VALID signal is sent to the trigger supervisor, and the whole event is recorded (LHRS and ARS data). The ARS is then reset. It takes 128 μs to digitize and transfer the ARS data [79]. Otherwise, if the ADCs integrated sum from the calorimeter trigger module does not pass the threshold, the ARS signals are cleared within 500 ns, and the DAQ gets ready for a new signal. The schematic representation of the trigger configuration is shown in Figure 2.12.

As S2&Chernkov trigger rate was low for both kinematics with x_B=0.60 about few hundred kHz, no threshold was set on ADC sum to select the photons. Along with electron and photon in coincidence, we also triggered on inclusive DIS event for DIS cross-section extraction. The DIS trigger was formed by the S2&Cherenkov signal and an external prescaled valid signal for the ARS. Because of the high DIS rate, a suitable prescale was set on the DIS trigger. The prescale factor allows to save only a fraction of the event that pass the trigger. The prescale factor helps to reduce the dead time caused by engaging electronics to save each event.

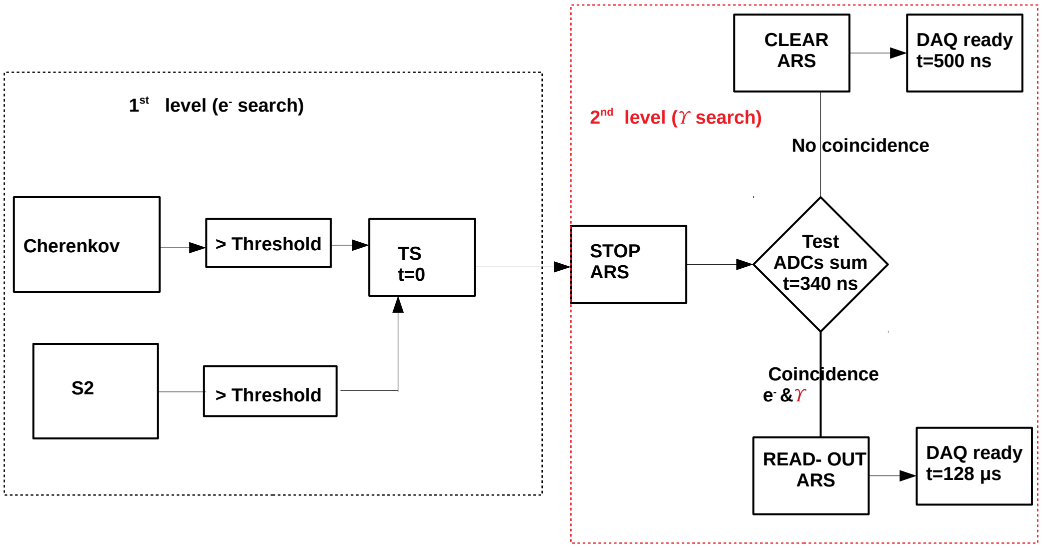

Figure 2.12: Schematic diagram of the two-level DVCS Trigger system. The first logic is to identify an $e-$, by looking at the events that trigger S2 and Cherenkov in coincidence. The second level decision is to identify if there is a photon(photons) in coincidence with e^{-}. To detect potential photon candidates, it computes the integrated ADC signal from the calorimeter in a 60 ns time window for every signal passing the first logic. The ARS signals are recorded or cleared depending on whether the integrated ADCs signal passes the set threshold or not.

In some of the kinematics, in addition to DVCS and inclusive DIS trigger, the other triggers formed by different combinations of S0, S2, and Cherenkov coincidences were present. For instance, S0&S2 and S0&Cherenkov. These additional triggers were for the measurement of detectors efficiencies. Expect for the DVCS, the main coincidence trigger, all other additional triggers had an external validation for the calorimeter trigger that bypassed the search for a high energy photon in the calorimeter.

3 DEEP INELASTIC SCATTERING

The E12-06-114 experiment ran with multiple coincidences triggers simultaneously formed by different detectors. In addition to triggering on e^- and γ in coincidence, we also had a trigger to record the inclusive electron events for every nine kinematics. For inclusive electron events, the trigger was formed by the scintillator (S2) and Cherenkov (CER) in coincidence as shown in Figure 2.12. Same detectors were used to trigger the DVCS/π^0 event, but in case of the Deep Inelastic Scattering (DIS) the electrons events were recorded regardless of the energy deposited by coincidence photon(s) in the calorimeter. This configuration allowed us to measure the DIS cross-section, the process described in section 1.2, in all nine kinematics. The DIS cross-sections are well known in our kinematic regime, so reproducing them with our data would help us to understand the luminosity, e^- detection efficiency, systematic errors, and overall normalization of our data. In this chapter, I will present my DIS cross-section analysis.

3.1 Cross-section Extraction Principal

The experimental differential DIS cross section is given by:

$$\frac{d^2\sigma}{dx_B\, dQ^2} = \boxed{\frac{N_{DIS}}{\mathcal{L}} \times \frac{1}{\eta_{Tracking} \times \eta_{S2} \times \eta_{CER} \times LT}} \times \boxed{\frac{1}{\eta_{virt}}} \times \boxed{\frac{1}{\alpha(x_B, Q^2) \times \Gamma_{DIS}(x_B, Q^2)}} \tag{3.1}$$

A short description of individual terms used in Equation 3.1 is given below. The detail can be found in the later sections of this chapter.

- N_{DIS} : The total number of DIS events passing through the selection cuts.
- $\eta_{Tracking}$: A factor correcting for the events misidentified by the tracking detectors, Vertical Drift Chambers (VDCs). The misidentified events are good electron events that are not properly tagged by the VDCs.

- η_{S2} : A factor correcting the events due to the inefficiency of the scintillator S2.
- η_{CER} : A factor correcting the events due to the inefficiency of the Cherenkov detector.
- LT : A factor correcting the events lost due to the dead time/ live time of the trigger.
- $\mathcal{L}$: The integrated luminosity gives the estimation of the number of the collision that can be produced in a unit area for a given time duration. It can be computed as :

  $$\mathcal{L} = \left(\frac{Q}{e}\right)\left(\frac{N_A \times \rho \times l}{A_H}\right) \tag{3.2}$$

  where e = 1.602×10^{-19} C is the charge of an electron , A_H = 1.0079 g/mol is the atomic mass of hydrogen, N_A = 60.22 $\times 10^{23}$ mol^{-1} is Avogadro,s constant, l=15 cm is length of the LH_2 target at operating temperature and pressure of 17 K and 25 psi, and ρ=0.07229 g/cm^3 is the density of LH_2 at the same operating temperature and pressure. The accumulated charge Q is measured using the BCM described in section 2.3.3 for every single run.
- η_{virt} : A factor correcting the virtual internal radiative effects.
- $\Gamma_{DIS}(x_B, Q^2)$: The phase-space from where the N_{DIS} events are selected.
- α (x_B,Q^2) : A factor to incorporate the kinematic dependence of cross-section. This factor allows us to extract the cross-section at a nominal value.

In Equation 3.1, terms in the red box are extracted using the data, the term in the green box is obtained from theoretical calculations, and the terms in the purple box are inputs from the simulation. Table 3.1 lists the values of these terms used for the DIS cross-section calculation.

Table 3.1: Summary of analysis cuts and correction factors used in the DIS analysis.

Kinematic	$\eta_{Tracking}$	η_{CER}	η_{S2}	η_{virt}	α	LT
36-1	0.943	0.998	0.997	1.077	0.863	0.99
36-2	0.940	0.997	0.997	1.078	0.865	0.98
36-3	0.935	0.998	0.996	1.079	0.863	0.97
48-1	0.959	0.997	0.996	1.076	0.947	0.98
48-2	0.941	0.997	0.996	1.079	1.209	0.95
48-3	0.946	0.997	0.996	1.080	1.037	0.98
48-4	0.943	0.997	0.996	1.082	1.123	0.98
60-1	0.938	0.998	0.997	1.080	0.885	0.98
60-3	0.940	0.997	0.996	1.083	0.889	0.97

3.2 HRS Optics with Saturated Q1

As described in chapter 2, the scattered electrons are transported through the magnetic spectrometers up to the detectors. The spectrometer consists of 3 quadrupoles and a dipole. In principle, all of these electro-magnets are tuned to select the particles of desired momentum range. Particles are bent in the magnetic field of the spectrometer. Characteristics of the trajectory of a particle exiting the spectrometer is measured by the VDCs (see section 2.3.7). A complete trajectory is defined by four variables (δ, y, ϕ, and θ). The θ is the tangent of the angle in the dispersive plane, while y and ϕ are the position and tangent of the angle perpendicular to the dispersive plane (see Figure 3.1). The δ is the fractional deviation of the momentum of a particle with respect to the central momentum of HRS i.e.

$$\delta = \frac{P - P_0}{P_0} \tag{3.3}$$

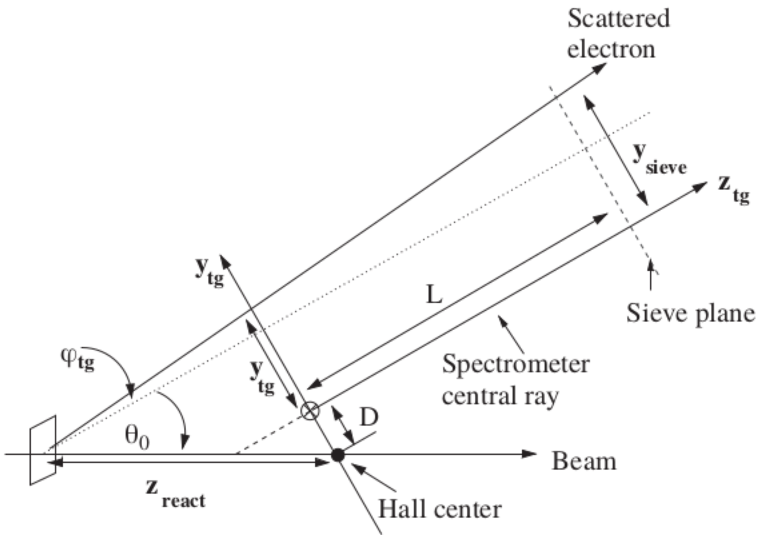

Figure 3.1: Definition of the variable defining the acceptance of HRS. The figure is adapted from [67]. See the re-use permission in Appendix C

.

where P is momentum of particle and P_0 is the central momentum of HRS.

The positions (x,y) and angles (θ, ϕ) of the trajectory in the spectrometer focal plane can be related to the characteristics of the trajectory at the target (at entrance of the spectrometer) by an optics matrix ($[\Phi_{tg}^{fp}]$), such that

$$\begin{pmatrix} \delta \\ y \\ \phi \\ \theta \end{pmatrix}_{tg} = [\Phi_{tg}^{fp}] \times \begin{pmatrix} x \\ y \\ \phi \\ \theta \end{pmatrix}_{fp} \tag{3.4}$$

The optics matrix can be extracted from dedicated data taking (see Hall A NIM paper [67] for further information).

In order to select the particles of the desired momentum range, a specific value of the magnetic field needs to be applied in the spectrometer. To have the desired field, a suitable current is passed through the coils of the magnets. As long as the applied current is linear to the magnetic field, the same optics matrix can be used to recompute the target variables using Equation 3.4, despite the momentum setting in the spectrometer. But when the linearity between the induced magnetic field and current applied does not hold, then optics data are needed to recompute the optics matrix for that particular momentum setting. Usually for standard optics calibration, optics data are taken at low momentum (1.0 GeV/c) because rates are high. For Fall 2014, the standard optics was used as Q1 was fully functional. For Spring 2016, the Q1 was not fully functional due to cryogenic coupling issues [80]. But we were aware of this fact and took the optics calibration data for the specific momentum settings we worked with. Optics calibration for Spring 2016 was done by F. Georges [81].

In Fall 2016, Q1 in the left HRS was replaced by the quadrupole Q1 of the obsolete Short-Orbit Spectrometer (SOS) of Hall C. During this run period, the applied current in the Q1 was not linear with the induced magnetic field in it beyond 550 A (see Figure 3.5). But in most of our kinematics, to have the desired momentum (magnetic field), the required current in the Q1 was above 550 A. Unfortunately, we were not aware of that Q1 saturation and did not collect the optics data for the optics calibration. Instead, used the simulation to compute the correction in the optics matrix due to the Q1 saturation. In this section, I will describe the optics matrix correction procedure briefly for the Fall 2016 run period.

Figure 3.2 shows the ratio of Q1 field as shown by the Hall A magnetic probe to the expected value for the given current reading. In principle, the relative field should stay constant at one at different currents (I). But the Q1 field was below the expected value above 550 A. The reduction in the field due to saturation effect can be parametrized by

$$\frac{\left(\frac{B}{P}\right)_{saturated}}{\left(\frac{B}{P}\right)_{expected}} = 1 - 0.27\left[\frac{I_{readback}}{550A} - 1\right]^2 \tag{3.5}$$

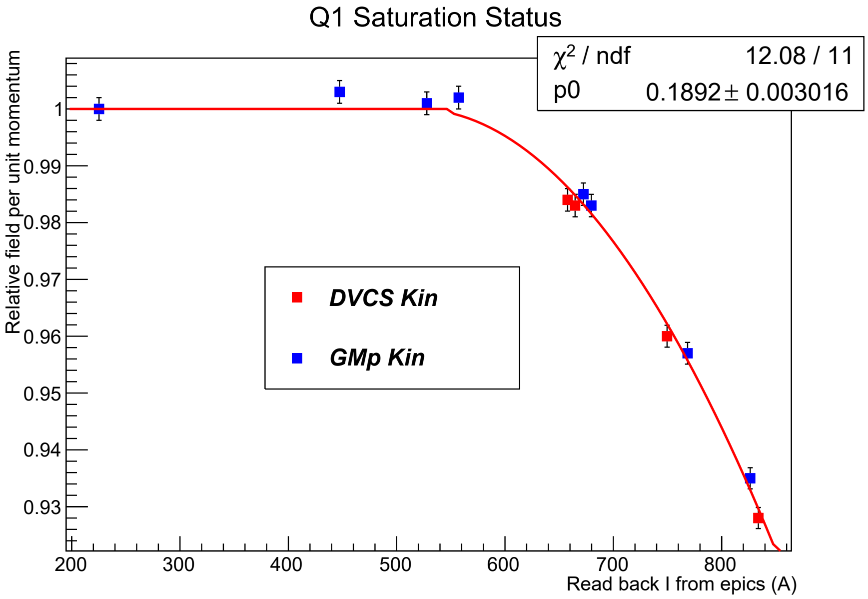

Figure 3.2: Reduction in quadrupole Q1 field as the function of read back current. The field measured in Q1 by a hall probe is compared to the expected field for a given applied current (Read back I from epics). We (DVCS) ran concurrently with other experiment (GMp) using same magnets, so the kinematics for both experiment is shown in figure. The Q1 was saturated beyond 550 A. The red line is a graphical representation of Equation 3.5.

Due to the lack of optics data to account for this saturation effect, we relied on Monte-Carlo simulation for the optics matrix optimization. The correction procedure was adapted from Ref. [72]. First, using the COSY simulation package [82] the optics matrix was generated with the actual Q1 field (Q1 saturated field). COSY generates the vertex of the multi-foil target to map out the magnetic field in the spectrometer. Then pseudo-data for optics calibration were generated using SIMC [83]. SIMC transports the particles from the entrance window of the spectrometer to the detector through the magnetic field, and applies realistic resolution effects. The simulated pseudo-data were used to determine the saturated optics matrix in the same way as regular data would be. Once the optics matrix for saturated setting was determined, the correction factor ($\Delta X'_{tar}$) due to the reduction in the field is given as:

$$X'^{sat}_{tar}(\delta_{fp}, \theta_{fp}, y_{fp}, \phi_{fp}) = X'^{Nominal}_{tar}(\delta_{fp}, \theta_{fp}, y_{fp}, \phi_{fp}) + \Delta X'_{tar}(\delta_{fp}, \theta_{fp}, y_{fp}, \phi_{fp}) \tag{3.6}$$

where X'^{sat}_{tar} is the optics element with pseudo-data from SIMC simulation with Q1 saturated field, $X'^{Nominal}_{tar}$ is reconstruction element determined using the optics data without Q1 saturated. For example,

$$X'^{Nominal}_{tar} = A_{0000} + A_{0010}y_{fp} + A_{0001}\phi^2_{fp} + A_{0011}y_{fp}\phi_{fp} \tag{3.7}$$

$$X'^{sat}_{tar} = B_{0000} + B_{0010}y_{fp} + B_{0001}\phi^2_{fp} + B_{0011}y_{fp}\phi_{fp} \tag{3.8}$$

$$\Delta X'_{tar}(\delta_{fp}, \theta_{fp}, y_{fp}, \phi_{fp}) = (B_{0000}-A_{0000})+(B_{0010}-A_{0010})y_{fp}+(B_{0011}-A_{0011})y_{fp}\phi_{fp}+.. \tag{3.9}$$

The coefficients A_{0000}'s and B_{0000}'s are optics matrix elements from data without Q1 saturation and with Q1 saturated determined with SIMC pseudo-data, respectively.

The corrected matrix is used to reconstruct the vertex position of the multi-foil target. Figure 3.3 is the reconstructed vertex of a multi-foil target whose foils position are known. The blue one with the poor resolution is before correcting the optics matrix, while the red one is after optics optimization. The impact of optics correction on vertex resolution is very distinct. After the optimization, the positions of the foils are well reconstructed.

3.3 Event Selection

The events selected by the DIS trigger (S2&CER in coincidence) are not all DIS events. The events are passed through a series of analysis cuts to select the sample of good DIS electrons. The analysis cuts used to select the DIS events will be described in this section.

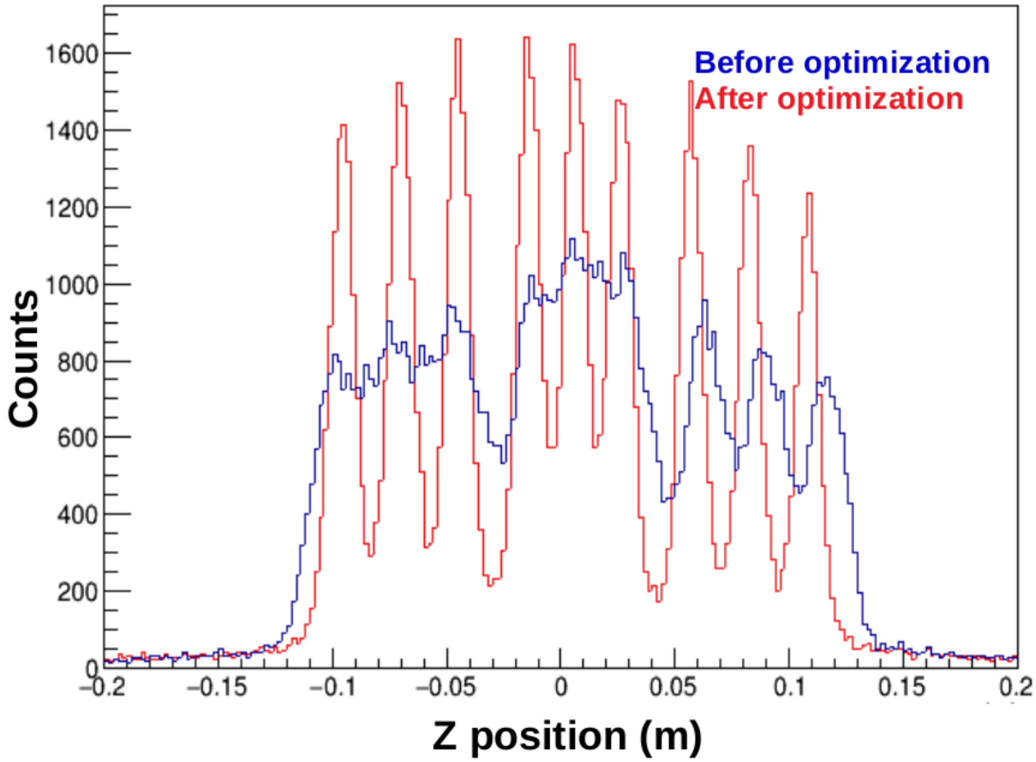

Figure 3.3: Reconstructed z vertex position for the data taken for optics (multi-foil) target with 7.2% Q1 saturation. The blue histogram is from data analyzed with regular optics matrix. The red histogram is of same the data analyzed with the corrected optics matrix. After the correction, the resolution looks better, and the position of foils are reconstructed at their expected positions.

3.3.1 HRS acceptance cut

Events produced at the target enter the spectrometer if they pass through the thick collimator that defines the geometrical acceptance of the HRS. Not all the events passing through the entrance window of the HRS are ultimately detected by the focal plane detector. Edge effects throughout the magnetic path of the particle limit the phase-space (δ, y, θ, ϕ) that the HRS can detect. There are two approaches to estimate that phase space: (1) a full simulation of the spectrometer magnetic area and focal plane detector or (2) an effective extraction based on the reconstructed trajectories. Our collaboration choose the effective method.

Our GEANT4 based Monte-Carlo simulation does not transport the particle in the magnetic field. Instead, it assumes all the particles passing through the HRS entrance window are detected in the detector. Due to this reason the effective HRS acceptance needs to be determined.

The naive way to define the HRS acceptance would be applying the 1-dimensional cut in each of the four variables, but due to the correlation between these variables, such cuts will be inefficient. Instead, the HRS acceptance is defined in a 4-dimensional hyperspace. The R-Function depends on 4 variables (δ, y, θ, and ϕ see Figure 3.1) and reduce that hyperspace to one number the R-value. The R-value represents the closest distance of any one point (δ, y, θ, ϕ) to defined boundary in the 4-dimensional hyperspace. As discussed in the earlier section, one of the quadrupoles was not fully functional and was detuned at a different extent in the different kinematic setting. As a consequence, we had to determine the R-Function for each kinematic settings. To determine the acceptance, boundaries are set on each of the 2D planes made by 4 different variables (see Figure 3.4). Once the limits are set on the 2D planes then for every electron, the minimum distance from those boundaries is computed. This minimum distance is called R-value. Now for the acceptance cut, the computed R-value distribution for data and Monte-Carlo events are compared, as shown in Figure 3.5. The threshold R-value, R-cut, above which the data and Monte-Carlo matches, is assigned as acceptance cut for the spectrometer for that kinematic. The analysis by A. Johnson [84] confirmed implementing R-Function analysis instead of 1D cuts in each target variable is better; as the extracted DIS cross-section is more stable and additionally allows us to consider more events.

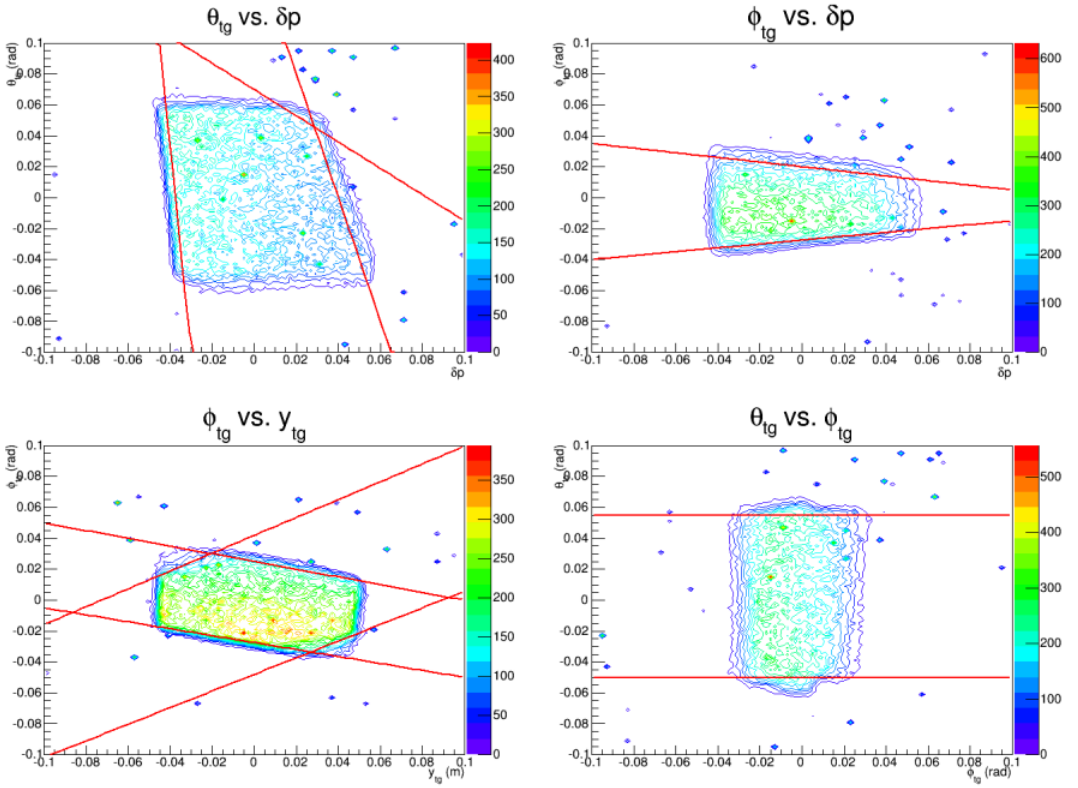

Figure 3.4: The distribution of target variables on 2D planes. Top left: distribution of θ_{tg} vs δ_{tg} Top right: distribution of ϕ_{tg} vs δ_{tg}. Bottom left: distribution of ϕ_{tg} vs y_{tg}. Bottom right: distribution of θ_{tg} vs ϕ_{tg}. The red line defines the edges of the spectrometer acceptance in these planes. Some boundaries are not shown in the figure as they would be redundant with the limit set on other planes. The figure is extracted from [85].

3.3.2 Vertex position cut

The liquid hydrogen (LH_2) target is contained in an Aluminum cylinder. The entrance and exit window of the Aluminum cyclinder is about 0.15 mm thick. Some of the electrons scatter off the Aluminum window, and these events should be eliminated from the analysis. For this process, we took data on the dummy target, an Aluminum cylinder slightly thicker

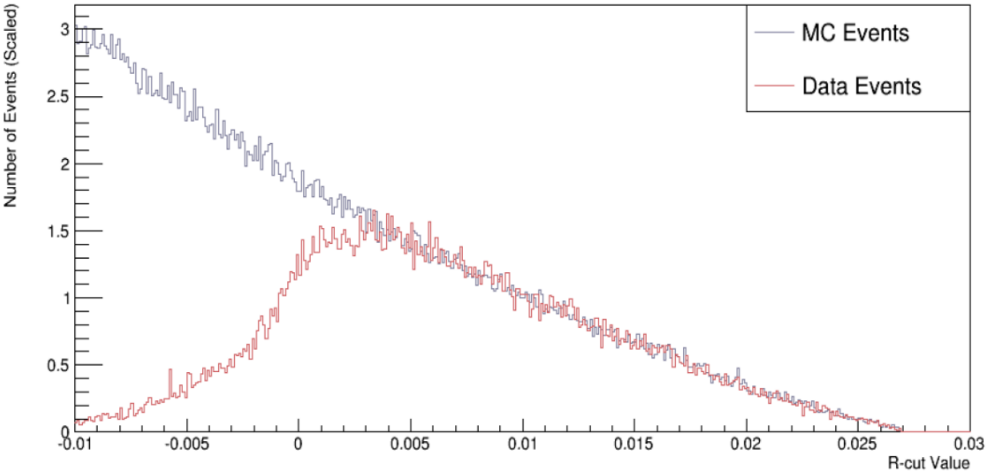

Figure 3.5: Comparison of the R-value distribution for data and Monte-Carlo. The data (red) and Monte-Carlo (blue) agree beyond 0.003. For this kinematic, all the events with R-value greater than 0.003 were selected as good events. The figure is extracted from [85].

than the one containing the LH_2 target. Figure 3.6 shows the vertex position distribution for LH_2 run and dummy run in the same kinematic. From the knowledge of the thickness of an Al window in dummy target (t^{Al}_{dummy}), the thickness of an Al window in LH_2 ($t^{Al}_{LH_2}$), the charge accumulated for LH_2 run (Q_{LH_2}), and the charge accumulated for dummy run (Q_{dummy}) one can determine the contribution from the end caps for LH_2 target for the given run as:

$$N^{Al}_{LH_2} = \left(\frac{N_{dummy}}{Q_{dummy} \times t^{Al}_{dummy}} \right) \left(t^{Al}_{LH_2} \times Q_{LH_2} \right) \tag{3.10}$$

Unfortunately, we acquired dummy runs for only 4 out of 9 kinematics (48-1, 48-2, 36-2, and 60-3). Instead of subtracting the contribution from dummy target, we selected the events with the vertex position in the interval [-6.5 cm , 6.5 cm] for all kinematics. The analysis by B.Karki [86] used the data from dummy target (for available kinematics) to show that the contribution from the Al windows are negligible (below 0.1%) for the vertex position within [-6.5 cm , 6.5 cm].

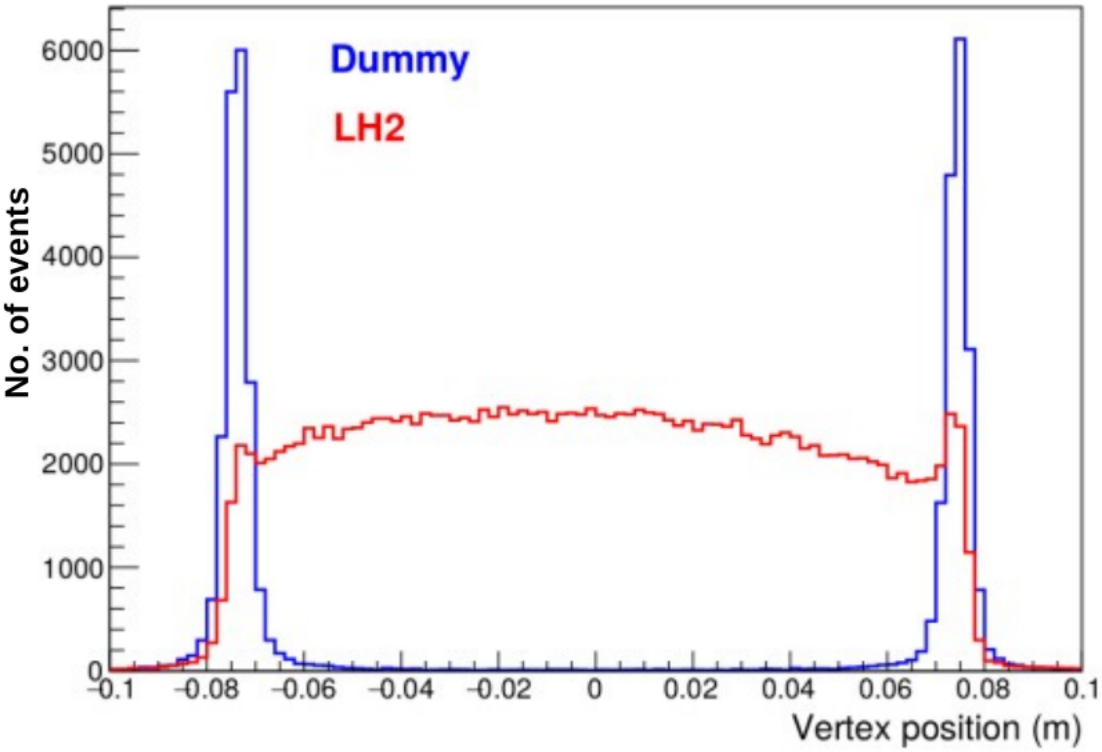

Figure 3.6: Vertex position distribution of the events from the dummy target in blue and LH_2 in red for kinematic 48-1. The peak on either side of distribution represents the events scattered off the end caps of the target. The difference in the number of events at the edge is due to the difference in thickness and beam charge for the two different targets.

3.3.3 Particle identification

The combination of S2&CER in coincidence forms the DIS trigger. The momentum threshold for e^- to produce the signal in Cherenkov is 17 MeV/c but for pions is about 4.8 GeV/c [67]. Hence, Cherenkov removes most of the π^- events. In Cherenkov, the signal from single-photon peaks around 100 ADC channel, and this one photo-electron peak represents the noise. To reject the false electrons in analysis the Cherenkov threshold is set at 150 ADC channel, represented by the blue line in Figure 3.7 (left).

Pions passing through the detector material ionize matter and produces secondary electrons called δ ray. The Cherenkov threshold of 1.5 photo-electron peak is not sufficient to remove all δ rays. Depending upon the kinematic up to 10% of the δ rays lie above the 150 ADC channel cut. To reject the δ rays, an additional cut is applied on the pion rejector (electromagnetic calorimeter) signal. The δ rays have low energy as compared to the DIS electrons. Based on the energy deposition on the pion rejector, δ rays can be removed from the analysis. Figure 3.7 (right) shows some fraction of low energy δ ray passes the Cherenkov threshold, but can be discriminated from DIS electron in the pion rejector. The low energy peak represents δ ray, while the peak at higher energy corresponds to DIS e^- events. The threshold cut of 600 ADC channel on the pion rejector total energy is applied for DIS event selection. An additional cut on pion rejector 1^{st} layer at 200 ADC channel is also applied. The combination of cuts on pion rejector and Cherenkov selects the e^- with more than 99% efficiency [74].

3.3.4 Single track cut

The tracking information (x_{fp}, y_{fp}, θ_{fp}, ϕ_{fp}, and x_{fp}) is provided by a pair of Vertical Drift Chambers (VDCs), described in section 2.3.7. As the charged particle passes through the VDC wire planes; it ionizes the gas on its path. The ions and ejected electrons drift to the wires producing a signal on a few adjacent wires. That group of wires forms a cluster.

The analysis by H.Rashad [87] shows that the track can be only reliably reconstructed if one of the following condition is justified.

- All 4 wire planes have a single cluster
- Only one wire plane has multiple cluster, the other 3 wire planes have a single cluster
- At most only two wire planes have multiple clusters, the other two have a single cluster

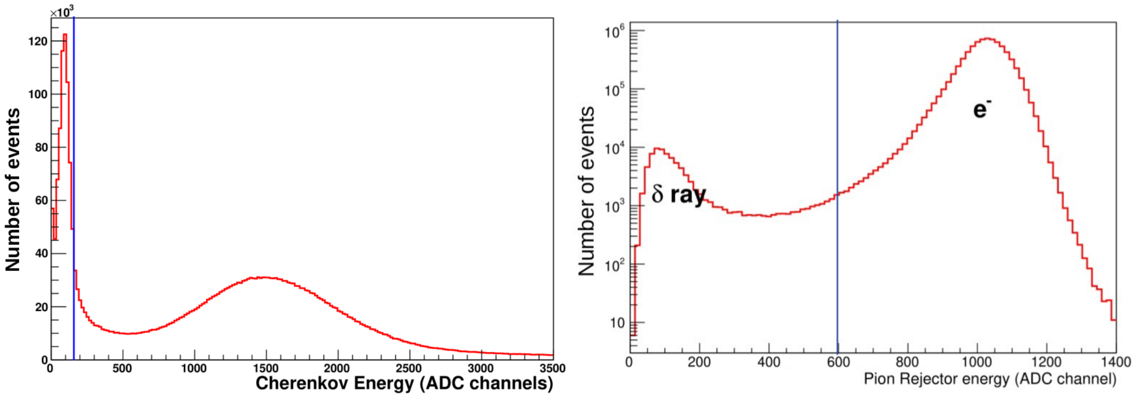

Figure 3.7: Left: Total energy distribution in the Cherenkov detector. The peak at lower energy corresponds to the single photo-electron peak (noise), while the higher energy peak represents mostly DIS electrons. The blue line corresponds to the 150 ADC channel threshold cut applied in analysis to select DIS electrons. Right: Total energy distribution in the pion rejector for events passing the Cherenkov cut. The low energy δ rays pass through the Cherenkov cut, so an additional cut on the energy deposited in the pion rejector is applied to discriminate between DIS electrons and δ rays. The blue vertical line at 600 ADC channel represents the pion rejector energy cut.

An event satisfying one of these three conditions is termed a single-track event. In our analysis, we require a single track cut. However, this cut sometime eliminates true DIS events. To account this loss, the number of DIS events is corrected by tracking efficiency $(n_{Tracking})$.

$$\eta_{Tracking} = \frac{N^{PID}_{multiTrack}}{N_{multiTrack}} \tag{3.11}$$

where $N_{multiTrack}$ is the number of events with more than one track i.e. events which can not be reliably reconstructed and $N^{PID}_{multiTrack}$ are the number of multi-track events passing the PID cut formed by Cherenkov and pion rejector. The tracking efficiency mostly depends on beam current for a given run, but the study by H.Rashad [87] showed that variation of tracking efficiency from one run to another is very small. So for the given kinematic, the mean value of of tracking efficiency is used. The tracking efficiencies for each kinematic are given in Table 3.1.

3.4 Trigger Efficiency

The DIS trigger was formed by S2 and Cherenkov in coincidence. To determine the efficiencies of these detectors, dedicated runs are taken.

- Cherenkov efficiency

  To determine the Cherenkov efficiency, events trigger by S0&S2 in coincidence are used. The Cherenkov lies between the scintillators S0 and S2 (see Figure 2.9). So every good electron triggering S0&S2 should leave a signal in Cherenkov if Cherenkov is 100% efficient. The sample of a good electron event is selected by using the pion rejector. The Cherenkov efficiency is then given by:

  $$\eta_{CER} = \frac{N_{S0\&S2\&CER\&PR}}{N_{S0\&S2\&PR}} \tag{3.12}$$

  where $N_{S0\&S2\&PR}$ is the sample of good electrons firing the S0&S2 and the pion rejector. $N_{S0\&S2\&CER\&PR}$ is the number of events firing the Cherenkov from the same sample of good electrons.

- S2 efficiency

  To determine the S2 efficiency, the run with trigger S0 and Cherenkov in coincidence (S0&CER) is used. The efficiency of S2 is given by the expression

  $$\eta_{S2} = \frac{N_{S0\&CER\&S2}}{N_{S0\&CER}} \tag{3.13}$$

  where $N_{S0\&CER}$ is the number of events triggered by S0&CER and $N_{S0\&CER\&S2}$ is number of events firing S2 from the sample of events triggered by S0&CER.

The S2 and Cherenkov efficiencies for each kinematic is given in Table 3.1. Both S2 and Cherenkov were more than 99.5% efficient throughout the period of our data taking.

3.5 Dead Time

The Data Acquisition (DAQ) takes some time to decide whether an event is of our interest or not and if it is a good event then additional time is required to save the event on tape. While the DAQ processes an event, it will be dead and will not accept a new event. This duration is termed as dead time. Due to the dead time, events of interest are missed. The dead time can be significant correction depending on the event rates for that kinematics. In order to minimize the dead time correction, a prescale factor is set in our trigger system. This prescale factor allows us to save an event after every certain number of good events. For instance, the prescale factor of 4 will save one event out of every 4 good events. Hence, prescale allows us to minimize the dead time by spending less time writing event on tape. Even after the prescale setting, there can be a few percent corrections (1-5%) needed due to dead time depending on the beam current. In our analysis, every run is corrected by its corresponding dead time.

The dead time is evaluated by the scaler system. Every events accepted by the trigger are counted even if they are not fully recorded. Counting is virtually dead time free. Events are counted as soon as they pass the trigger giving the number N_{raw}. Additionally, events that are fully recorded are also counted giving the number N_{Live}. Then the dead time (DT) can be computed as:

$$\mathrm{DT} = 1 - \frac{N_{Live}}{N_{Raw}} \tag{3.14}$$

The dead time and Live Time (LT) are equally used in this document, they are related as:

$$\mathrm{DT} + \mathrm{LT} = 1 \tag{3.15}$$

The average value of LT for each of the kinematic is given in Table 3.1.

3.6 Radiative Effects

The electron is a very light particle, as a result it easily loses its energy through radiation on its way. One of the major disadvantages of using the e^- beam is dealing with the radiative loss of energy. Broadly speaking, the radiative loss can be classified into two categories: external radiative loss and internal radiative loss.

3.6.1 External radiative loss

When an electron traverses through the medium, it will lose some of its energy through the Bremsstrahlung process, radiating a photon. If this energy loss is not at interaction vertex, then it is termed an external radiative loss. For instance, in our case electrons lose energy as they pass through the Al windows of the target cell and through LH_2. The amount of energy loss follows the statistical distribution is given by [88].

$$I(E_0, \Delta E, t_{mat}) = \frac{bt_{mat}}{\Delta E}\left(\frac{\Delta E}{E}\right)^{bt_{mat}} \tag{3.16}$$

where E_0 is the energy of an electron, ΔE is energy loss, t_{mat} is the material thickness (in units of radiation length) traversed, and b is a constant for a given target. For the H_2, b is about $\frac{4}{3}$. The distribution I(E_0, Δ E, t_{mat}) is normalized to 1, i.e.,

$$\int_0^{\Delta E} I(E_0, \Delta E, t_{mat})\, d(\Delta E) = 1 \tag{3.17}$$

If the energy loss for an individual event is computed as in Equation 3.18 then energy loss follows the distribution described by Equation 3.16.

$$\Delta E = E_0\, r^{\frac{1}{bt_{mat}}} \tag{3.18}$$

where r is uniformly generated in an interval [0,1]. The external radiative loss is handled by the GEANT4 toolkit in the Monte-Carlo, on an event by event basis. The energy loss is computed within the peaking approximation that is the photon emitted is in the same direction as the initial electron.

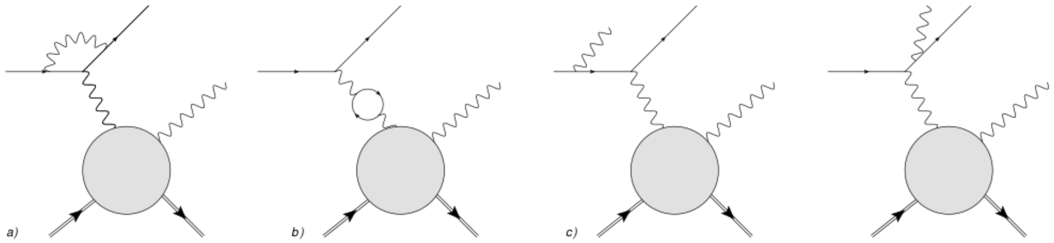

Figure 3.8: Illustration of the internal radiative correction (first-order) for DVCS process.

3.6.2 Internal radiative loss

Unlike in external radiative loss, in internal radiative loss, photons are emitted at interaction vertex. The emitted photons can be either real or virtual. The internal radiative loss is prominent in a leptonic part as compared to the proton side in the electron-proton scattering. All the radiative loss on the proton is ignored and this is good first order approximation as a proton is heavy. As the radiative effects only for the electron but not for a hadron (proton/pion) is considered, so corrections will be the same for DIS, DVMP, or DVCS process. Figure 3.8 shows the first-order internal radiative effects for the DVCS process. At first order there, are three radiative processes:

- The vertex correction [see Figure 3.8(a)]: a virtual photon is emitted by the incoming electron before the main scattering and is reabsorbed after the main scattering.
- The vacuum polarization [see Figure 3.8(b)]: a virtual photon splits into an electron-positron pair, which later recombines into a virtual photon.
- The internal Bremsstrahlung [see two right diagrams in Figure 3.8(c)]: a real photon is emitted either by an incoming or outgoing electron.

The connection between the experimentally measured cross-section (σ_{exp}) and the Born cross-section (σ_{Born}) can be written as [89]:

$$\sigma_{exp} = \sigma_{Born} \times \left(\frac{e^{\delta_{Brem}+\delta_{ver}}}{(1-\delta_{vac})^2} \right) \tag{3.19}$$

where δ_{vac}, δ_{Brem}, and δ_{ver} are the correction for vacuum polarization, Bremsstrahlung contribution, and vertex correction respectively.

$$\delta_{vac} = \frac{\alpha}{3\pi} \left[\ln\left(\frac{Q^2}{m_e^2}\right) - \frac{5}{3} \right] \tag{3.20}$$

$$\delta_{ver} = \frac{\alpha}{\pi} \left[\frac{3}{2}\ln\left(\frac{Q^2}{m_e^2}\right) - 2 + \frac{\pi^2}{6} - \frac{1}{2}\ln^2\left(\frac{Q^2}{me_e^2}\right) \right] \tag{3.21}$$

$$\delta_{Brem} = \frac{\alpha}{\pi} \left[\mathrm{Sp}\left(\cos\frac{\theta_e}{2}\right) - \frac{\pi^2}{3} + \frac{1}{2}\ln^2\left(\frac{Q^2}{m_e^2}\right) - \frac{1}{2}\ln^2\left(\frac{E_0}{E'}\right) \right] + \frac{a}{\pi}\ln\left(\frac{(\Delta E)^2}{E_0 E'}\right)\left(\ln\left(\frac{Q^2}{m_e^2}\right) - 1\right) \tag{3.22}$$

with α the QED fine structure constant, E' is scattered electron energy and Sp is the Spence's function defined as:

$$\mathrm{Sp}(z) = -\int_0^z \frac{\ln(1-t)dt}{t} \tag{3.23}$$

Equation 3.22 can be separated into two independent parts: one dependent on energy loss and another independent on ΔE such that:

$$e^{-\delta_{Brem}} \sim e^{-\delta_{Brem,0}} \times \left(\frac{\Delta E}{E_0}\right)^{\delta_{Brem,1}} \times \left(\frac{\Delta E}{E'}\right)^{\delta_{Brem,1}} \tag{3.24}$$

where the terms $\delta_{Brem,0}$ and $\delta_{Brem,1}$ are given by:

$$\delta_{Brem,0} = \frac{\alpha}{\pi} \left[\mathrm{Sp}\left(\cos\frac{\theta_e}{2}\right) - \frac{\pi^2}{3} + \frac{1}{2}\ln^2\left(\frac{Q^2}{m_e^2}\right) - \frac{1}{2}\ln^2\left(\frac{E_0}{E'}\right) \right] \tag{3.25}$$

$$\delta_{Brem,1} = \frac{a}{\pi} \left[\ln\left(\frac{Q^2}{m_e^2}\right) - 1 \right] \tag{3.26}$$

The energy losses $\left(\frac{\Delta E}{E_0}\right)^{\delta_{brem,1}}$ and $\left(\frac{\Delta E}{E'}\right)^{\delta_{brem,1}}$ follows the statistical distribution as described in Equation 3.19, with the radiator of thickness $\delta_{Brem,1}$. To reproduce the energy loss by internal Bremsstrahlung, this loss is computed in the Monte-Carlo simulation for every event, in a similar way as an external radiative loss given by Equation 3.18. But the internal Bremsstrahlung is computed twice for every event: one for incoming and other for outgoing electron.

The correction related to emission and re-absorption of electron-positron pairs from virtual photons within a loop (see Figure 3.8(b)) is given by the expression:

$$\eta_{virt} = \frac{e^{\delta_{Brem,0}+\delta_{ver}}}{(1-\delta_{vac})^2} \tag{3.27}$$

The term η_{virt} mostly depends on Q^2 and hence is computed theoretically using Equation 3.27 for every kinematics. The values of η_{virt} used for different kinematics are given in Table 3.1.

3.7 Monte-Carlo Simulation

After scattering at vertex, but before being detected in the spectrometer, the e^- travels a few centimeter in dense material. Therefore the scattered electron might lose energy before being detected. Similarly, the incident beam also loses some energy before scattering due to the radiative loss. As a consequence, events that are detected within the spectrometer acceptance might have the energy and angle at vertex far from the HRS acceptance (see Figure 3.9). Similarly, events with vertex kinematics within the HRS acceptance end up not being detected by the HRS. Unlike in data, the vertex variables can be accessed in Monte-Carlo simulation. In order to compute the phase space factor Γ_{DIS} and the term α (see Equation 3.32) the simulation is used.

The major steps in Monte-Carlo simulation are: generate the DIS event, account for radiative losses, and test if the measured events are in spectrometer acceptance. First, the vertex position is generated within the target length (15 cm). This vertex position determines the distance traversed by the beam in the target. Knowing the distance traverse, the external radiative loss is computed both in the Al window and the LH_2 target. The

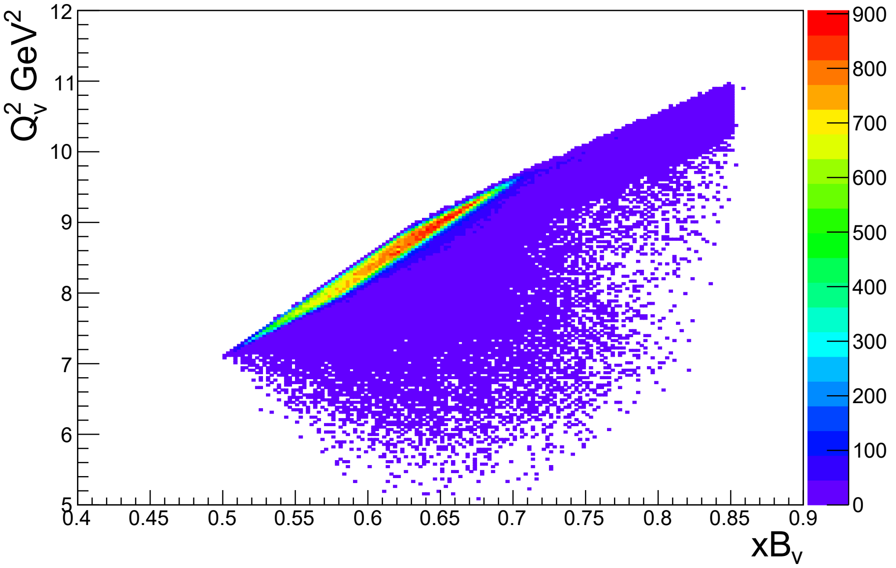

Figure 3.9: The distribution of variables, Q^2 and x_B at vertex for the events detected in spectrometer. The dense portion represents the HRS acceptance for which the incident and scattered electron energies are not significantly modified by radiative effects. Due to the radiative loss, the event can migrate either in or out from the HRS acceptance.

kinematic variables (x_B, Q^2) are generated uniformly in a window larger than the nominal spectrometer acceptance window.

$$x_B \ \epsilon \,[0,\ 1] \tag{3.28}$$

$$Q^2 \ \epsilon \ [0,\ 3 \times Q^2_{Nominal}] \tag{3.29}$$

where “Nominal” stands for the central value of the given kinematic setting. The energy and angles of the scattered electron are deduced using the energy of the beam, x_B, and Q^2. Later internal radiative losses are computed to both incoming and scattered electron as described in section 3.6.2. All the major steps in Monte-Carlo simulation for generating the DIS event are shown in Figure 3.10. Once the scattered e^- reaches the spectrometer, the vertex position is smeared to take the spectrometer resolution effect.

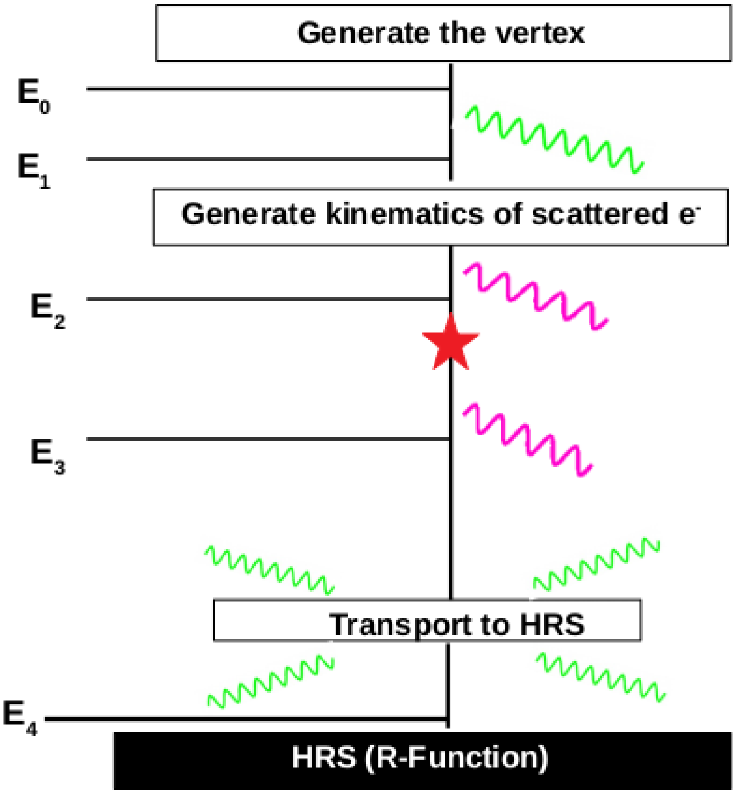

Figure 3.10: Schematic representation of the steps involved in Monte-Carlo simulation for generating DIS events. The red star represents the vertex. The internal radiative correction before and after the vertex is represented by magenta color photon. The external radiation are represented by the green photons. The E_i represent the e^- energy after the radiative loss.

The DIS phase space is computed as:

$$\Gamma_{DIS} = \left(\frac{N_{accept}}{N_{gen}}\right)\Gamma_{MC} \tag{3.30}$$

where $\Gamma_{MC} = \Delta x_B \times \Delta Q^2 \times \Delta\phi$, N_{gen} is the total number of generated events. N_{accept} is the total number of events passing through the set of analysis cuts, same as the DIS event selection.

3.8 Parametrization of DIS Structure Functions

For the data normalization study, the extracted DIS cross-section from E12-06-114 experiment is compared with the existing world's data. The DIS cross-section can be computed using Equation 1.9, if the structure functions:F_1 (x_B, Q^2) and F_2 (x_B, Q^2) are known at a given kinematics. These structure functions can be extracted from experimentally measured observables. To evaluate F_1 (x_B, Q^2) and F_2 (x_B, Q^2) at our kinematic points, we opted to use the parameterization suggested by E.Christy et al. [90]. The main reasons to choose this parameterization of structure functions are:

- The longitudinal (L) to transverse (T) cross-section ratio, i.e., R= ($\frac{\sigma_{\mathrm{L}}}{\sigma_{\mathrm{T}}}$), is extracted by fitting the L/T separated cross-section data rather than using the educated guess for the value of R as in Ref. [91].

- The data set used for fitting is a precision data set, covering a wide kinematic range very close to our kinematics.

The value R is related to the structure function F_1 and F_2 as:

$$R = \frac{\sigma_L}{\sigma_T} = \left[\left(\frac{F_2}{2x_BF_1}\right)\left(1 + \frac{4M^2x_B^2}{Q^2}\right)\right] - 1 \tag{3.31}$$

The structure function F_1 is the purely transverse response, so it can be computed after knowing σ_T, while F_2 (transverse + longitudinal) can be computed using Equation 3.31 once R is extracted.

3.9 Variation of Cross-Section within a Bin

To extract the experimental cross-section, the number of DIS events in a particular kinematic bin was selected. Due to our choice of single large bin in x_B and Q^2, the cross-section changes within the bin. This makes it difficult to compare our extracted cross-section with a theoretical one, defined at a nominal kinematic point. The experimentally extracted correction is corrected by the term α to compare with the theoretical cross-section from the world's data at given x_B and Q^2.

$$\alpha(x_B, Q^2) = \left(\frac{1}{\left(\frac{d^2\sigma}{dx_B\, dQ^2}\right)_{Nominal}} \right) \times \frac{1}{N_{accept}} \times \sum_i \left(\frac{d^2\sigma}{dx_B\, dQ^2} \right)_i \tag{3.32}$$

where $\left(\frac{d^2\sigma}{dx_B dQ^2}\right)_i$, and $\left(\frac{d^2\sigma}{dx_B dQ^2}\right)_{Nominal}$ are the cross-section (using E. Christy and P. Bosted parametrization) for i^{th} event and at the nominal value, respectively. The nominal value of kinematic is the point where we want to compare experimental and theoretical cross-section. Table 3.1 shows the value α used in DIS cross-section analysis for different kinematics.

3.10 Result

We extracted the DIS cross-section for all nine kinematics for experiment E12-06-114. In this section, the stability of extracted cross-section within a kinematic and overall normalization by comparing with world data will be discussed.

3.10.1 Trigger interference

The data for the experiment E12-16-114 were taken in three different run periods: the Fall 2014 (36-1), the Spring 2016 ((48-1, 48-2, 48-3, and 48-4), and the Fall 2016 (36-2, 36-3, 60-1, 60-3). In addition to the DVCS and DIS triggers, an additional S0&CER trigger was also present during the Spring 2016 kinematics. In the Fall 2016, only the DVCS and DIS trigger were present. Through our DIS cross-section analysis, we found that there was interference between DIS and S0&CER triggers. Some of the electrons triggered by S0&CER arrived too late to be registered by DIS trigger despite being a DIS event [92] and [93]. The events with low momentum (relative to peak value) can potentially miss the DIS trigger whenever the S0&CER was triggered due to delay in time. Depending on the prescale setting on the S0&CER trigger, we missed up to 15 % DIS events. To compensate for the missed DIS events, a correction was applied to raw DIS events. For the correction, a sample of events triggered by S0&CER only (exclusive), but passing the same cuts used to select the DIS events were added to DIS events. Figure 3.11 shows the correction introduced from exclusive S0&CER events reduced the disagreement in DIS cross-section between the runs with and without the S0&CER from 15% to 3%. This correction equally holds for the rest of the kinematics where there was interference between DIS and S0&CER trigger.

The extracted differential cross-section was stable within 1% over the runs for the kinematics without the S0&CER trigger (Fall 2016). But for the Fall 2014 and the Spring 2016 data set, stability is within 3%. The typical stability plot for kinematic without S0&CER trigger is shown in Figure 3.12, and kinematic with S0&CER trigger is shown in Figure 3.11 by the blue triangles. This stability test helps us to select the good runs and to understand the uniformity in our data while taking data in different experimental configurations within the same kinematics. The runs that were 3σ away from the root mean square of the cross-section distribution of each kinematic were excluded for DVCS or π^0 analysis.

3.10.2 Comparison with world data

The cross-section is extracted using 3 different simulations for the systematic study. The result from each simulations are compared with the model or theoretical cross-section from [90]. Here are the main features of the 3 different simulations:

- Simulation A:

  This is a GEANT4 simulation used by E12-06-114 collaboration for the DVCS and π^0 cross-section analysis. The same simulation was modified for DIS event generation. While transporting the particles from the vertex to the detectors all

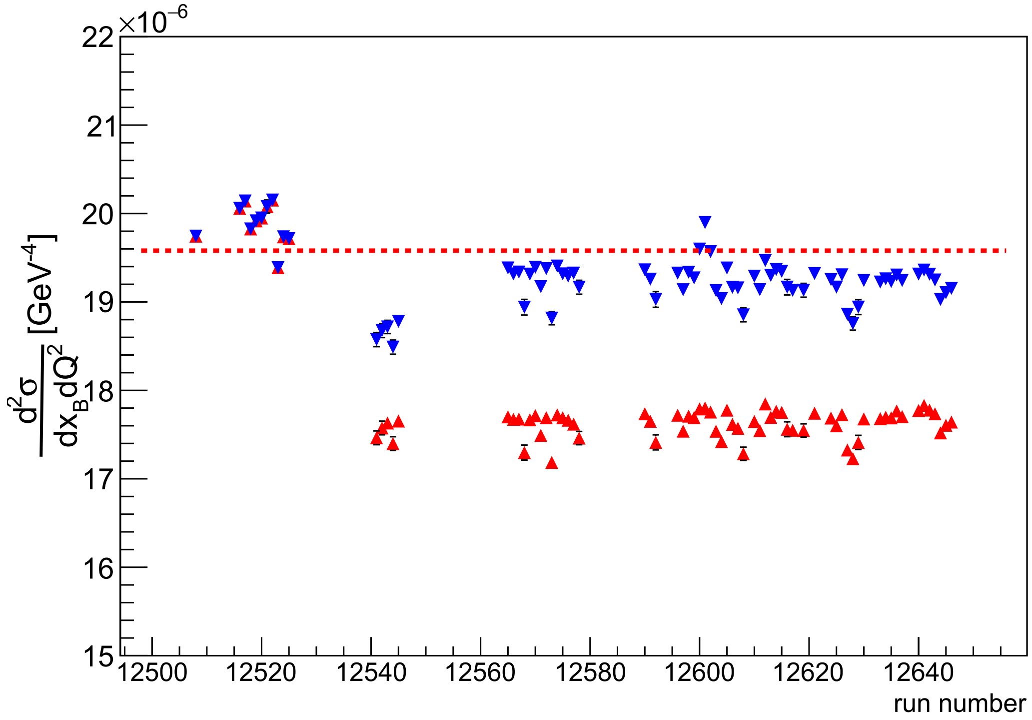

Figure 3.11: The effect of including the missing events in DIS cross-section analysis for kinematic 48-1. The red triangles represent the cross-sections without correcting the DIS events with missing events from S0&CER trigger. The cross-section for runs around 12520 (without S0&CER trigger) is about 15% higher than the rest runs with S0&CER trigger. The blue triangles represent the cross-sections for the same set of runs after correcting the DIS events. The agreement between the runs with and without the S0&CER trigger is below 3%. The dashed red line is the theoretical cross-section for this kinematic.

material in between the scattering chamber and the spectrometer entrance window is considered. However this simulation does not consider the magnetic field effect inside the spectrometer. The radiative corrections are done as described in section 3.6.

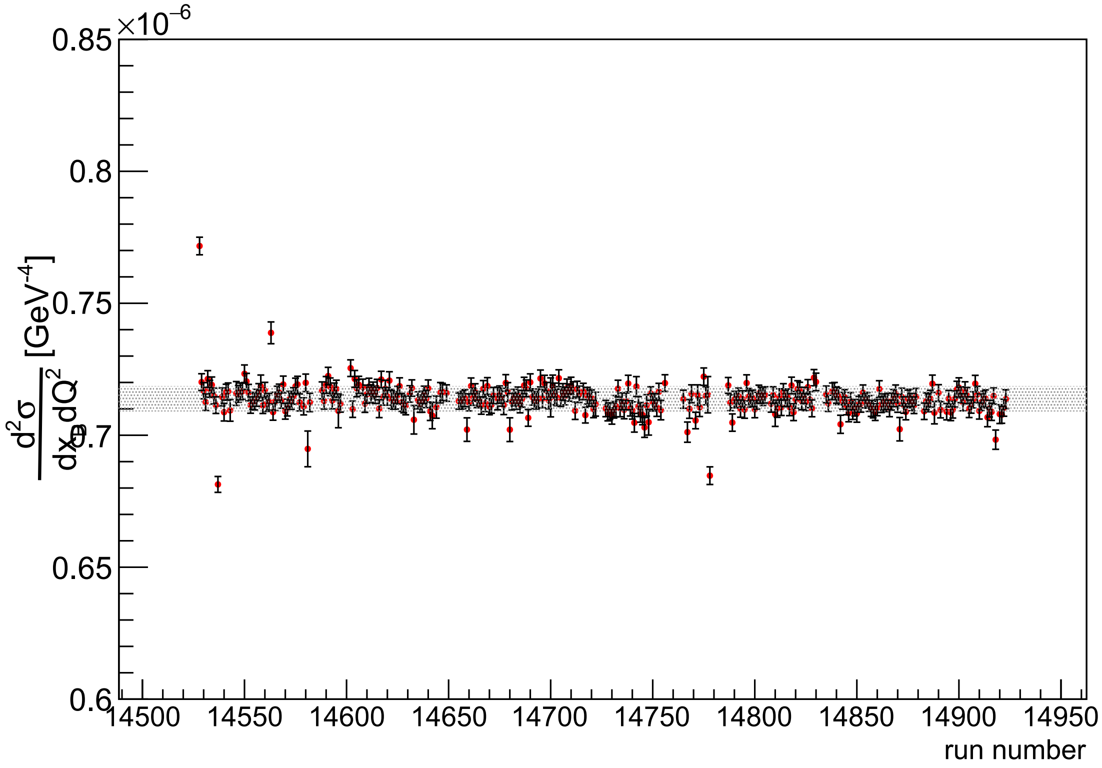

Figure 3.12: Experimentally extracted DIS cross-section for all runs within the same kinematics. The shaded region corresponds to the root mean square of the distribution. Left: For kinematic 60-3, the extracted cross-section is stable within 0.5%, expect few outliers which are excluded in π^0 analysis.

- Simulation B:

  It is a standard Hall C DIS event generator commonly called SIMC [83]. The main feature of this simulation is, it contains the full description of the spectrometer including the transport of the scattered particle through the magnetic filed and detection in the focal plane of the detector. The internal radiative correction are implemented differently compared to a simulation A (for more details see document by E.Christy [94]). The SIMC is limited for some kinematics due to the absence of the magnetic field map due to the detuned setting for the quadrupole Q1.

- Simulation C:

  This simulation is more close to simulation A, the only difference is that it does not use the GEANT4 tool-kit to compute the energy loss by the incoming or scattered electron [95].

Table 3.2 shows the ratio of theoretical or model cross-section σ_M to extracted DIS cross-section[9] (σ_D) for 9 different kinematics using 3 different simulations (A, B, C). The 4^{th} and 5^{th} columns of Table 3.2 are the results extracted by me while the 6^{th} column is taken from [95]. Comparing results in Table 3.2 along one line is an indication of systematic error rising from the solid angle estimation. We estimated this variation to be 2%. On average, the measured cross-sections are 4% smaller than the world data with the total systematic uncertainty (dispersion) of 4%. The different sources of experimental systematic uncertainty are given in Table 3.3. The total uncertainty for electron detection is 3.5%. The uncertainty in HRS acceptance is computed by studying the DIS cross-section variation with the different values of R-cut [85]. The DIS model used to extract the cross-section (E. Christy and P. Bosted parametrization) at our kinematics interpolates the existing data. The uncertainty associated with the interpolation is 2% [90]. With additional 2% uncertainty from DIS model results total systematic uncertainties to 4% which is equivalent to the dispersion of the measured cross-section compared to expected cross-section (RMS of the last column of Table 3.2).

After our rigorous analysis, we concluded that 4% below the reference cross-section is due to the inefficiency of our DIS trigger. We strongly believe that this inefficiency does not affect the DVCS/π^0 analysis. As for the DVCS/π^0 event selection, the trigger information is not used in the same way as in the DIS event selection. The dead time for DVCS trigger

---

[9] For simplicity it is represented with σ but its actually differential cross-section

Table 3.2: Comparison of model and extracted DIS cross-section results for 9 different kinematics of the experiment E12-06-114. For the systematic study, three different simulations were used to compute the solid angle. In average the extracted cross-section is 4% below the model cross-section from world data with a systematic uncertainty of 4%. The third column represents the quadrupole Q1 status for different run periods. Only for the kinematics 36-1 and 48-1 the Q1 was fully functional (Unsat.). For the Spring 2016, Q1 was not in tune (detuned) with rest magnets. But the optics calibration data were taken. For the Fall 2016, a different quadrupole was used from SOS. The Q1 saturation was saturated between 1-7 % in different kinematics.

Kinematic	Run Period	Q1 status	$\left(\frac{\sigma_M}{\sigma_D}\right)_A$	$\left(\frac{\sigma_M}{\sigma_D}\right)_B$	$\left(\frac{\sigma_M}{\sigma_D}\right)_C$	Average
36-1	Fall 2014	Unsat.	0.95	0.97	0.99	0.97
36-2	Fall 2016	SOS (1%)	1.04	1.06	1.06	1.05
36-3	Fall 2014	SOS (7%)	1.04	1.07	1.06	1.06
48-1	Spring 2016	Unsat.	1.03	1.06	1.00	1.03
48-2	Spring 2016	detuned.	1.06	–	1.06	1.06
48-3	Spring 2016	detuned.	1.06	–	1.09	1.07
48-4	Spring 2016	detuned.	1.09	–	1.09	1.09
60-1	Fall ’16	SOS (4%)	1.01	1.06	1.06	1.04
60-3	Fall ’16	SOS (1%)	0.98	1.02	1.03	1.01
Average			**1.03 ± 0.04**	**1.04 ± 0.04**	**1.05 ± 0.03**	**1.04 ± 0.04**

is different than that for DIS but systematic on them is about the same. The radiative correction is only applied for the leptonic part, but not on proton which is a good first order approximation; as proton is relatively heavier so less radiative loses. The total systematic from electron side (3.5%) is taken into account for DVCS/π^0 analysis.

Table 3.3: Sources of experimental systematic errors for DIS cross-section. Total uncertainty in electron detection is 3.5%. The reference DIS cross-section from E. Christy and P. Bosted [90] has 2% systematic uncertainty resulting total DIS systematic to 4%.

Systematic errors	value (%)
Luminosity and dead time	1.6
Radiative correction	2.0
HRS acceptance (R-cut)	1.0
HRS multi-track correction	0.5
HRS electron identification	0.5
Solid angle (multiple simulations)	2
Quadratic total	**3.5**
Model cross-section	2
Quadratic total (DIS)	**4**

4 DATA ANALYSIS AND MONTE-CARLO SIMULATION

The procedure for detecting the electron using the spectrometer is described in the previous chapter. This chapter will briefly explain the procedure to extract the photon information from the raw calorimeter signals. Each of the calorimeter blocks is equipped with an Analog Ring Sampler (ARS) as described in section 2.6. The calorimeter analysis is done in two steps: first, the ARS waveforms are analyzed to extract the amplitude and arrival time of the signal of each block. This process is called waveform analysis. The second step of the calorimeter analysis is to take the information from multiple adjacent blocks to reconstitute the total energy of the photons. Because the Molière radius of PbF_2 is comparable to the transverse size of the block, a photon entering the center of a given block leaves its energy to eight adjacent blocks. The process of reconstructing the photon's energy from the signals of many blocks is called clustering. The clustering gives the position and energy information of an incident photon.

4.1 Waveform Analysis

The waveform analysis algorithm assumes that the shape of the signal in each block of the calorimeter is independent of the amplitude [77]. Depending on the energy deposited in the block, signals from a given PMT are related to each other by a scaling factor. Thus, the ARS pulses can be fitted with reference shapes by adjusting their amplitudes and arrival time to match the raw data. The reference shapes are the average ARS pulses of each block.

The reference shapes of each PMT are determined using elastic calibration data acquired at low current (5 μA) that is configuration where pile-up events are rare. As the reference shapes are critical for the waveform analysis, they were extracted and updated frequently (5 times) during the run period of this experiment. The study by M. Dlamini [76] has shown that there is no significant change in reference shapes between the two years of data taking except for a few blocks. In this section, I will briefly describe the waveform analysis procedure.

4.1.1 Baseline fit

The first part of waveform analysis is to check if photon signal is measured by the calorimeter block. Indeed if an electron is detected by the HRS and a photon is detected in the calorimeter, signal from all the blocks of the calorimeter is written to tape. For this purpose, the ARS signal is fitted with the noise, baseline (b), to minimize the functional:

$$\chi^2 = \sum_{i_{min}}^{i_{max}} (x_i - b)^2 \tag{4.1}$$

The minimization yields χ^2 and the best value of b as:

$$b = \frac{1}{i_{max} - i_{min}} \sum_{i_{min}}^{i_{max}} (x_i) \tag{4.2}$$

where x_i is the ARS signal in bin i, i is the bin number of the ARS signal.

Instead of analyzing the entire 128 ns ARS window, the analysis iss limited between the interval, i_{max} - i_{min} = 80 ns. The ARS signals close to 0 and 128 ns do not contain any useful information, so reducing the time interval makes the analysis more efficient and reduces noise. The χ^2 obtained after minimization is then compared with the set global threshold, χ^2_0 (see Section 4.1.4). If χ^2 is smaller than χ^2_0, then the algorithm decides there is no real signal, and the event is ignored. Figure 4.1 shows a case with no signal where the baseline fit is sufficient to fit the ARS signal.

4.1.2 Single pulse fit

Once the baseline fit confirms that there is a potential photon signal, then the ARS raw signal is fitted with a single pulse. This is done by minimizing the χ^2:

$$\chi^2(t_1, a_1, b) = \sum_{i_{min}}^{i_{max}} \left(x_i - a_1 h_{i-t_1} - b\right)^2 \tag{4.3}$$

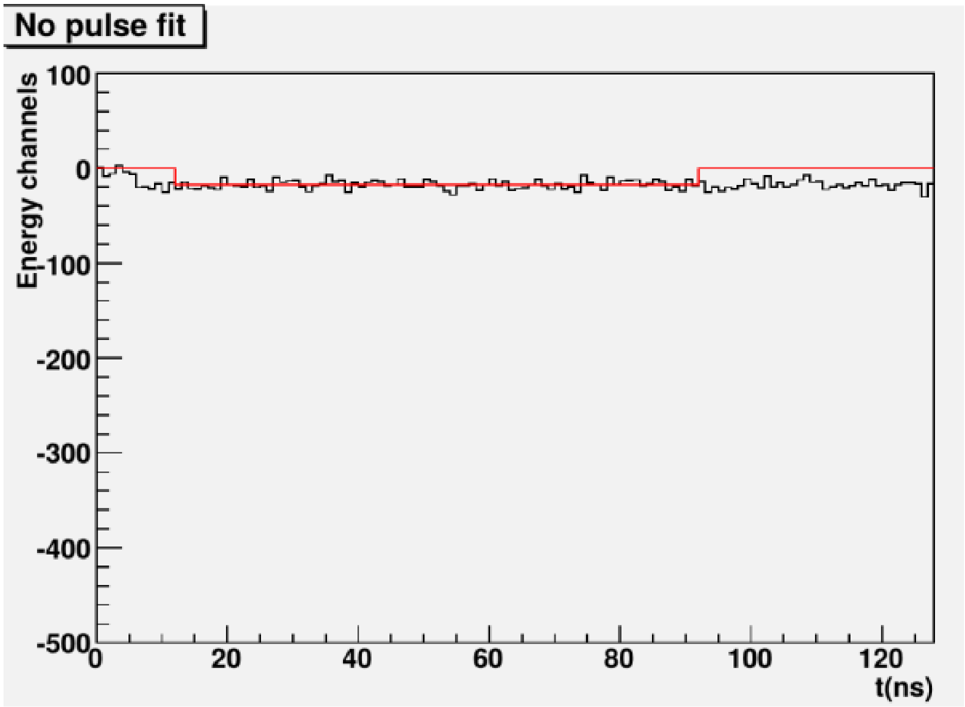

Figure 4.1: Illustration of baseline fit during the waveform analysis. The ARS raw signal in black is fitted with a baseline in red. This represents a case with no signal.

where h_i is the reference shape, t_1 is the arrival time, a_1 is amplitude, and b represents the baseline. The one pulse fit yields a_1, b, t_1 and χ^2 values that minimizes Equation 4.3. Again like in the previous step, the evaluated χ^2 is compared to a preset global value, χ_1^2 (see Section 4.1.4). If χ^2 is smaller than χ_1^2, then single pulse fitting is regarded as accurate. Otherwise, the two pulses fitting is invoked. Figure 4.2 shows a waveform analysis with a single pulse.

4.1.3 Two pulse fit

If one pulse fit is not adequate to reproduce the signal ($\chi^2 > \chi_1^2$), then the raw signal is fitted with two pulses. The idea is to minimize Equation 4.4 to best estimate the values of

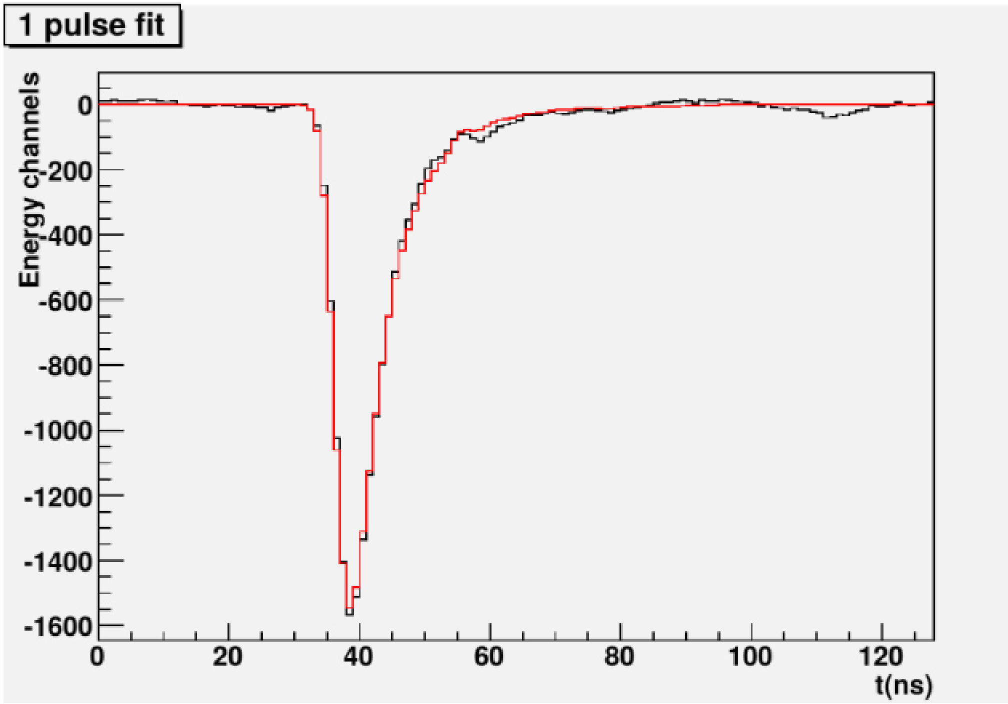

Figure 4.2: An example of waveform analysis with a single pulse fit. The ARS raw signal in black is fitted with a single pulse in red.

t_1, t_2, a_1, a_2, and b.

$$\chi^2(t_1,t_2,a_1,a_2,b) = \sum_{i_{min}}^{i_{max}} \left(x_i - a_1 h_{i-t_1} - a_2 h_{i-t_2} - b\right)^2 \tag{4.4}$$

The two pulse fit can not discriminate between the two signals if they are separated by less than 4 ns. The pile-up events for our kinematics are very small (below 5%), so the two-pulse fit is sufficient; there is no requirement for a three-pulse fit [81]. Figure 4.4 shows how the ARS can be useful to disentangle pile-up events.

4.1.4 Global thresholds

The values of χ_0^2 and χ_1^2 are determined by studying the variation of different variables with respect to χ_0^2 and χ_1^2. Figure 4.4 shows an example of such a study for the energy resolution of calorimeter at different values of χ_0^2. A similar analysis of other variables: W^2

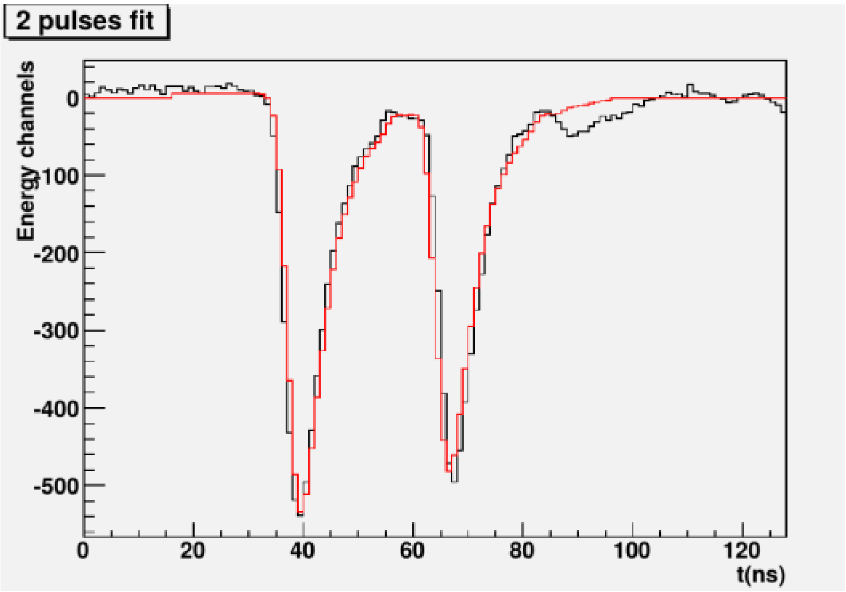

Figure 4.3: An illustration of the two pulse fit of the ARS signal. ARS allows the separation of the two signals if they are more than four ns apart. This would not be possible only with the ADC.

with elastic data, π^0 invariant mass etc. showed a plateau below the threshold followed by a steep rise above that threshold. The combined analysis of these variables is used to infer χ_0^2 and χ_1^2 threshold. For the simplicity values of χ_0^2 and χ_1^2 are converted from ADC channel to MeV using the calorimeter energy calibration coefficients. The optimized values for χ_0^2 and χ_1^2 are 60 MeV and 300 MeV, respectively [81].

4.2 Calorimeter Calibration

The amplitude of a signal from the waveform analysis is in some ARS channel units. Its relationship to the amount of energy deposited in the block depends on multiple efficiency factors like the critical transmission, property of the block, the amplification of the PMT (depending on high voltage), etc. Through the calorimeter calibration, the coefficients corresponding to the individual blocks are determined. In practice, the ARS

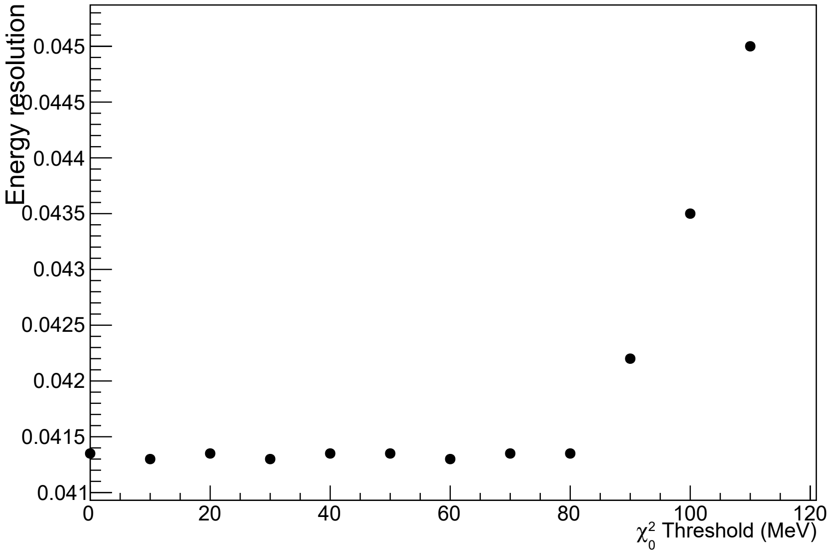

Figure 4.4: Variation of the calorimeter energy resolution as the function of χ_0^2. Below the 80 MeV, the resolution is stable, and above 80 MeV, it starts to degrade. The conservative value of 60 MeV was chosen as χ_0^2 threshold after a similar analysis using other variables. The figure was taken from [81].

signal amplitude is related to the energy through an overall calibration coefficient. The coefficients from calibration also help to tune the High Voltage (HV) of the PMTs such that for the same energy deposition, every block across the calorimeter produces the same raw ARS response. This allows us to implement a global energy threshold cut to remove the noise instead of having a block specific threshold. We adopted two different ways for calorimeter calibration.

4.2.1 Elastic calibration

The elastic calibration is performed with the electron-proton elastic scattering data. The elastically scattered electron is detected in the calorimeter and proton on the spectrometer. The elastic kinematic is used to determine the energy of the j^{th} scattered electron (E_j). If A_i^j is the amplitude of a j^{th} event in the i^{th} block of calorimeter, then energy deposited in calorimeter can be written as:

$$E^j = \sum_{i=0}^{208} C_i A_i^j \tag{4.5}$$

where C_i's are the unknown calorimeter coefficients that relate raw ARS signal to energy. This can be done by minimizing the given function for each value of C_i.

$$\chi^2 = \sum_{j=0}^{Nevents} \left(E_j - \sum_{i=0}^{208} C_i A_i^j \right) \tag{4.6}$$

The calorimeter blocks suffer radiation damage after long continuous use. As a consequence, the relationship between energy deposited in the block and the resulting ARS amplitude changes with time, and the calibration coefficients needs to be adjusted. In order to account for the radiation damage, several elastic calibrations were performed (5 times) during the DVCS3 run period. Through the elastic calibration the energy and angular resolution of the calorimeter was determined. The study by M. Dlamini [76] found a 3% energy resolution for the electrons of average energy 7.0 GeV. The same study showed angular resolution, both vertical and horizontal, to be about 2 mrad when the calorimeter was placed 6 m away from the target.

4.2.2 Calibration using π^0

The elastic calibration of the calorimeter is an invasive procedure and consumes about a day of data taking. Hence, the elastic calibration cannot be frequently afforded. The typical gap between two elastic calibrations is 20 days. In between two elastic calibrations, the gains of the calorimeter blocks change due to the radiation exposure. To account for the change in the gain of the calorimeter blocks, the complimentary procedure using π^0 events was implemented. This method is non-invasive and relies on the detection of the two decayed photons from π^0. The calibration coefficient of each block is adjusted on a

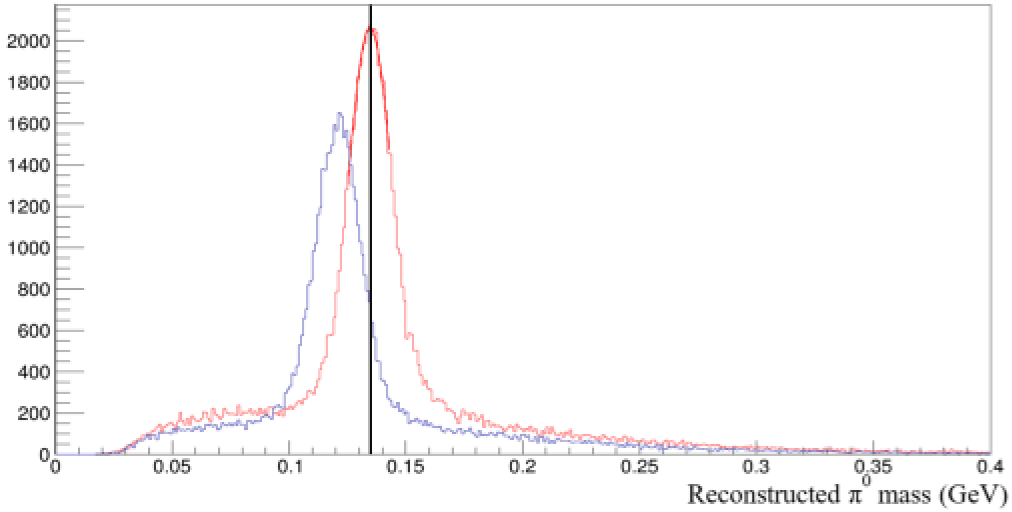

Figure 4.5: The reconstructed invariant mass of π^0 from $ep \rightarrow e'p'\pi^0$ channel. The blue curve and the red curve are before and after the π^0 calibration. The mean of invariant mass after the calibration is aligned with the expected value of 0.135 GeV, as shown by a black line. The resolution is improved by 3%. The figure is taken from [81].

daily basis so that the invariant mass of π^0 can be recovered at 0.135 GeV. Further detail for this procedure can be found in the thesis of F. Geogres [81]. Figure 4.5 shows the reconstructed pions invariant mass before and after π^0 calibration. For most of the blocks, the correction was not greater than 30%, but for the few blocks it was up to 300% between two elastic calibrations (about a month) [81].

4.3 Clustering Algorithm

As the photon traverses through the PbF_2 blocks of the calorimeter, it loses its energy. If the photon strikes at center of a block, then most of its energy (about 90%) is contained within that central block. But depending on the position of the hit on the block, the photon energy might distributed within 9 adjacent blocks. The group of blocks recording the signal from the same event is called a cluster. In some cases, multiple particles can hit the calorimeter at the same time; for instance, two decayed photons from π^0. This will give rise to multiple clusters within the calorimeter for one event. The clustering algorithm determines the position of a photon in the calorimeter as well as its energy. For each of the kinematic, clustering threshold is assigned well below the expected signal to discriminate the photon signal from noise. For kinematic 60-1 and kinematic 60-3, the clustering threshold is set at 0.8 and 1.0 GeV, respectively.

For the given spectrometer-calorimeter coincidence time window[10], the clustering algorithm first finds the impact point, where the energy deposition is maximum. Then it computes every possible combination of 4 blocks (see red boxes in Figure 4.6, the number inside blocks corresponds to the energy deposited by the photon). For each combination of 4 adjacent blocks, the total deposited energy is computed. If the sum of the energies deposited in 4 adjacent blocks is greater than the set threshold, then the cluster is saved for further analysis. There can be a possibility that a single block may belong to multiple groups of 4 blocks. Out of all possible 4 blocks combination, the right one is picked based on the fact that the energy lost by a photon will be maximum in the central block, and the energy in adjacent blocks gradually decreases. For each cluster, the total energy is given by;

$$E_{cluster} = \sum_i C_i A_i; \tag{4.7}$$

where C_i and A_i are calibration coefficient and signal amplitude for the i^{th} block, respectively. The cellular automata algorithm [96] used in clustering can distinguish between two clusters arriving at the same time, close to each other in distance.

The second part of the clustering algorithm is to find the position of the photon in the calorimeter (x_{clust}, y_{clust}). It is calculated as a weighted sum of blocks positions x_i (y_{clust} is

---

[10] the photon must be within ±3 ns coincidence window i.e. 3 σ of spectrometer-calorimeter time resolution

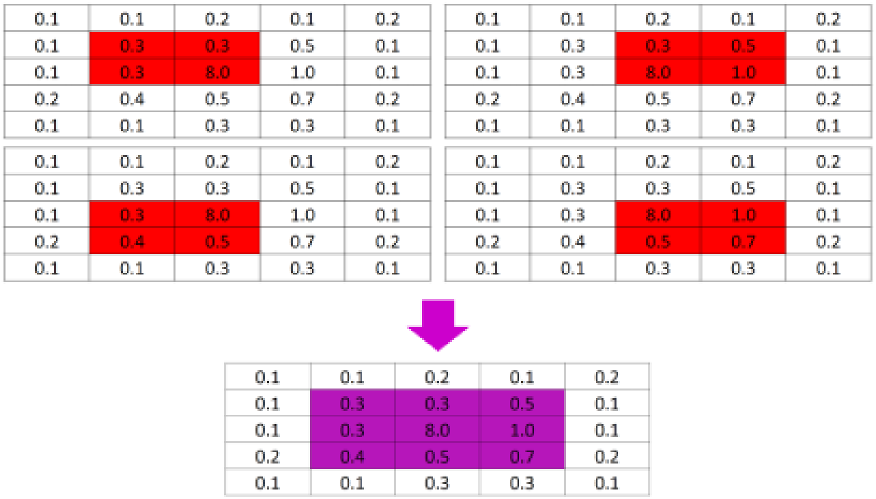

0.1	0.1	0.2	0.1	0.2
0.1	0.3	0.3	0.5	0.1
0.1	0.3	8.0	1.0	0.1
0.2	0.4	0.5	0.7	0.2
0.1	0.1	0.3	0.3	0.1

0.1	0.1	0.2	0.1	0.2
0.1	0.3	0.3	0.5	0.1
0.1	0.3	8.0	1.0	0.1
0.2	0.4	0.5	0.7	0.2
0.1	0.1	0.3	0.3	0.1

0.1	0.1	0.2	0.1	0.2
0.1	0.3	0.3	0.5	0.1
0.1	0.3	8.0	1.0	0.1
0.2	0.4	0.5	0.7	0.2
0.1	0.1	0.3	0.3	0.1

0.1	0.1	0.2	0.1	0.2
0.1	0.3	0.3	0.5	0.1
0.1	0.3	8.0	1.0	0.1
0.2	0.4	0.5	0.7	0.2
0.1	0.1	0.3	0.3	0.1

0.1	0.1	0.2	0.1	0.2
0.1	0.3	0.3	0.5	0.1
0.1	0.3	8.0	1.0	0.1
0.2	0.4	0.5	0.7	0.2
0.1	0.1	0.3	0.3	0.1

Figure 4.6: Illustration of the identifying the cluster to reconstruct the photon. The large rectangles represent the same portion of the calorimeter and small rectangles are calorimeter blocks with the amount of energy deposited in it by an event. Top: four different combinations of 4 blocks can be made such that the energy deposited is larger than the set threshold. But a particular block can fall into multiple groups as represented by the red-colored portion. The clustering algorithm picks the right one based on the fact that most of the energy is deposited at the central block and energy is photon is calculated by summing up 9 adjacent blocks shown by the purple color. The figure is taken from [81].

determined in a similar way).

$$x_{clust} = \frac{\sum_i w_i x_i}{\sum_i w_i}, \tag{4.8}$$

The weights w_i are assigned as the logarithm of the relative energy deposited in each block.

$$w_i = \text{Max.}\left[0, W_0 + \log\left(\frac{E_i}{E}\right)\right] \tag{4.9}$$

The logarithmic weighting factor takes into account the fact that energy deposition decreases exponentially with distance from the impact point. Near the impact point, the relative energy deposited is large so does the weight, and the weight is smaller the farther from the central value. The term W_0 provides an additional tuning of the relative weight. For large W_0 ($W_0 \to \infty$), despite relative energy deposited the weight becomes uniform. But for a small W_0, the block with larger relative energy gets a larger weight. Using the Monte-Carlo simulation and elastic data, the value of W_0 is estimated to be 4.3 [81].

The previous calculation of the clustered position was based on the assumption that the shower starts at the surface of the calorimeter. But in practice, shower only starts after the photon traverses certain distance inside the calorimeter block. Hence the correction on the x_{clust} is required, and given as:

$$x_{cor} = x_{clust}\left(1 - \frac{a}{\sqrt{L^2 + x_{clust}^2}}\right) \tag{4.10}$$

where L is the distance from the vertex to the calorimeter, a is the depth from the surface of the calorimeter to the point where the shower starts. The value of a is estimated to be 7 cm using Monte-Carlo simulation and elastic data [81]. Finally, the cluster/photon arrival time is computed as:

$$t_{cluster} = \frac{\sum_i A_i t_i}{\sum_i A_i} \tag{4.11}$$

where A_i and t_i are amplitude and arrival time of the signal in block i.

4.4 Monte-Carlo Simulation

The Monte-Carlo simulation is used to estimate the phase space or acceptance of the spectrometer and calorimeter in coincidence. For every event, the simulation gives access to both the vertex and the reconstructed variable simultaneously. This information is very advantageous for the extended target. But in data, only reconstructed variables can be accessed. The particle has to travel through the material medium to reach the detectors. On the way to detectors, a particles may lose some of their energies due to interaction with material. As a consequence, for any event the reconstructed kinematics variables (energy and angle) may be different than that at a vertex. Besides the phase-space determination, the simulation is also used to extract the cross-section at vertex via a fitting procedure that will be described in the next chapter.

The simulation is based on the CERN software package, GEANT4, written in C++ [97]. The DVCS setting in the GEANT4 was implemented by R. Paremuzyan and M. Defurne [98], and later the setup was adapted to the experiment E12-06-114 by M. Dlamini [76]. The GEANT4 package can handle the interaction of particles with the detector material, for instance, energy loss by electron while passing through different materials from vertex to entrance of the spectrometer, etc. Figure 4.7 shows an exact implementation of the experimental setting in the Monte-Carlo simulation. The scattering chamber, different beam shields, the spectrometer entrance window, the material between the vertex and spectrometer entrance window, and beam pipes are introduced as in HRS. However, the transportation of particles from the HRS entrance window to the HRS detectors is not implemented in the simulation. All the particles reaching the spectrometer entrance window are assumed to be detected by the HRS. To deal with the spectrometer acceptance, we use the R-Function concept discussed in Chapter 3. The calorimeter geometry is also fully implemented in simulation. All the calorimeter blocks are placed according to the survey position, and the full block package (screws, Tyvek paper, Tedlar, etc.) is implemented.

4.4.1 Event generator

The event generator in the simulation generates the event of interest within the given kinematic setting. The exclusive electroproduction of π^0 ($ep \to e'p'\pi^0$) can be split into two parts. First the leptonic part, describes the emission of a virtual photon and includes all radiative losses as described in Chapter 3. The hadronic part ($\gamma^* p \to p'\pi^0$) is treated in the second step (see dashed rectangle in Figure 4.8). Events are generated in the

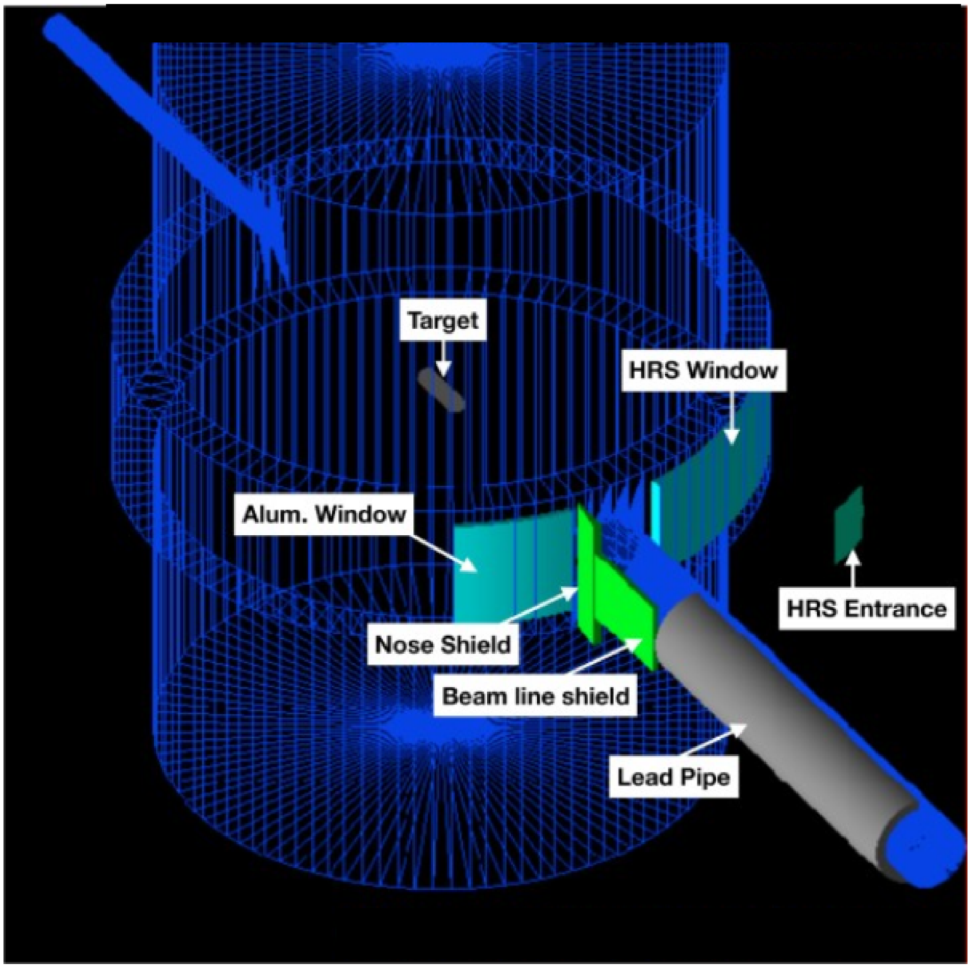

Figure 4.7: The experimental setup for the experiment the E12-06-114 implemented in GEANT4 Monte-Carlo simulation. The cylindrical mesh of the blue lines represents the scattering chamber maintained at very low pressure about 10^{-7} Torr where the target is placed. The beamline is represented in the dark blue. A lead pipe represents the shielding in the beam pipe, downstream to the target. The HRS entrance window and different beam shields are also implemented in the simulation.

larger acceptance window as compared to the actual spectrometer acceptance in order to accommodate for the radiative effects. For instance, the momentum acceptance range of the HRS is ± 4.5% of central value, but in the simulation events are generated within ±

6% of central value. In the same way though the horizontal acceptance is ± 28 mrad of the central value of the HRS angles, events are generated within ± 60 mrad of central value.

First, the vertex is generated then the external radiative loss is implemented. Taking the beam energy E_1 after the external radiative loss, the Q^2 is generated uniformly as:

$$Q^2 \in \left[4 \times E_1 \times p_{min} \times \sin^2\left(\frac{\theta_{min}}{2}\right), 4 \times E_1 \times p_{max} \times \sin^2\left(\frac{\theta_{max}}{2}\right)\right] \tag{4.12}$$

where max stands for maximum. To have physical π^0 event, the constraint on the invariant mass of the hadronic system is implemented i.e., $W^2 \geq M_p^2 + m_{\pi^0}$. It puts the constraint on the maximum value of Bjorken-x as:

$$x_B^{lim} = \frac{Q^2}{(M_p + m_{\pi^0})^2 - M_p^2 + Q^2} \tag{4.13}$$

where M_p and m_{π^0} are masses of proton and pion, respectively. Then x_B is generated within the limit defined by:

$$x_B^{min} = \text{Max}\left(\frac{Q^2}{2M_p(E_1 - P_{min})}, 0.05\right) \tag{4.14}$$

$$x_B^{max} = \text{Max}\left(\frac{Q^2}{2M_p(E_1 - P_{max})}, x_B^{lim}\right) \tag{4.15}$$

The GEANT4 toolkit handles all the radiative losses while transporting the electron up to the HRS entrance window. In the hadronic part, first the square of momentum transfer to the recoiling proton "t" (see the definition in Chapter 1) is uniformly generated between t_{min} and t_{max}. The value of t_{max} is fixed at -3 GeV^2 while t_{min} can be computed as:

$$t_{min} = -Q^2 - 2(A \times B) + 2(C \times D) + m_{\pi^0} \tag{4.16}$$

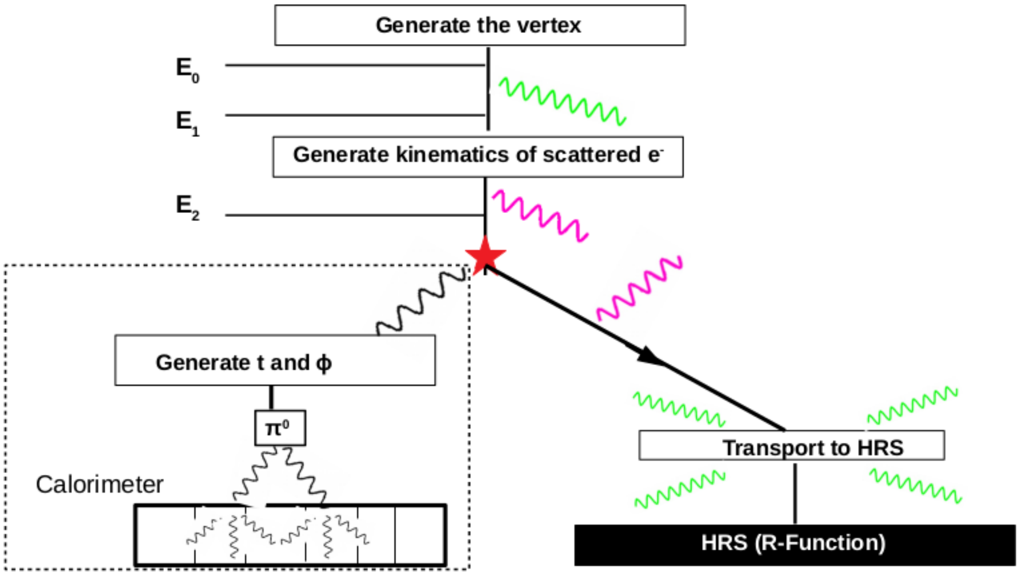

Figure 4.8: Schematic representation of event generation and the radiative corrections process in simulation. The radiative correction is on the leptonic part and follows the same procedure as described in chapter 3. The green and magenta photons are from external and internal radiative losses, respectively. The steps inside the dashed rectangular represent the hadronic part ($\gamma^* p \to \pi^0 p'$).

with

$$A = \frac{W^2 - M_p^2 + m_{\pi^0}^2}{2W} \tag{4.17}$$

$$B = \frac{W^2 - M_p^2 - Q^2}{2W} \tag{4.18}$$

$$C = B^2 + Q^2 \tag{4.19}$$

$$D = A^2 + m_{\pi^0}^2 \tag{4.20}$$

Once t is generated, the four-momentum vectors of final state particles are computed in the center of mass of the virtual photon-proton system. Later it is boosted to the laboratory frame and rotated around the virtual photon by and angle ϕ_{π^0} which is generated uniformly between the interval [0, 2π]. The photons from π^0 decay are isotropically generated in π^0 rest frame and later boosted to the laboratory frame. The phase space for each event can be computed as:

$$\Gamma_i = (\Delta Q^2)_i \times (\Delta x_B)_i \times (\Delta t)_i \times (\Delta\phi_{\pi^0})_i \times (\Delta\phi_e)_i \tag{4.21}$$

where the term ϕ_e is the angle made by the leptonic plane with the beam direction. The event is generated in a single plane, and to account for the azimuthal symmetry the factor 2π is introduced, i.e., $(\Delta\phi_e)_i = 2\pi$. Figure 4.8 illustrates the whole π^0 event generation process.

4.5 Calibration and Smearing of Simulation

The recoiled proton in the reaction e(p, e'π^0)p is selected by the missing mass squared distribution (see Equation 2.10). The Monte-Carlo simulation allows selection of most $ep \rightarrow e'p'\pi^0$ events while rejecting the events with additional particle production. In order to use the simulation for the estimation of exclusive cut, the missing mass squared distribution for both data and the simulation should have the same position and same resolution. However, due to the following reasons, the missing mass distribution from the simulation is different than data.

- In the simulation, the resolution of the PbF_2 blocks of the calorimeter do not degrade with the beam exposure time. But data are affected by the degradation of resolution of the calorimeter, so the width of missing mass distribution of data is larger as compared to simulation.

- Around 4% of photon energy leaks either between the blocks or at the back of the block. The energy leak is compensated in the data by adjusting the calibration coefficients but not in a simulation. As a consequence, the energy of a photon in simulation is underestimated, which shifts the missing mass peak towards larger value as compared to data.

To perform the calibration and smearing of the simulation, the momentum and energy of the photons are multiplied by a random variable following a Gaussian distribution, Gauss (μ, σ), as:

$$\begin{pmatrix} q_x \\ q_y \\ q_z \\ E \end{pmatrix} \rightarrow \text{Gauss}(\mu, \sigma) \times \begin{pmatrix} q_x \\ q_y \\ q_z \\ E \end{pmatrix} \tag{4.22}$$

The parameter μ shifts the mean of the energy distribution of the photons, and the energy resolution effect of calorimeter crystal is taken into account by the parameter σ. The method for the calibration and the smearing is adapted from the M. Defurne thesis [79].

The data for each kinematics are separated by time. With time, the response of calorimeter blocks degrades due to the radiation damage. To account for this fact, the simulation for each kinematics needs to be smeared. The resolution of calorimeter block differs with the position in the calorimeter. For instance, blocks close to the beamline degrade faster than the blocks farther away from the beamline. To have position dependent calibration coefficients, the entire calorimeter is divided into $7\times 7 = 49$ overlapping rectangular sections. The parameters μ and σ are computed for each of the sections independently such that the missing mass square distribution between the data and simulation have the best match in that particular section. Later for each event depending on its impact position on calorimeter, μ_i, σ_i are extracted by interpolating the previously extracted μ, σ values for different 49 sections. In addition to the missing mass cut, we also apply the π^0 invariant mass (see definition in Equation 2.11) cut to select the exclusive π^0 events. This requires the agreement between the simulation and data for invariant mass distribution. The invariant mass is mostly sensitive to the angle between two photons:

$$m^2_{\pi^0} = m^2_{\gamma_1\gamma_2} = 2E_1E_2\left(1 - \cos\theta_{\gamma_1\gamma_2}\right) \tag{4.23}$$

where $\theta_{\gamma_1\gamma_2}$ is the angle between two decayed photons from π^0. To have the same invariant mass distribution both on data and simulation, keeping the μ and σ constant (determined from missing mass smearing), the angular resolution is smeared isotropically with an angle, θ, generated following a Gaussian distribution.

Figure 4.9 shows the variation of calorimeter calibration coefficient (μ) and resolution parameter (σ) within the surface of the calorimeter for the kinematic 60-3. The coefficient μ varies by about 4% across the calorimeter blocks. While the energy resolution parameter varies between 0.14 GeV to 0.21 GeV for photon of energy 5 GeV. For the smearing of invariant mass distribution, the angular resolution (in degrees) across the calorimeter surface is shown in Figure 4.10. The angular resolution varies between 0.04 to 0.1 degrees within the calorimeter. The observed small variation in μ, σ, and θ across the calorimeter position is expected due to the energy and the angular resolution of the calorimeter and the position dependent effect of radiation damage. In other words, the blocks close to the beamline are more susceptible to radiation damage, so they have poorer resolution.

Figure 4.11 shows the effect on missing mass squared and invariant mass distribution before and after smearing the simulation. Before smearing the simulation (black histogram), the mean position is different than that of data (red histogram). This is due to energy leakage, as described previously. Along with the mean position, the widths for both the distributions are different in simulation and data before smearing. After smearing (blue histogram), the simulation and data have a similar distribution.

In this chapter, I have briefly explained how to extract the energy and position information of the photons from the raw calorimeter signal. I also explained the steps involved in the Monte-Carlo simulation and briefly described the necessity and procedure for smearing the simulation. After smearing the same peak position and shape of the same missing mass squared and invariant mass distribution was obtained between the simulation and data.

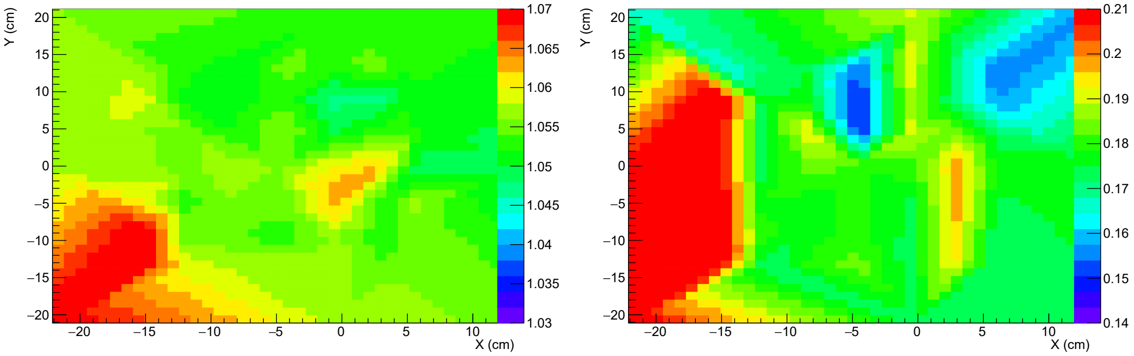

Figure 4.9: The extracted parameters μ and σ in GeV for different sections of the calorimeter for kinematic 60-3. Left: The values of the calibration coefficient for the blocks in a different position to have the same peak position for the missing mass and invariant mass distribution. Right: The values of σ to change the width of missing mass squared distribution.

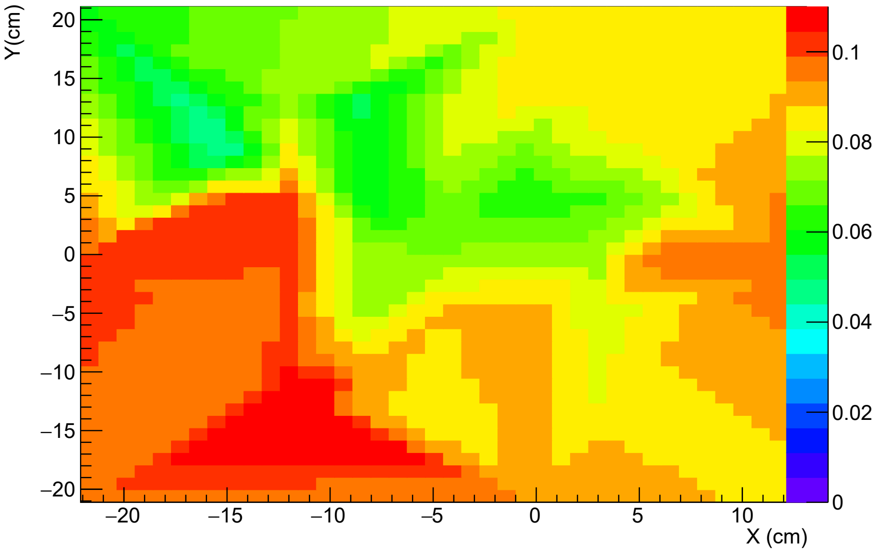

Figure 4.10: The angular resolution in degrees used to smear the invariant mass distribution for kinematic 60-3. As expected blocks close to the beamline have (towards negative x) poor resolution relative to the blocks away from the beamline.

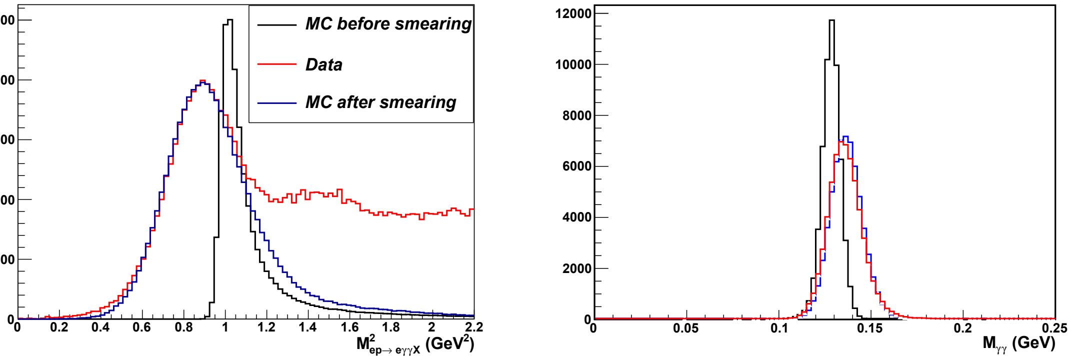

Figure 4.11: Smearing effects on the missing mass squared and invariant mass distribution from simulation. Left: The missing mass squared distribution. Right: Invariant mass distribution. The black histogram represents the simulation before smearing, the blue histogram represents simulation after smearing, and the red histogram is for the data for comparison. After smearing, data and simulation have the same mean position and the resolution.

5 EXCLUSIVE π^0 PRODUCTION AND CROSS-SECTION RESULTS

The main goal of my dissertation is to extract the cross-section for the exclusive π^0 production ($ep \rightarrow e'p'\pi^0$). To measure the cross-section for exclusive processes all the final state particles (recoiled proton, scattered electron, and pion) are identified. The procedure for selecting the scattered electron is same as the one described in Chapter 3. The recoiled proton is reconstructed using the missing mass square distribution (see Equation 2.10). In the first part of this chapter, I will focus on the selection criteria for π^0. In the second part, I will describe the cross-section extraction formalism and finally present my results and conclusions. I analyzed the kinematics with two different values of Q^2 equal to 5.54 GeV^2 and 8.40 GeV^2 at fixed Bjorken-x (x_B=0.60).

5.1 Accidental Subtraction

Exclusive π^0 electroproduction is a three-body final state, but only the scattered electron and π^0 are detected. Neutral pions decay before they arrive at our detector. So the π^0 events are reconstructed from decayed photons information. As discussed earlier, for the overall exclusivity of the reaction, we select the recoil proton from the missing mass squared distribution. One of our main sources of background is accidental events. Two photons detected in the calorimeter in coincidence with an electron in the spectrometer may not always come from the same reaction. To exclude the accidental events from our analysis, we perform a side band random time coincidence estimation. Figure 5.1 shows the arrival time of each of the two photons with respect to the electron. The rectangular section R_5 represents two photons γ_1 and γ_2, arriving within ±3 ns (coincidence window) relative to an electron in the spectrometer. However, these events may still be contaminated with accidental events. The number of events in section R_5 can be

$$R_5 = N_{ccc} + N_{acc} + N_{cca} + N_{cac} + N_{aaa} \tag{5.1}$$

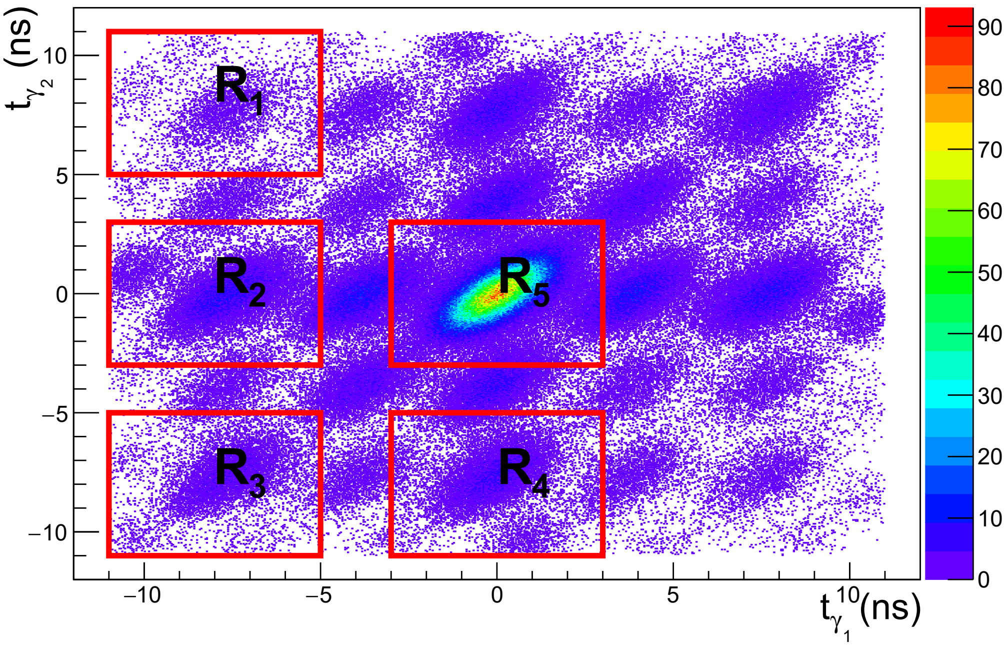

Figure 5.1: Arrival time of each of the two photons in the calorimeter with respect to the electron in the spectrometer. The start time 0 corresponds to the detection of an electron in the spectrometer. The diagonally aligned events represent two photons in coincidence.

where the N is the number of events. The subscript "a" and "c" represent accidental and coincidence, respectively. The three subscripts are listed in order for the electron, first photon (γ_1), and the second photon (γ_2) to describe if they are accidental or true coincidence. For instance, N_{acc} means the number of events with two photons in coincidence with each other but in random coincidence with the electron.

In the same way, the other sections of Figure 5.1 can be defined as:

$$R_1 = N_{aaa} \tag{5.2}$$

$$R_2 = N_{cca} + N_{aaa} \tag{5.3}$$

$$R_3 = N_{acc} + N_{aaa} \tag{5.4}$$

$$R_4 = N_{cac} + N_{aaa} \tag{5.5}$$

The total number of accidental event is given by:

$$N^{ACC} = N_{acc} + N_{cca} + N_{cac} + N_{aaa} \tag{5.6}$$

The accidental rates are uniform with time; based on this fact, we can estimate the number of accidental events by performing the clustering (as described in section 4.3) in several time windows. Table 5.1 shows the different clustering windows, sensitiveness of each window to a different kind of accidentals (N_{cca}, N_{cac}, etc.), and corresponding visual representation in Figure 5.1.

Table 5.1: Different calorimeter clustering time windows to estimate the accidental events. The different clustering time windows are sensitive to different types of accidental and can be visually represented in the arrival time distribution of photons by different sections.

Clustering window	Accidental	Section	Description
[-3, 3]	$N_{ccc} + N^{ACC}$	R_5	$\|t_{\gamma_1}\| <= 3$ and $\|t_{\gamma_2}\| <=3$
[-11, -5]	$N_{acc} + N_{aaa}$	R_3	$\|t_{\gamma_1} + 8\| <= 3$ and $\|t_{\gamma_2} + 8\| <=3$
[-11, -5] and [-3, 3]	$N_{cca} + N_{cac} + N_{aaa}$	R_4	$\|t_{\gamma_1} + 8\| <= 3$ and $\|t_{\gamma_2}\| <=3$
[-3, 3] and [-11, -5]	$N_{cca} + N_{cac} + N_{aaa}$	R_2	$\|t_{\gamma_1}\| <= 3$ and $\|t_{\gamma_2} + 8\| <=3$
[5, 11] and [-11, -5]	N_{aaa}	R_1	$\|t_{\gamma_1} - 8\| <= 3$ and $\|t_{\gamma_2} + 8\| <=3$

The suitable combination of these clustering windows as given by Equation 5.7 can reproduce the same total number of accidentals that are required to be eliminated from main coincidence window, [-3, 3].

$$N^{ACC} = R_3 + \left(\frac{R_2 + R_4}{2}\right) - R_1 \tag{5.7}$$

5.2 π^0 Selection

The lifetime of π^0 is very short (about 10^{-17}s), so it decays into two photons (about 99% of cases) before reaching the calorimeter. π^0 events are reconstructed from the energy and momentum information of the decayed photons detected in the calorimeter. The two photons produce two clusters in coincidence in the calorimeter. However, two clusters in the calorimeter may not always represent a π^0 event. In some cases, either one or both the clusters may be from low energy photons (background). In order to remove the low energy photons from the signal, we apply an minimum energy threshold cut (see Table 5.4 for value). The choice of energy threshold cut introduces systematic in the π^0 analysis and will be discussed in a later section.

After we identify the two photons in the calorimeter, along with an electron in the spectrometer, we apply the pion invariant mass and p(e,e'π^0)X missing mass cuts to select the exclusive events from the channel our interest ($ep \to e'p'\gamma_1\gamma_2$). The π^0 invariant mass distribution and missing mass distributions are correlated because any imperfection in measuring the energies of photons will effect both of the distributions. Because of this correlation, we can not apply a simple geometrical exclusivity cut. To remove this correlation, an empirical approach suggested by M. Malek [99] is adopted. The corrected missing mass squared distribution is given as:

$$M_X^2 = M_X^2|_{raw} + Corr \cdot \left(m_{\gamma_1\gamma_2} - m_{\pi^0}\right) \tag{5.8}$$

where $M_X^2|_{raw}$ and M_X^2 are the missing mass square before and after removal of the correlation, respectively. $m_{\gamma_1\gamma_2}$ is the measured invariant mass in the experiment while

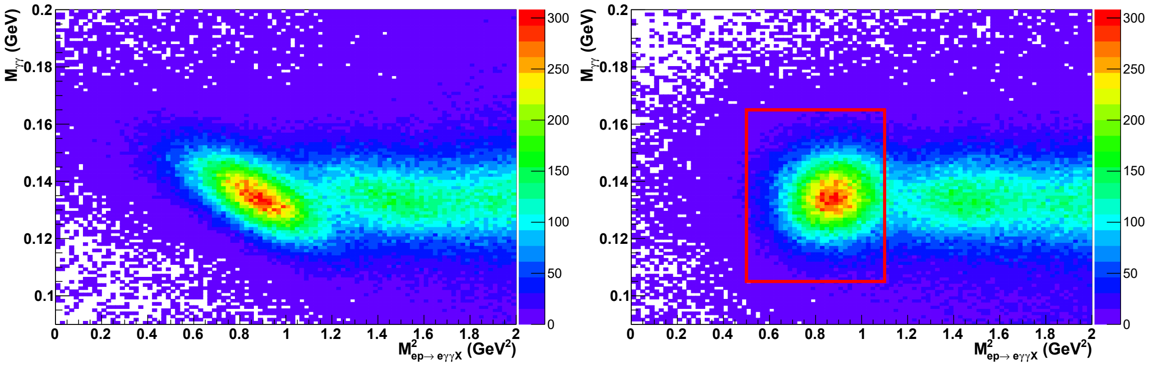

Figure 5.2: The invariant mass vs. the missing mass squared distribution before and after the correction for the kinematic 60-1. Left: Before correcting the correlation effect. Right: After the removal of correlation.

m_{π^0} is ideal the invariant mass for π^0, and its value is set at 0.13497 GeV from Particle Data Group [75]. The correction is applied on an event by event basis. The correction factor (Corr) is defined as:

$$Corr = \frac{2}{m_{\pi^0}}\left(m_{\pi^0}^2 - 2\sqrt{2}\left(\nu + M_p - q\cos\theta_{\pi\gamma^*}\right)\frac{E_1E_2}{E_1+E_2}\right) \tag{5.9}$$

where ν is the energy of a virtual photon, $\theta_{\pi\gamma^*}$ is the angle between virtual photon and π^0, and q is the magnitude of 3-momentum of the virtual photon. E_1, E_2 are the energies of photons decayed from the π^0. Though the correction factor (Corr) was evaluated for each event, the mean value was used in Equation 5.8 for the correction. The correction factor is determined for each kinematics independently. The correction factors for kinematic 60-1 and 60-3 were -13.7 GeV and -17.64 GeV, respectively. Figure 5.2 shows the effect of that correction. The red rectangular box in Figure 5.2 (right) shows the simple geometric cut used to select the exclusive events. The choices of exclusive cuts were based on the comparison of the missing mass squared distributions between data and simulation. For instance, Figure 5.3 illustrates that the choice of the exclusivity cuts by comparing simulation and data. The

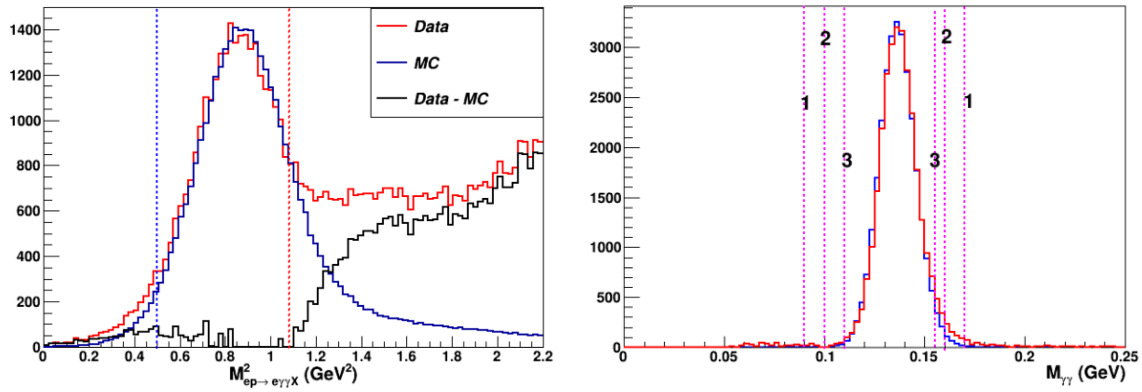

Figure 5.3: Left: Comparison of the missing mass squared distribution between data (red) and simulation (blue). Random coincidences are removed before applying exclusivity cuts. The black histogram shows the difference between simulation and data. The blue line and red line represent the lower and upper bound between which simulation can well describe the data. Right: The invariant mass distribution for data (red) and simulation (blue). The magenta lines on either side of the peak represent the upper and lower bounds for the invariant mass cuts. These three sets of invariant mass extrema were used for the systematic study.

extrema of the exclusive cuts for kinematics 60-1 and 60-3 are given in Table 5.2. The systematic effect on the extracted cross-section due to the different choice of exclusive cuts is studied and will be explained later.

A photon striking at the edge of the calorimeter may not lose all of its energy in the calorimeter; as a consequence, the reconstructed energy-momentum information is not precise. In order to avoid photons incident on the edge of the calorimeter, a calorimeter acceptance cut is implemented. The calorimeter acceptance cut is a rectangular cut, which eliminates events striking on the most external layer of the calorimeter (one block deep).

Table 5.2: Position of the exclusivity cuts selecting exclusive π^0 events.

Kinematic	M_x^2 (GeV^2)	$M_{\gamma_1\gamma_2}$ (GeV)
60-1	[0.3, 1.08]	[0.10, 0.16]
60-3	[0.5, 1.08]	[0.10, 0.16]

5.3 Correction for Branching Ratio of $\pi^0 \rightarrow \gamma\gamma$

A π^0 decays into two photons ($\pi^0 \rightarrow \gamma\gamma$) with a branching ratio 98.82% [75]. The number of detected pion are corrected by branching ratio as:

$$N_{corrected} = \frac{N_{raw}}{BR} \tag{5.10}$$

where BR is the branching ratio. N_{raw} and $N_{corrected}$ are the number of detected π^0 events.

5.4 Correction from 3 Clusters

As discussed in Section 4.3 to select exclusive π^0, only the events with two clusters in the calorimeter are selected. But sometimes there can be 3 clusters in the calorimeter, two clusters from decayed photons from π^0 and one accidental photon. Due to our selection criteria we can miss the possible exclusive π^0 event if there are 3 clusters in the calorimeter. The correction from 3 clusters is implemented in our final number of events selected as:

$$N_{corr} = N \times 3ClusCorr \tag{5.11}$$

where N and N_{corr} are the total number of exclusive π^0 events before and after implying the correction from 3 clusters. The correction from 3 clusters (3ClusCorr) is given by,

$$3ClusCorr = \frac{N_{3Clus}}{N_{2Clus}} \tag{5.12}$$

where N_{2Clus} is the total number of exclusive π^0 events with the total number of clusters equal to 2 during clustering (see Section 4.3). N_{3Clus} is the total number of exclusive π^0

events with 3 clusters in the calorimeter. Out of those 3 photons (γ_1, γ_2, and γ_3) all the possible π^0 events are reconstructed (γ_{12}, γ_{13}, γ_{23}). The accidental events for 3 clusters are subtracted in the same way as 2 clusters analysis (see Section 5.1). Table 5.3 shows the correction from 3 clusters.

Table 5.3: The correction factors from 3 clusters. The cases where two or more combinations of photons forming the π^0 are neglected. The precision of the correction factor is our inability to identify the exclusive π^0 event while multiple combinations of photons are possible.

Kinematic	Correction (%)
60-1	3.9 ± 0.1
60-3	3.6 ± 0.1

5.5 Cross-Section Extraction Formalism

The π^0 electroproduction cross-section is parametrized by Equation 1.28. The experimental cross-section is extracted by minimizing the difference between the number of events in the data and the number of events predicted by simulation in each kinematic bin. This procedure has two main advantages:

- It can take care of bin migration from the vertex kinematic to measured kinematic, caused by resolution and radiative effects.
- It integrates the kinematics dependencies of the cross-section over the entire experimental acceptance range.

Based on the reconstructed variables, the π^0 events are binned in 5 different $t_{min} - t$ bins (see Equation 4.16) and 12 ϕ bins (see Figure 1.10 for ϕ definition). These bins are called reconstructed bins. The Monte-Carlo simulation contains both the vertex and reconstructed variables information. So these events are binned in both reconstructed and vertex bins. If there would be no radiative and resolution effects, then the same number of events would be in both the reconstructed and vertex bins. The number of event reconstructed in a bin r is the sum of events generated in any of the vertex bins, weighted by the probability (K_{rv}) of the vertex events to migrate in that reconstructed bin that is,

$$N_r = \sum_{v=1}^{\mathcal{V}} K_{rv} N_v \tag{5.13}$$

where N_r is the total number of events in a specific reconstructed bin r and N_v is the total number of events in a specific vertex bin v. $\mathcal{V}$ is the number of vertex bins. Now the cross-section is related to the number of events at the vertex as:

$$N_v = \mathcal{L} \int_{\phi_v} \frac{d^4\sigma_v}{d\Phi} d\Phi \tag{5.14}$$

where dΦ=dQ^2 dx_B dt dϕ_π is a four-fold phase space factor. Now using Equation 5.14, Equation 5.13 can be re-written as:

$$N_r = \mathcal{L} \sum_{v=1}^{\mathcal{V}} K_{rv} \int_{\phi_v^r} \frac{d^4\sigma_v}{d\Phi} d\Phi \tag{5.15}$$

where ϕ_v^r corresponds to the sub-volume of vertex phase space contributing to N_r. Assuming the cross-section to be stable in the phase space ϕ_v^r, Equation 5.15 can be re-written as:

$$N_r = \sum_{v=1}^{\mathcal{V}} K_{rv} \left(\mathcal{L} \int_{\phi_v^r} d\Phi \right) \frac{d^4\sigma_v}{d\Phi} \tag{5.16}$$

Now the integration of the Equation 5.16 yields:

$$K_{rv} = \sum_{i \epsilon r \cap v} \frac{\Gamma_{MC}^i}{N_{gen}}, \tag{5.17}$$

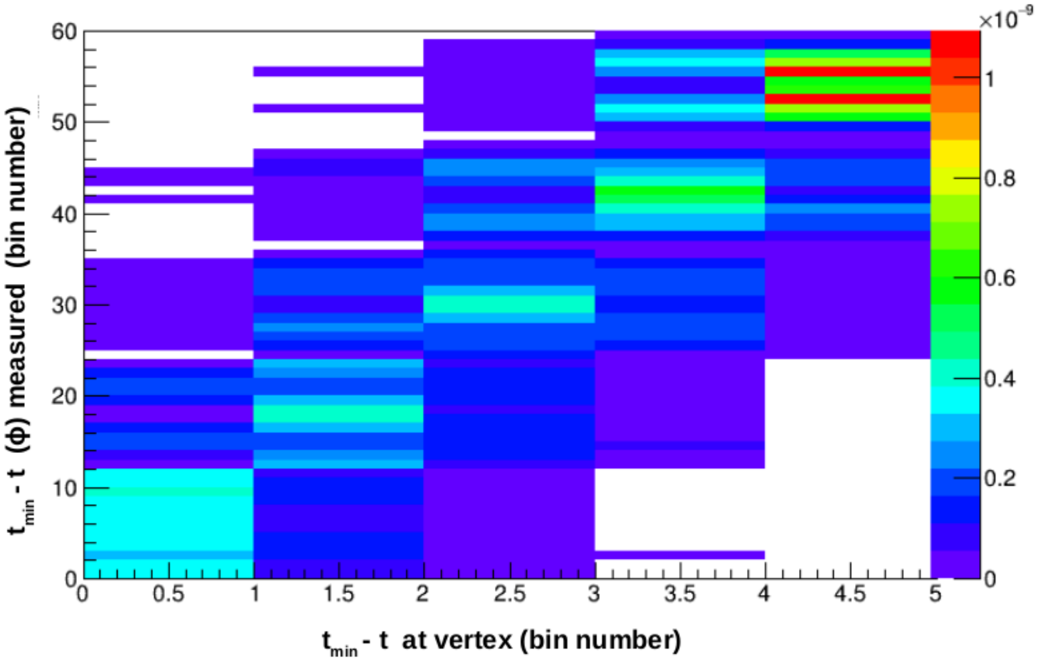

Figure 5.4: The bin migration probability matrix with kinematic dependence terms for unseparated cross-section term for kinematic 60-1. The horizontal axis represents the five $t_{min} - t$ (t') bins measured at the interaction point (vertex). The Y-axis represents five reconstructed t' bins. Each t' bin is divided into 12 ϕ bins. The diagonal boxes represent the events where both the vertex and reconstructed kinematics fall in the same t' bin. The off-diagonal boxes represent the cases with bin migration.

where i is an event in reconstructed bin r and vertex bin v, N_{gen} is the number of generated events in simulation, Γ^i_{MC} is the phase space factor for an event i. Using the simulation, the bin migration probability can be computed. Figure 5.4 shows the bin migration probability matrix for unseparated cross-section term along with kinematic dependence term. Depending on kinematic and bin, the bin migration is up to 10% [100].

5.5.1 Fitting procedure

Let X^n be the different cross-section parameters then the cross-section for π^0 production can be re-written from Equation 1.28 as:

$$\frac{d^4\sigma}{dQ^2 dx_B dt d\phi_\pi} = \sum_{n=1}^{N} \Gamma_n(E, Q^2, x_B, t, \phi) X^n, \tag{5.18}$$

where Γ_n(E, Q^2, x_B, t, ϕ) is a known function, which depends only on kinematic variables (see Equation 1.28). N represents the total number of cross-section parameters. For unpolarized cross-section there are total 3 parameters to be extracted: $\sigma_{\mathrm{T}} + \epsilon\sigma_{\mathrm{L}}$, σ_{TT}), and σ_{TL}. The helicity dependent or polarized cross-section term $\sigma_{\mathrm{TL'}}$ in the total cross-section (see Equation 1.28) is extracted by measuring the difference of cross-sections with opposite beam helicity, as:

$$\frac{1}{2}\left(d\overrightarrow{\sigma} - d\overleftarrow{\sigma}\right) = d\sigma_{TL'} \tag{5.19}$$

Using Equation 5.18 in Equation 5.15 the number of events in a reconstructed bin can be connected with cross-section parameters as:

$$N_r = \sum_{v=1}^{V} \sum_{n=1}^{N} K^n_{rv} X^n_v \tag{5.20}$$

Now with the assumption that these cross-section parameters do not vary within a experimental bin, the bin migration probability can be defined as follows:

$$K^n_{rv} = \sum_{i\epsilon r\cap v} \Gamma_n(E, Q^2, x_B, \phi) \frac{\Gamma^i_{MC}}{N_{gen}}, \tag{5.21}$$

To extract the cross-section parameters the total number of events in data and Monte-Carlo is minimized as:

$$\chi^2 = \sum_{r=1}^{\mathcal{R}} \left(\frac{N^{exp}_r - N^{MC}_r}{\sigma^{exp}_r} \right)^2 \tag{5.22}$$

where $\mathcal{R}$ is the total number of ϕ bins, σ^{exp}_r is the error associated with the experimental bin r. The number of events generated in Monte-Carlo is about an order of magnitude larger than in data so the error associated with Monte-Carlo is neglected. N_r^{MC} and N_r^{exp} are the number of events in the reconstructed bin r in Monte-Carlo and data, respectively. Equation 5.20 connects N_r^{MC} to the cross-section parameters. For the case of polarized cross-section extraction, the N_r^{exp} is given by

$$N_r^{exp} = N^+ - N^- \tag{5.23}$$

where N^+ is the number of events with positive helicity state and N^- is the number of events with negative helicity state.

Let $\overline{X}^n$ be the values of X^n which minimize the χ^2 in Equation 5.22 i.e,

$$0 = -\frac{1}{2}\frac{\partial \chi^2}{\partial X^n}\bigg|_{\overline{X}^n} \tag{5.24}$$

$$0 = \sum_{v'=1}^{V}\sum_{n'=1}^{N} A_{v,v'}^{n,n'}\overline{X}_{v'}^{n'} - B_v^n \qquad \forall v, n \tag{5.25}$$

Equation 5.25 is the matrix equation in the form, AX=B. The matrix A has a dimension $(N \times \mathcal{V}) \times (N \times \mathcal{V})$ and the matrix B with $(N \times \mathcal{V}) \times 1$. The matrix elements for A and B can be defined as:

$$\begin{aligned} A_{v,v'}^{n,n'} &= \sum_{r=1}^{R} \mathcal{L}^2 \frac{K_{rv}^{n} \times K_{rv'}^{n'}}{(\sigma_r^{exp})^2} \\ B_v^n &= \sum_{r=1}^{R} \mathcal{L} \frac{K_{rv}^{n} \times N_r^{exp}}{(\sigma_r^{exp})^2} \end{aligned} \tag{5.26}$$

where the term $\mathcal{L}$ is the integrated luminosity given by Equation 3.2. The linear system of equations represented by Equation 5.25 is solved to extract the cross-section parameters ($\overline{X}^n$), by inverting the matrix A:

$$\overline{X}^n = \sum_{v'=1}^{V}\sum_{n'=1}^{N} [A^{-1}]_{v,v'}^{n,n'} \cdot B_{v'}^{n'} \tag{5.27}$$

where A^{-1} is the inverse matrix. The cross-section parameters that give the minimum value of χ^2 in Equation 5.22 are extracted. The error on each cross-section parameter (σ_n^2) is

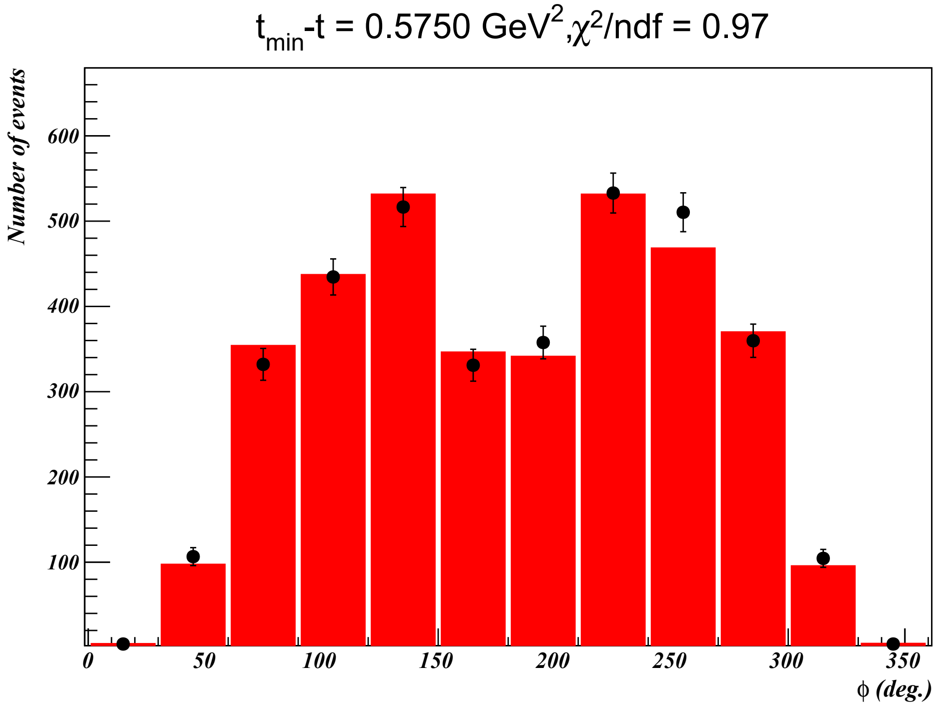

Figure 5.5: The number of events in the typical experimental bin of kinematic 60-3. The black points are data with statistical error bar and the red bars represent the Monte-Carlo prediction. The cross-section parameters that minimize the difference between the number of events in data and Monte-Carlo are extracted.

given by

$$\sigma_n^2 = [A^{-1}]_{nn} \tag{5.28}$$

In order to check the extraction procedure, one can reconstruct the the number of simulation counts in each t_{min} -t bin by computing,

$$N^{MC} = \mathcal{L} \sum_{v,n} K_{rv}^{n} \dot{X}_{v}^{n} \tag{5.29}$$

Figure 5.5 illustrates the best agreement between the prediction by the simulation and the data for a specific bin. Appendix B shows a similar comparison for all the bins in both kinematics 60-1 and 60-3.

5.6 Systematic Errors

Our choices of the cuts to select the exclusive π^0 events introduces a systematic error in the cross-section analysis. I studied the different sources of systematic errors for both kinematics 60-1 and 60-3. While studying the DIS cross-section, a 3.5% of systemic uncertainty from electron selection was found. The sources of the 3.5% uncertainty in inclusive electron measurements were from: radiative correction, spectrometer acceptance, luminosity, electron identification, and spectrometer multi-track corrections. This error needs to be taken in to account in π^0 cross-section analysis. This 3.5% systematic associated with inclusive electron measurement (DIS) will be taken as the global effect, that is, the same effect will be considered for all kinematical points. Along with the error associated with an electron selection and luminosity, there is also an error associated with the photon selection. For instance the choice of exclusivity cut, photon energy cut, and clustering threshold cut to select the good π^0 candidates might have a systematic effect on the extracted cross-sections.

5.6.1 Exclusivity cuts

To evaluate the systematic effect of exclusivity cuts, the fluctuation of the cross-section parameters with different cut positions is studied. In this section, the procedure adapted for this analysis is described.

- Missing mass cut higher extremum:

  The extrema of the invariant mass distribution is fixed at “2” (see Figure 5.3). In addition, the lower end of the missing mass squared distribution is also fixed as shown by the blue line in Figure 5.3 (left). Then the cross-section parameters are extracted at the different higher extrema of the missing mass squared cut, below the threshold (the extremum up to where the simulation and data are in agreement). The red points in Figure 5.6 denote the unseparated cross-section parameter at different values of higher extremum of missing mass squared cut for kinematics 60-1 (top) and 60-3 (bottom).

- Missing mass cut lower extremum:

  The upper bound of missing mass squared distribution and invariant mass cuts are fixed. Then the cross-section is extracted at different values of lower extrema of missing mass squared cut. The extracted unseparated cross-section parameter is shown with blue points in Figure 5.6 for kinematics 60-1 (top) and 60-3 (bottom).

- Invariant mass cuts:

  The extrema of missing mass squared cut is fixed. Then the cross-section terms are extracted at different invariant mass cut positions “1”, “2”, and “3” (see Figure 5.3). The extracted unseparated cross-section parameter is shown with magenta points in Figure 5.6 for kinematics 60-1 (top) and 60-3 (bottom).

The unseparated cross-section parameter $\sigma_{\mathrm{T}} + \epsilon\sigma_{\mathrm{L}}$ is stable within 0.5% for different choices of the exclusivity cuts for both kinematics 60-1 and 60-3 (see Figure 5.6). The other cross-section terms like σ_{TL}, σ_{TT}, and $\sigma_{\mathrm{TL'}}$ are insensitive to the choices of different exclusivity cuts presented here due to the large statistical error.

5.6.2 Energy threshold

In order to eliminate the low energy photon background, only the reconstructed photons above certain threshold are selected. Our choice of minimum energy cut is the other source of systematic error. Figure 5.7 shows the variation in the cross-section parameter $\sigma_{\mathrm{T}} + \epsilon\sigma_{\mathrm{L}}$ in one of the t_{min}-t bin, with different choices of photon energy cut for kinematic 60-1 (top) and 60-3 (bottom). For kinematic 60-3, the cross-section is independent of the choice of energy cut. For kinematic 60-1, the small t_{min}-t bins show a variation up to 4% with the different choices of photon energy cuts. The other cross-

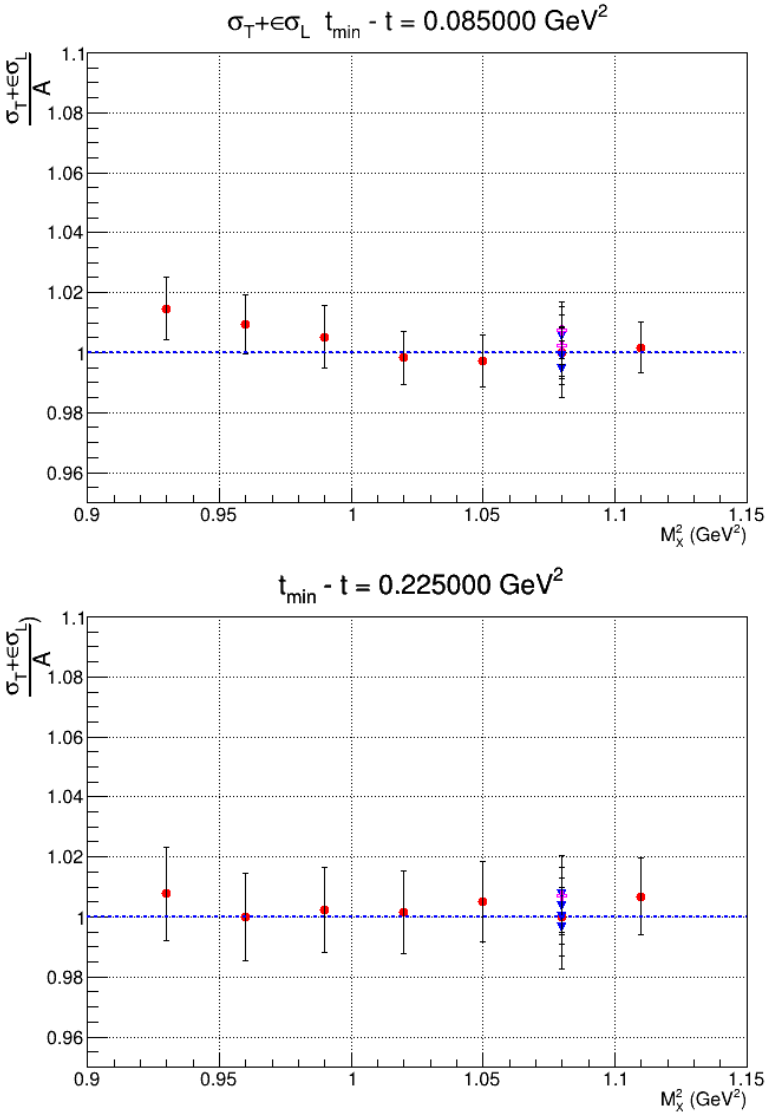

Figure 5.6: The cross-section parameter $\sigma_T + \epsilon\sigma_L$ normalized to a value at 1.08 GeV^2 (A) at different exclusivity cuts for kinematic 60-1 (top) and 60-3 (bottom). The red points represent the different higher extrema of missing mass squared cuts, keeping the other fixed. The magenta points represent the variation with the different invariant mass cut. The blue points represent the variation of cross-section term with the lower end of missing mass squared cut, keeping other cuts fixed.

section parameters are insensitive to the energy cut due to larger statistical error associated with these parameters.

5.6.3 Clustering threshold

When a photon hits on the calorimeter it deposits its energy in multiple blocks. The blocks producing a signal from the photon form a cluster. In order to discriminate the noise from a real signal, we require the cluster to be above a certain energy threshold. This energy threshold implemented during the clustering process is called the clustering threshold. The values of the software cut on photon's energies, clustering thresholds, and expected π^0 energies are shown in Table 5.4 for the kinematics I analyzed.

Table 5.4: Clustering and software thresholds with expected π^0 energies for the kinematics 60-1 and 60-3. Both the photons are required to have the energy greater than the threshold to qualify as good π^0 events.

Kinematic	Clustering Threshold (GeV)	Expected π^0 energy (GeV)	Software threshold (GeV)
60-1	0.8	4.92	1.1
60-3	1.0	7.46	1.1

To quantify the systematic due to the clustering threshold, the variation in the extracted cross-section with different clustering thresholds is studied. The unseparated cross-section term for kinematic 60-3 is fairly independent on clustering thresholds (see bottom Figure 5.8). But for kinematic 60-1, especially at small t_{min}-t bin the choices of threshold cut introduces the systematic up to 4% (see top Figure 5.8). The other cross-section terms are insensitive to the different choices of the clustering threshold due to the large statistical error associated with them. The total systematic errors are given in Table 5.5. The error due to photon energy or clustering threshold cut are different for each t_{min}-t bin. They are not reported in Table 5.5 but considered in the final cross-section results.

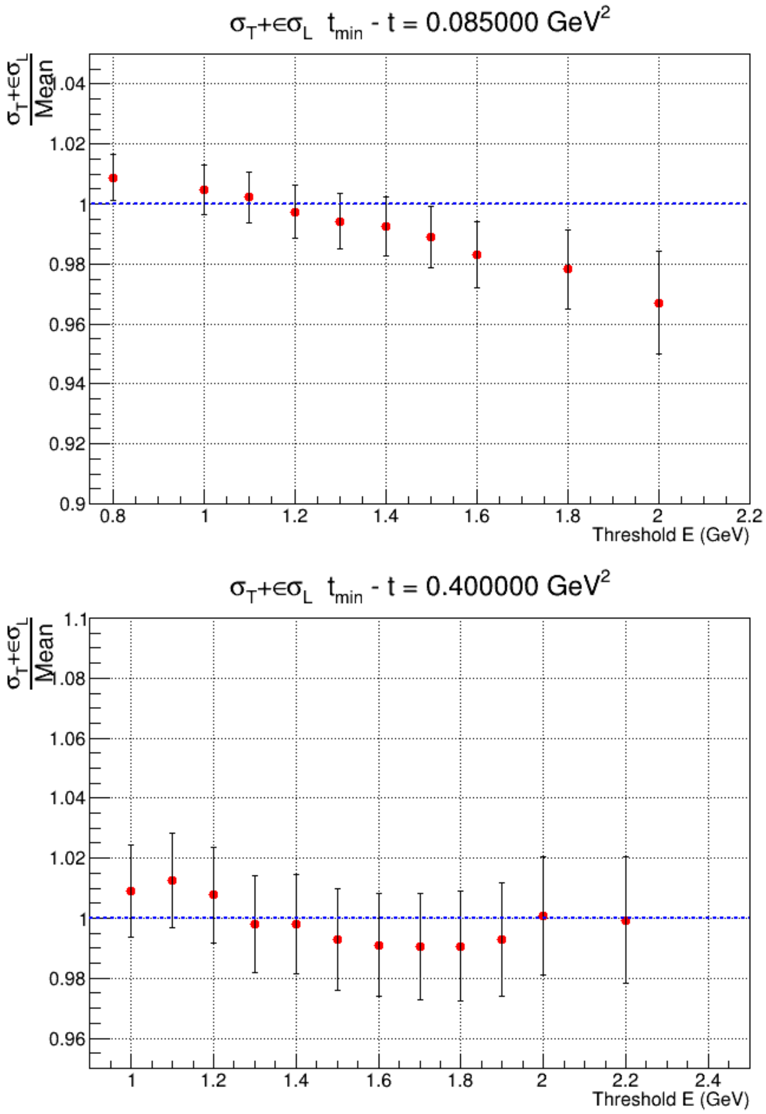

Figure 5.7: The variation in the cross-section parameter $\sigma_T + \epsilon\sigma_L$ with different choices of the energy cut imposed in selection of photons from π^0 decay for kinematic 601 (top) and 60-3 (bottom). The y-axis represents the unseparated cross-section parameter relative to a mean value. The extracted cross-section should be constant regardless our choice of energy threshold. But for kinematic 60-1, the choice of energy threshold introduces systematic up to 4% depending on bin.

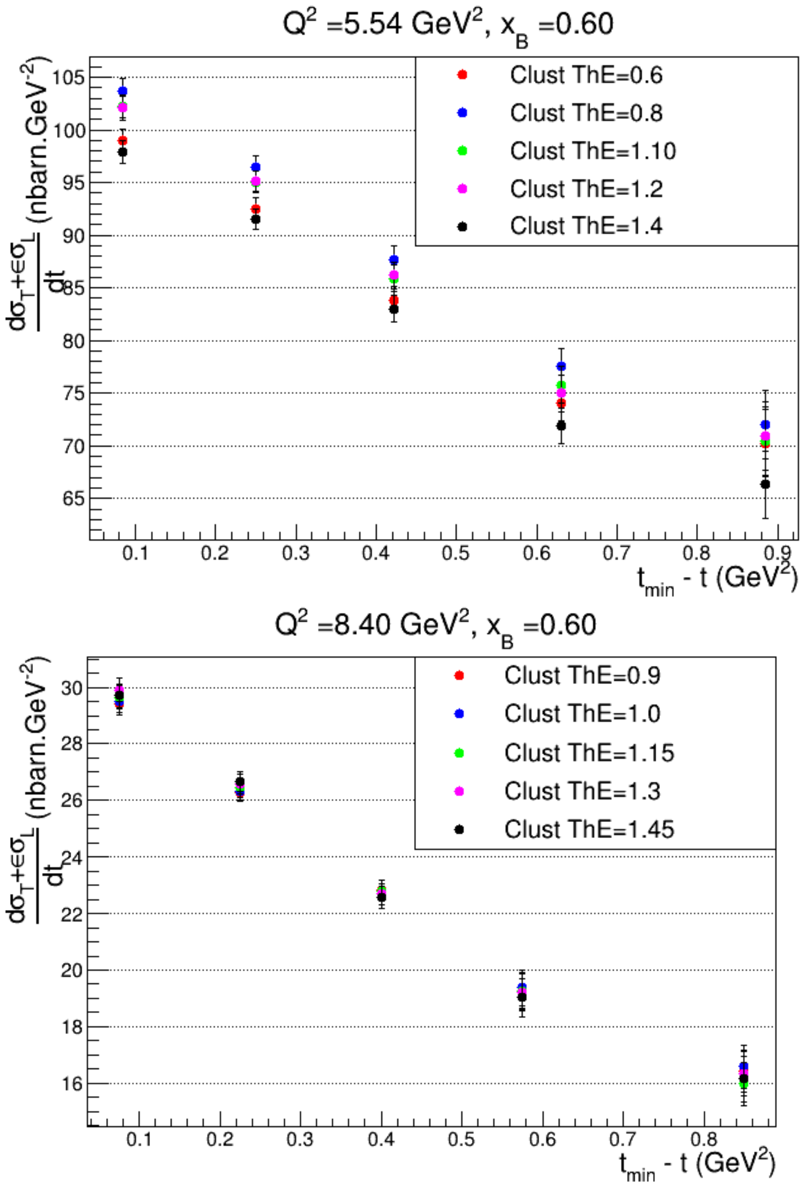

Figure 5.8: The variation in the cross-section parameter $\sigma_T + \epsilon\sigma_L$ with different choices of the clustering threshold cut, while selecting the photons cluster from π^0 decay for kinematic 60-1 (top) and 60-3 (bottom). The result is only shown for one of the t_{min}-t bins in each kinematics, but all other bins show a similar trend.

Table 5.5: Systematic errors for exclusive π^0 cross-section. The DIS study error includes the systematic from radiative correction, electron identification, and spectrometer acceptance.

Systematic	Value (%)
Exclusivity Cuts	0.5
DIS study	3.5
Clustering threshold	0.5
Photon Energy cut	0.5
Total Quadratic (helicity-independent)	3.6
Beam polarization	1
Total Quadratic (helicity-dependent)	3.75

5.7 Result and Discussion

Having taken data with only one beam energy for each x_B and Q^2, we can not separate the cross-section terms σ_{T} and σ_{L}. Instead, the unseparated term $\sigma_U = \sigma_{\mathrm{T}} + \epsilon\sigma_{\mathrm{L}}$ is extracted (see Equation 1.28). Therefore in the unpolarized case, only three cross-section parameters are extracted. For the polarized case (absolute beam spin asymmetry), one cross-section parameter $\sigma_{\mathrm{TL}'}$ is extracted. The unseparated term $\sigma_U = \sigma_{\mathrm{T}} + \epsilon\sigma_{\mathrm{L}}$ is shown in Figure 5.9 for kinematic 60-1 (top) and 60-3 (bottom). The red points are the results of this experiment, while the blue line is the prediction from the Goloskokov and Kroll (GK) transversity model [40]. The cyan band represents the systematic uncertainty. The values for all cross-section parameters at different kinematic bins can be found in Table B.1, Appendix B.

Before comparing our results directly with the Goloskokov and Kroll model, one should keep in mind that the model calculations are totally based on the data at low x_B

(0.36) and low t (about 0.3 GeV^2) due to the limitation on the availability of data at large t and x_B. However, our results at high x_B of 0.60 and high t about 1 GeV^2 will be very useful to improve the model [101]. With this fact in mind, we can now discuss some findings of our results.

The systematic disagreement in σ_U (see Figure 5.9), between our data and the Goloskokov and Kroll model, which assumes the negligible contribution from longitudinally polarized photons, hints that σ_{L} might be underestimated in this model. From the perspective of GPDs, this can be important in the sense that factorization is only proven from longitudinally polarized virtual photons, and if σ_{L} has a significant contribution to the total cross-section, it still opens the possibility to extract the GPDs with a regular factorization scheme. The other source of this disagreement in σ_U could be from the Goloskokov and Kroll model under predicting the contribution from σ_{T}. In the latter case, σ_{T} would still dominate the cross-section like it was observed at smaller Q^2 (see Figure 1.13). In that case, the transversity GPDs can be extracted but has to rely on the model-dependent factorization scheme either suggested by Goloskokov and Kroll or by Goldstein, Hernandez and Luiti.

The extracted result for cross-section parameter σ_{TL} (see Figure 5.10) is more exciting. Our result is consistent in sign with the previous π^0 result from Hall A [37] (see Figure 1.13), at the low x_B (0.36) and Q^2 (about 2 GeV^2). Our results are significantly different from the Goloskokov and Kroll model prediction, both in sign and magnitude. This can be interpreted as a hint that the Goloskokov and Kroll model is under predicting the contribution from σ_{L}.

The Goloskokov and Kroll model is able to predict the cross-section parameter σ_{TT} (see Figure 5.11) fairly well in our kinematics. It suggest that in the kinematic regime we explored, σ_{T} has a sizable contribution in exclusive π^0 production. This can be a strong

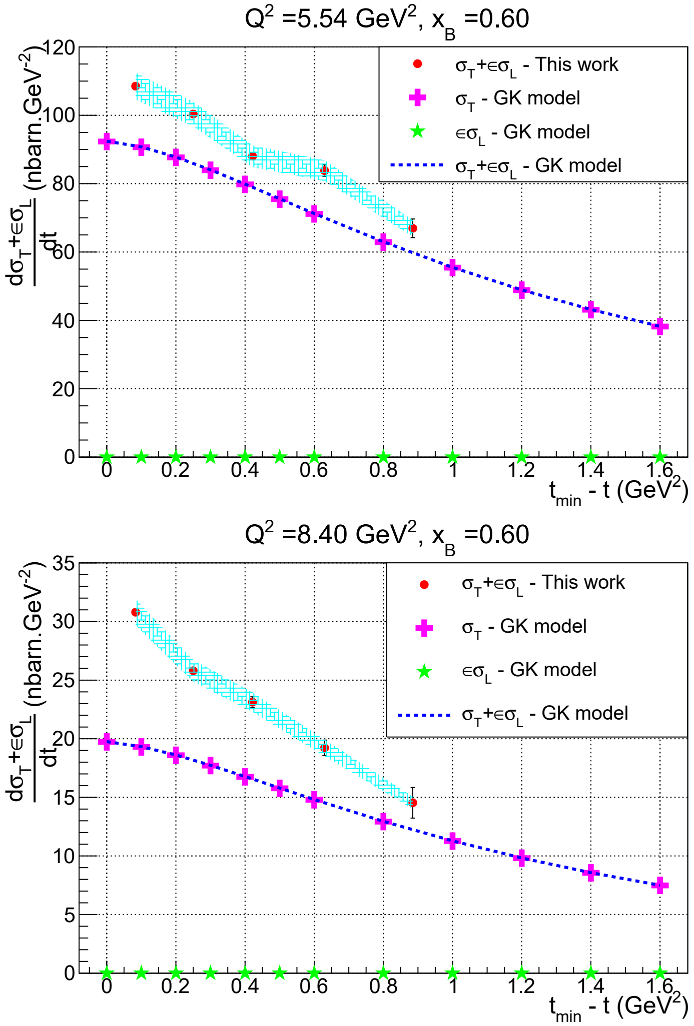

Figure 5.9: The extracted unseparated cross-section parameters for kinematic 60-1 (top) and 60-3 (bottom). The red points are the results of this experiment with their statistical error bar. The cyan band represents the systematic uncertainty. The blue dotted line is the prediction from the Goloskokov and Kroll (GK) model. The GK model predicts an almost negligible contribution from the longitudinally polarized virtual photons.

motivation to further improve the existing models that can factorize the contribution of the transversely polarized virtual photon in handbag formalism.

The measured absolute beam spin asymmetry is small with large statistical error bars for both kinematics 60-1 and 60-3 (see Figure 5.12 top and bottom respectively). We can not infer much besides giving fairly wide limits on the asymmetry values.

5.8 Conclusion

Generalized Parton Distributions can improve our understanding of the quark and gluon structure of the nucleon. In the future, it can potentially give access to the orbital angular momentum of the quarks. This information can be crucial to understand the spin structure of the nucleon.

GPDs can be accessed through exclusive channels like DVCS and DVMP. This document was focused on exclusive π^0 production (ep$\rightarrow$ $e'p'\pi^0$). We took data between 2014 -2016 in experimental Hall A, Jefferson Lab. Our data covered a wide range of kinematics. We scanned three different Bjorken-x at valence regime (x_B= 0.36, 0.48, and 0.60). For each of x_B setting, we covered at least two different Q^2 settings. The Q^2 range of our data was roughly 2 to 9 GeV^2. However, I analyzed only two different kinematics settings [Q^2 = 5.54 GeV^2 , x_B=0.60] and [Q^2 = 8.40 GeV^2 , x_B=0.60]. These are the first results at such a high x_B and Q^2. Our overall precision on absolute cross-section is about 5%.

Next, I will pose my research question and discuss how my result can justify it. In the end, I will discuss what is the future of these types of studies.

- Does the QCD factorization prediction ($\sigma_{\rm L}$ >> $\sigma_{\rm T}$) hold at large Q^2?

  The factorization is valid for only longitudinally polarized virtual photons at sufficiently high Q^2. The QCD factorization predicts the dominance of $\sigma_{\rm L}$ over $\sigma_{\rm T}$. As long as this prediction holds, the GPDs can be extracted from deep exclusive π^0 production. However, the previous π^0 results, limited to small Q^2 and x_B, had a strong disagreement with the QCD factorization prediction. One of our goals is to extend

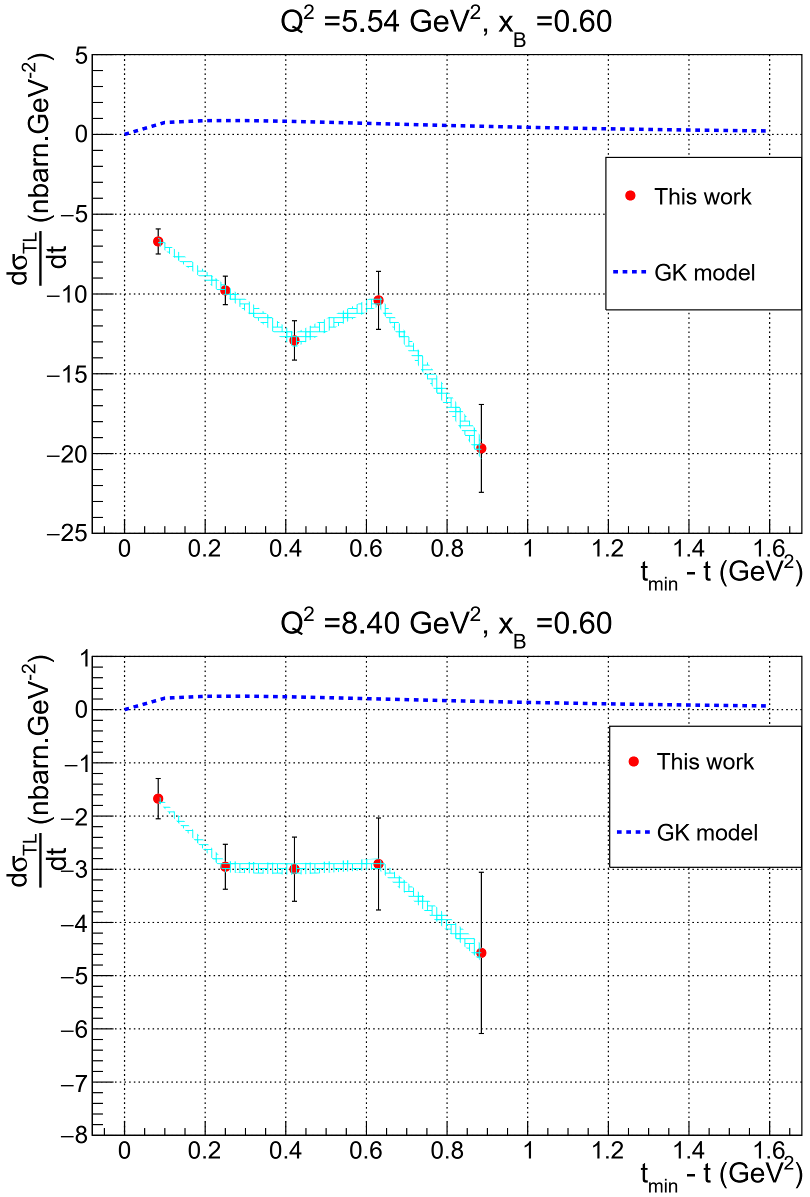

Figure 5.10: The extracted interference term σ_{TL} in the unpolarized cross-section for kinematic 60-1 (top) and 60-3 (bottom). The experimentally extracted cross-section parameter is opposite in sign as compared to the Goloskokov and Kroll model prediction.

the data to higher Q^2 and x_B to test if the factorization prediction is observed at higher Q^2. The extracted cross-section term σ_{TT} is relatively large. This might be a strong

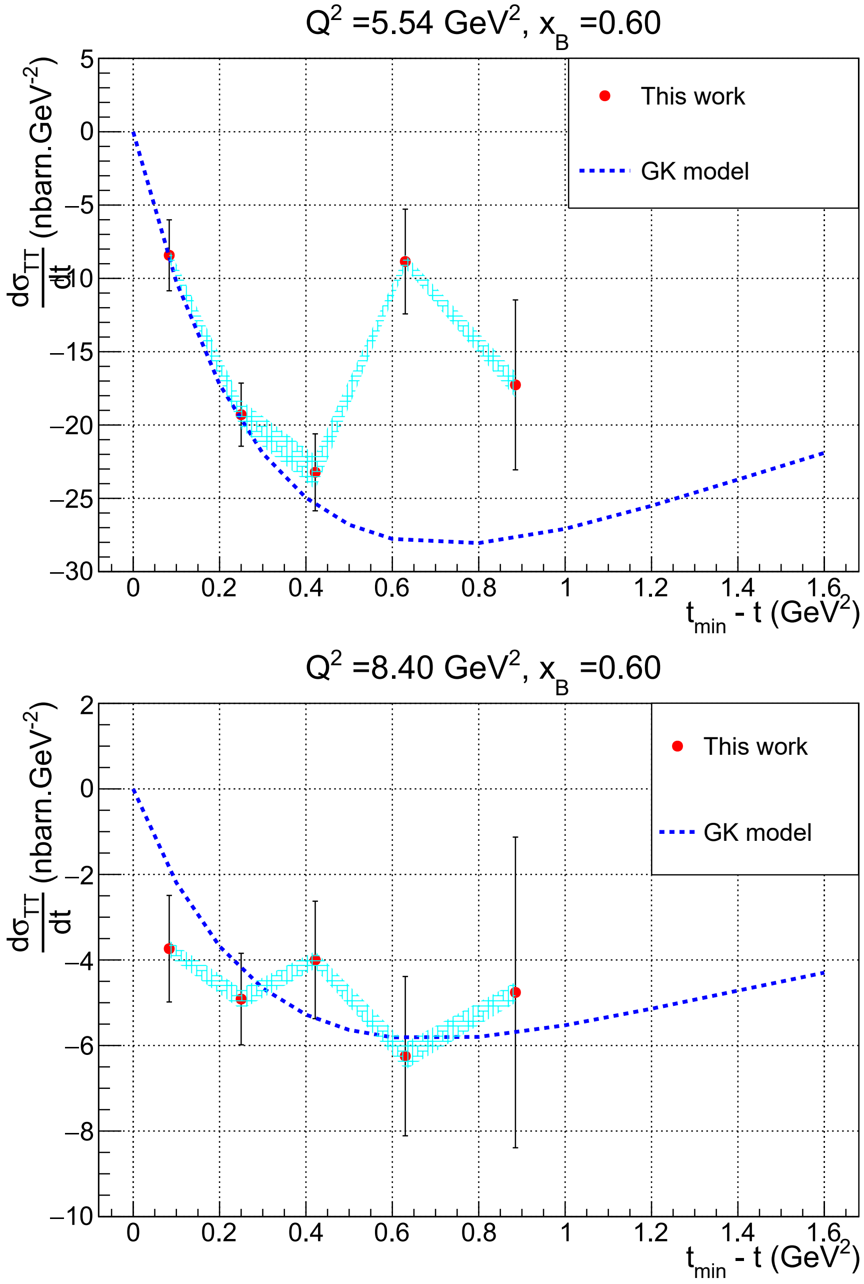

Figure 5.11: The extracted interference term σ_{TT} in the unpolarized cross-section for kinematic 60-1 (top) and 60-3 (bottom). The experimentally extracted cross-section parameter is in fair agreement with the Goloskokov and Kroll model prediction.

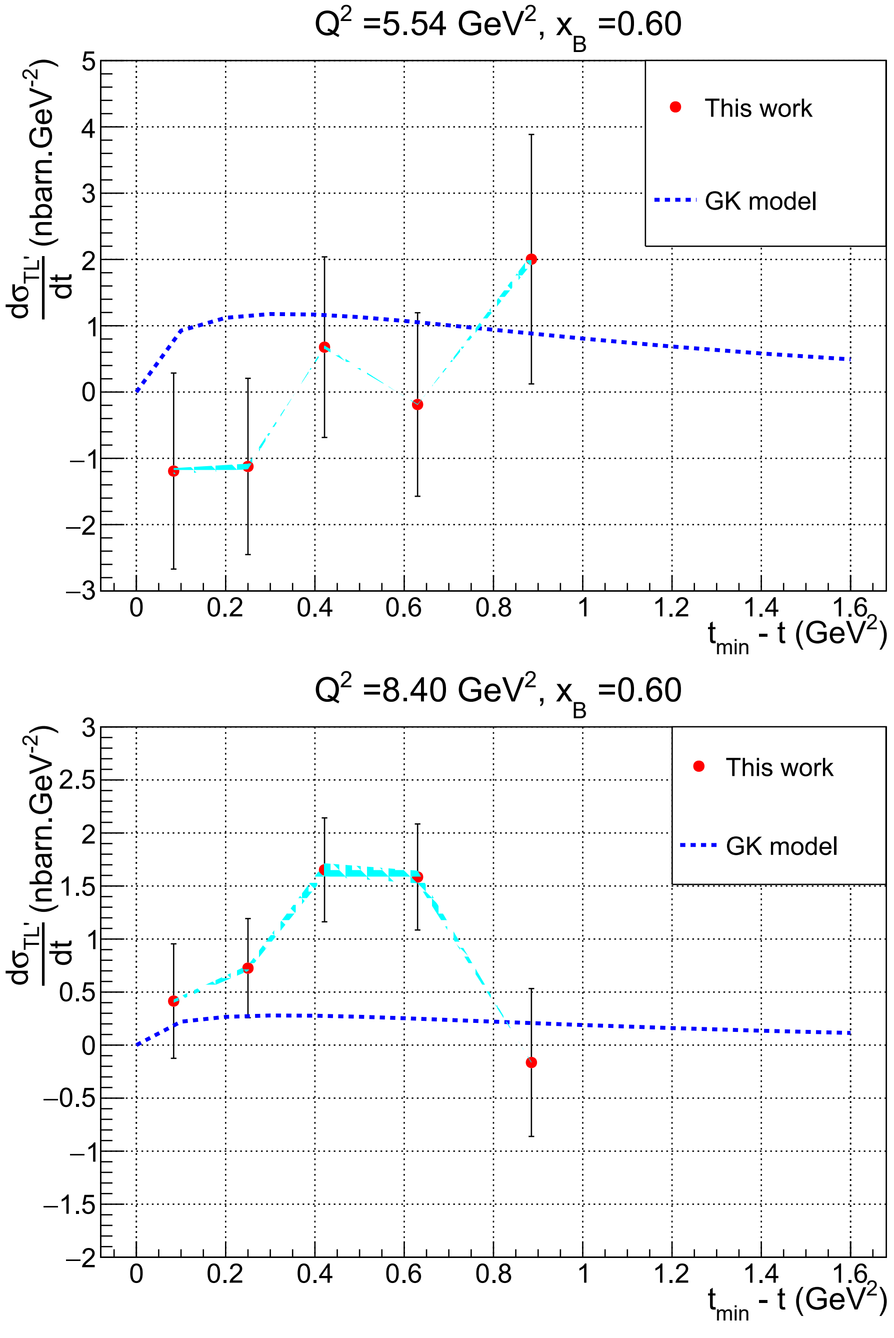

Figure 5.12: The polarized cross-section term for kinematic 60-1 (top) and 60-3 (bottom). Our results consist of large statistical error bar.

hint that even up to Q^2 of 8.5 GeV^2 there is a sizable contribution from transversely polarized virtual photons. O the other hand, the significant difference between the Goloskokov and Kroll model and the data for the cross-section term σ_{TL} suggests, there can be larger contributions from longitudinally polarized virtual photons than the model predicts. In the end, it can be concluded that the contribution from both the longitudinally and transversely polarized virtual photons are significant. Integrating all the results from exclusive π^0 production ranging from Q^2 1.5 to about 9 GeV^2 at different x_B (0.36, 0.48, and 0.6), we can not find a kinematic regime where the QCD factorization prediction holds i.e, $\sigma_{\mathrm{L}} >> \sigma_{\mathrm{T}}$.

- How good are current existing models for transversity GPDs?

  The transversity GPDs models are so far the only way to extract the GPDs from the existing data with dominance of transversely polarized virtual photons in the exclusive meson production cross-section. These models have an effective way to factorize the contribution from transverse photons and explains the sizable contribution of σ_{T} [40] [39]. Out of two existing models, I could only compare my result with the model from Goloskokov and Kroll. The calculation from another model, Goldstein, Hernandez and Luiti, is still in work. Both of these models were fair enough to explain the data at low Q^2. The comparison between the Goloskokov and Kroll model prediction and our results is encouraging, given the fact that Goloskokov and Kroll prediction was based on the available data at small x_B and small t but our data are at large x_B and t. This result provides a strong motivation to further improve the transversity GPDs models. Our data can be very important in improving the existing transversity GPDs model [101].

- Can we extract GPDs through exclusive π^0 production?

In order to connect the experimental measured cross-section for exclusive processes with GPDs, the factorization is essential. In our kinematic regime, neither the regular QCD factorization is applicable nor can we solely rely on transversity GPD models that can factorize the observed dominance of transversely polarized virtual photons. GPDs can not be reliably extracted from our exclusive π^0 production data.

To make a significant improvement in data interpretation, the future experiments should aim to measure the L/T separated cross-section terms. These measurements can lead to two possible outcomes. First, σ_{L} maybe sufficiently large so that GPDs can be extracted from the exclusive π^0 production channel using the regular QCD factorization. Second, if σ_{L} is not large enough or σ_{T} is sufficiently large, then we have to rely on the factorization scheme as suggested by transversity models to factorize the contribution from transversely polarized virtual photons. But for the latter scenario first the observed cross-section data should be explained by the models, only then we can move forward to extract the GPDs.

Recently a proposal for a new experiment in Hall C, Jefferson Lab has been accepted [59] to measure L/T separated cross-section parameters σ_{L} and σ_{T} in π^0. The proposed Electron-Ion Collider facility posses a unique potential to explore the nucleon structure through GPDs and can explain the role of gluons and sea quarks. In the theoretical front, some work is needed to improve the existing transversity GPDs model.

In this document, I showed my analysis for the kinematic with Bjorken-x (x_B=0.60), but the other kinematics (x_B=0.36 and x_B=0.48) were analyzed by other member from the DVCS collaborations (M. Dlamini, S. Ali, Po-Ju Lin, and Ho-San). The same experiment also measured the DVCS cross-section. Other members from DVCS collaboration (F. Georges, A. Johnson, and H. Rashad) were involved in DVCS cross-section analysis. The results for DVCS cross-sections can be found in F. Georges's thesis [81].

REFERENCES

[1] X.-D. Ji, Phys. Rev. Lett. **78**, 610 (1997), arXiv:hep-ph/9603249 [hep-ph] .

[2] D. Müller, D. Robaschik, B. Geyer, F. M. Dittes, and J. HoÅejÅi, Fortsch. Phys. **42**, 101 (1994), arXiv:hep-ph/9812448 [hep-ph] .

[3] A. V. Radyushkin *et al.*, Phys. Rev. **D56**, 5524 (1997), arXiv:hep-ph/9704207 [hep-ph] .

[4] D. Geesaman, "Reaching for the Horizon: The Nuclear Science Advisory Committee 2015 Long Range Plan for Nuclear Science," (2016), https://doi.org/10.1080/10619127.2016.1140967 .

[5] R. Hofstadter, Rev. Mod. Phys. **28**, 214 (1956).

[6] M. N. Rosenbluth, Phys. Rev. **79**, 615 (1950).

[7] Z. Ye, J. Arrington, R. J. Hill, and G. Lee, Physics Letters B **777**, 8 (2018).

[8] R. Pohl, R. Gilman, G. A. Miller, and K. Pachucki, Ann. Rev. Nucl. Part. Sci. **63**, 175 (2013), arXiv:1301.0905 [physics.atom-ph] .

[9] A. Bodek *et al.*, Phys. Rev. **D20**, 1471 (1979).

[10] A. Accardi, L. T. Brady, W. Melnitchouk, J. F. Owens, and N. Sato, Physical Review D **93**, 114017 (2016).

[11] F. Myhrer and A. Thomas, Journal of Physics G-nuclear and Particle Physics - J PHYS G-NUCL PARTICLE PHYS **37** (2010), 10.1088/0954-3899/37/2/023101.

[12] R. D. Ball, S. Forte, A. Guffanti, E. R. Nocera, G. Ridolfi, and J. Rojo (NNPDF), Phys. Lett. **B728**, 524 (2014), arXiv:1310.0461 [hep-ph] .

[13] E. Wigner, Phys. Rev. **40**, 749 (1932).

[14] H.-W. Lee, Physics Reports **259**, 147 (1995).

[15] C. Lorce and B. Pasquini, Phys. Rev. **D84**, 014015 (2011), arXiv:1106.0139 [hep-ph] .

[16] D. Sivers, Phys. Rev. D **41**, 83 (1990).

[17] B. Pasquini and F. Yuan, Phys. Rev. **D81**, 114013 (2010), arXiv:1001.5398 [hep-ph] .

[18] M. Burkardt and B. Pasquini, Eur. Phys. J. **A52**, 161 (2016), arXiv:1510.02567 [hep-ph] .

[19] M. Diehl, Phys. Rept. **388**, 41 (2003), arXiv:hep-ph/0307382 [hep-ph] .

[20] J. C. Collins and A. Freund, Phys. Rev. **D59**, 074009 (1999), arXiv:hep-ph/9801262 [hep-ph] .

[21] X. Ji and J. Osborne, Phys. Rev. D **58**, 094018 (1998).

[22] M. Defurne *et al.*, Nature Commun. **8**, 1408 (2017), arXiv:1703.09442 [hep-ex] .

[23] M. Guidal, H. Moutarde, and M. Vanderhaeghen, Rept. Prog. Phys. **76**, 066202 (2013), arXiv:1303.6600 [hep-ph] .

[24] M. V. Polyakov, Phys. Lett. **B555**, 57 (2003), arXiv:hep-ph/0210165 [hep-ph] .

[25] A. V. Belitsky, D. Mueller, and A. Kirchner, Nucl. Phys. **B629**, 323 (2002), arXiv:hep-ph/0112108 [hep-ph] .

[26] A. Bacchetta, U. D'Alesio, M. Diehl, and C. A. Miller, Phys. Rev. D **70**, 117504 (2004).

[27] J. J. Kelly, Phys. Rev. C **70**, 068202 (2004).

[28] K. Kumeriki and D. Müller, EPJ Web Conf. **112**, 01012 (2016), arXiv:1512.09014 [hep-ph] .

[29] M. Burkardt, Phys. Lett. **B595**, 245 (2004), arXiv:hep-ph/0401159 [hep-ph] .

[30] X. Ji, Ann. Rev. Nucl. Part. Sci. **54**, 413 (2004).

[31] A. Ekstedt, H. Ghaderi, G. Ingelman, and S. Leupold, "Towards solving the proton spin puzzle," (2018), arXiv:1808.06631 [hep-ph] .

[32] A. Accardi *et al.*, Eur. Phys. J. **A52**, 268 (2016), arXiv:1212.1701 [nucl-ex] .

[33] V. D. Burkert, L. Elouadrhiri, and F. X. Girod, Nature **557**, 396 (2018).

[34] L. Favart, M. Guidal, T. Horn, and P. Kroll, The European Physical Journal A **52**, 158 (2016).

[35] S. V. Goloskokov and P. Kroll, Eur. Phys. J. **C65**, 137 (2010), arXiv:0906.0460 [hep-ph] .

[36] K. Goeke, M. V. Polyakov, and M. Vanderhaeghen, Prog. Part. Nucl. Phys. **47**, 401 (2001), arXiv:hep-ph/0106012 [hep-ph] .

[37] M. Defurne *et al.* (Jefferson Lab Hall A Collaboration), Phys. Rev. Lett. **117**, 262001 (2016).

[38] I. Bedlinskiy *et al.* (CLAS), Phys. Rev. **C95**, 035202 (2017), arXiv:1703.06982 [nucl-ex] .

[39] S. Ahmad, G. R. Goldstein, and S. Liuti, Phys. Rev. D **79**, 054014 (2009).

[40] S. V. Goloskokov and P. Kroll, Eur. Phys. J. **A47**, 112 (2011), arXiv:1106.4897 [hep-ph] .

[41] N. d'Hose, S. Niccolai, and A. Rostomyan, Eur. Phys. J. **A52**, 151 (2016).

[42] E.-C. Aschenauer, S. Fazio, K. Kumericki, and D. Mueller, JHEP **09**, 093 (2013), arXiv:1304.0077 [hep-ph] .

[43] A. Aktas *et al.* (H1), Eur. Phys. J. **C44**, 1 (2005), arXiv:hep-ex/0505061 [hep-ex] .

[44] S. Chekanov *et al.* (ZEUS), Phys. Lett. **B573**, 46 (2003), arXiv:hep-ex/0305028 [hep-ex] .

[45] F. D. Aaron *et al.*, Journal of High Energy Physics **2010**, 32 (2010).

[46] S. Chekanov *et al.* (ZEUS), Nucl. Phys. **B695**, 3 (2004), arXiv:hep-ex/0404008 [hep-ex] .

[47] J. Breitweg *et al.* (ZEUS), Phys. Lett. **B487**, 273 (2000), arXiv:hep-ex/0006013 [hep-ex] .

[48] S. V. Goloskokov and P. Kroll, Eur. Phys. J. **C53**, 367 (2008), arXiv:0708.3569 [hep-ph] .

[49] A. Airapetian *et al.* (HERMES), Phys. Rev. **D75**, 011103 (2007), arXiv:hep-ex/0605108 [hep-ex] .

[50] A. Airapetian *et al.* (HERMES), JHEP **07**, 032 (2012), arXiv:1203.6287 [hep-ex] .

[51] A. Airapetian *et al.* (HERMES), JHEP **06**, 066 (2008), arXiv:0802.2499 [hep-ex] .

[52] A. Airapetian *et al.* (HERMES), Nucl. Phys. **B842**, 265 (2011), arXiv:1008.3996 [hep-ex] .

[53] A. Airapetian *et al.* (HERMES), Phys. Lett. **B659**, 486 (2008), arXiv:0707.0222 [hep-ex] .

[54] S. Stepanyan *et al.* (CLAS), Phys. Rev. Lett. **87**, 182002 (2001), arXiv:hep-ex/0107043 [hep-ex] .

[55] H. S. Jo *et al.* (CLAS Collaboration), Phys. Rev. Lett. **115**, 212003 (2015).

[56] M. G. Alexeev *et al.* (COMPASS), "Measurement of the cross section for hard exclusive π^0 leptoproduction," (2019), arXiv:1903.12030 [hep-ex] .

[57] V. Yu. Alexakhin *et al.* (COMPASS), Eur. Phys. J. **C52**, 255 (2007), arXiv:0704.1863 [hep-ex] .

[58] T. Horn *et al.* (Jefferson Lab F(pi)-2), Phys. Rev. Lett. **97**, 192001 (2006), arXiv:nucl-ex/0607005 [nucl-ex] .

[59] S. D. Covrig *et al.*, “Exclusive Deeply Virtual Compton and Neutral Pion Cross-Section Measurements in Hall C,” (2013).

[60] C. M. Camacho *et al.*, Phys. Rev. Lett. **97**, 262002 (2006), arXiv:nucl-ex/0607029 [nucl-ex] .

[61] M. Mazouz *et al.* (Jefferson Lab Hall A), Phys. Rev. Lett. **99**, 242501 (2007), arXiv:0709.0450 [nucl-ex] .

[62] S. Fazio, in *Proceedings, 20th International Workshop on Deep-Inelastic Scattering and Related Subjects (DIS 2012): Bonn, Germany, March 26-30, 2012* (2012) pp. 381–384, [,381(2012)], arXiv:1212.3584 [nucl-th] .

[63] J. Roche *et al.*, “Measurements of the electron-helicity dependent cross-sections of deeply virtual compton scattering with CEBAF at 12-GeV,” (2006), arXiv:nucl-ex/0609015 [nucl-ex] .

[64] P. Adderley, M. Baylac, J. Clark, T. Day, J. Grames, J. Hanskneckt, M. Poelker and M. Stutzman, “Jefferson Lab Polarized Source ,” (2002).

[65] J. Dudek *et al.*, Eur. Phys. J. **A48**, 187 (2012), arXiv:1208.1244 [hep-ex] .

[66] O. Glamazdin et al., “Beam polarization: Raw results,” http://hallaweb.jlab.org/equipment/moller/raw_results.html (2016).

[67] J. Alcorn *et al.*, Nucl. Instrum. Meth. **A522**, 294 (2004).

[68] W. Barry *et al.*, “Basic noise considerations for CEBAF beam position monitors, ,” (1991).

[69] K.Unser, Nucl. Sci **NS 28**, 2344 (1981).

[70] Bishnu Karki, “Internal Note: BCMs and Charge for the experiment E12-06-114,” https://hallaweb.jlab.org/dvcslog/12+GeV/180911_234857/bcmUncertainity.pdf (2018).

[71] D. W. Higinbotham et al., “Determination of the Beam Energy,” https://www.jlab.org/indico/event/197/session/3/contribution/12/material/slides/0.pdf (2016).

[72] T. N. S. Gautam, *Precision Measurement of the Proton Magnetic Form Factor at High Q^2*, Ph.D. thesis, Hampton University (2019).

[73] D. Meekins, ”Hall A Target Configuration, Jefferson Lab Target Group,” (2016).

[74] Hashir Rashad, “Internal Note: DVCS3 Event Selection (HRS),” https://userweb.jlab.org/~mongi/DVCSMeeting_100317.pdf (2017).

[75] M. Tanabashi, K. Hagiwara, K. Hikasa, K. Nakamura, *et al.* (Particle Data Group), Phys. Rev. D **98**, 030001 (2018).

[76] M. Dlamini, *”Measurement of Hard Exlcusive Electroproduction of π^0 Meson Cross-Section in Hall A of JLab with CEBAF at 12 GeV”*, Ph.D. thesis, Ohio University (2018).

[77] C. Camacho, *”Photon and pions electroproduction at Jefferson Laboratory - Hall A”*, Ph.D. thesis, de l’ Universite Paris VI (2005).

[78] F. Feinstein (ANTARES), in *Proceedings, 3rd International Conference, Beaune, France, June 17-21, 2002:New developments in photodetection*, Vol. A504 (2003) pp. 258–261.

[79] M. Defurne, *”Photon and pions electroproduction at Jefferson Laboratory - Hall A”*, Ph.D. thesis, Universite Paris-SUD (2015).

[80] G. M. Hamad, *”Using the R-Function to Study the High-Resolution Spectrometer (HRS) Acceptance for the 12 GeV Era Experiment E12-06-114 at JLAB”*, Vol. Master Thesis (2017).

[81] F. Georges, *”Deeply Virtual Compton Scattering at Jefferson Lab”*, Ph.D. thesis, Universite Paris-SUD (2018).

[82] B. Hartmann, M. Berz, and H. Wollnik, Nuclear Instruments and Methods in Physics Research Section A: Accelerators, Spectrometers, Detectors and Associated Equipment **297**, 343 (1990).

[83] J. Arrington, “Introduction to SIMC,” https://hallaweb.jlab.org/wiki/images/0/07/Simc.pdf (2000).

[84] Alexa N. Johnson, “Internal Note:DIS result update,” https://hallaweb.jlab.org/dvcslog/12+GeV/181031_085738/ELOG_103118.pdf (2018).

[85] Internal Note: Alexa N. Johnson, “R-Function for Halll A L-HRS Acceptance,” https://hallaweb.jlab.org/dvcslog/12+GeV/161031_161903/1.pdf (2016).

[86] Bishnu Karki, “Internal Note: Target cut study with dummy target,” https://hallaweb.jlab.org/dvcslog/12+GeV/170410_175132/target_study_april12.pdf (2017).

[87] Hashir Rashad, “Internal Note: Tracking, VDC multi-cluster),” https://hallaweb.jlab.org/dvcslog/12+GeV/161108_074436/Multi_Clusters_DVCS.pdf (2017).

[88] Y.-S. Tsai, Phys. Rev. **122**, 1898 (1961).

[89] M. Vanderhaeghen, J. M. Friedrich, D. Lhuillier, D. Marchand, L. Van Hoorebeke, and J. Van de Wiele, Phys. Rev. **C62**, 025501 (2000), arXiv:hep-ph/0001100 [hep-ph] .

[90] M. E. Christy and P. E. Bosted, Phys. Rev. C **81**, 055213 (2010).

[91] L. M. Stuart and P. E. e. a. Bosted, Phys. Rev. D **58**, 032003 (1998).

[92] Paul King, "Internal Note:Effect of trigger timing on TriggerPatternWord," https://hallaweb.jlab.org/dvcslog/12+GeV/370 (2013).

[93] Bishnu Karki, "Internal Note: Correction for DVCS and DIS rates with missing events," https://hallaweb.jlab.org/dvcslog/12+GeV/180716_193047/WeeklyMettingDVCSJuly2018.pdf (2018).

[94] M. Eric Christy, "Extraction of inclusive cross-sections," https://hallcweb.jlab.org/DocDB/0008/000867/002/inclusive_analysis-2017-1.pdf (2017).

[95] Alexa N. Johnson, "Internal Note:Experimental DIS cross-section," https://hallaweb.jlab.org/dvcslog/12+GeV/180116_091107/ELOG_011618_.pdf (2018).

[96] V. Breton, H. Fonvieille, P. Grenier, C. Guicheney, J. Jousset, Y. Roblin, and F. Tamin, Nucl. Instrum. Meth. **A362**, 478 (1995).

[97] S. Agostinelli *et al.* (GEANT4), Nucl. Instrum. Meth. **A506**, 250 (2003).

[98] R. Paremuzyan and M. Defurne, "Internal Note:Implementation of the Hall A DVCS calorimeter in GEANT4," https://userweb.jlab.org/rafopar/halla/calo/calogeant4.ps (2013).

[99] M. Mazouz, "Internal Note:Missing mass and Invariant mass distribution correlation," https://hallaweb.jlab.org/dvcslog/Pion/131 (2008).

[100] Bishnu Karki, "Internal Note: 5 Bin vs. 1 Bin Cross-section analysis," https://hallaweb.jlab.org/dvcslog/12+GeV/191010_154454/pions.pdf (2019).

[101] P. Kroll, "Comparison of data with GPDs based model," Private communication (2020).

APPENDIX A: ADDENDUM TO DVCS CROSS-SECTION

A.1 The Bethe-Heitler term

Here are the definition of the terms used in Equation 1.20

$$
\begin{aligned}
\mathcal{P}_1(\phi) &= -\frac{J + 2Kcos(\phi)}{y(1+\epsilon^2)}, \\
\mathcal{P}_2(\phi) &= 1 + \frac{t}{Q^2} + \frac{J + 2Kcos(\phi)}{y(1+\epsilon^2)}, \\
J &= \left(1 - y - \frac{y\epsilon^2}{2}\right)\left(1 + \frac{t}{Q^2}\right) - (1 - x_B)(2 - y)\frac{t}{Q^2}, \\
K^2 &= -\frac{\Delta^2}{Q^2}(1 - x_B)\left(1 - y - \frac{y^2\epsilon^2}{4}\right)\left(1 - \frac{\Delta^2_{min}}{\Delta^2}\right)\left(\sqrt{1+\epsilon^2} + \frac{4x_B(1-x_B) + \epsilon^2\Delta^2 - \Delta^2_{min}}{4(1-x_B)}\right), \\
-\Delta^2_{min} &\approx \frac{M^2x_B^2}{1 - x_B + x_BM^2/Q^2}
\end{aligned}
\tag{A.1}
$$

A.2 The DVCS term

The DVCS squared term can be expanded using Harmonic coefficients: c_n^{DVCS} and s_n^{DVCS}. These Harmonic coefficients are connected with the CFFs as described in following equations.

$$
\mid \mathcal{T}_{DVCS} \mid^2 = \frac{e^6}{y^2Q^2}\left\{\rfloor_0^{DVCS} + \sum_{n=1}^{2}\left[\rfloor_n^{DVCS} cos(n\phi) + \rfloor_n^{DVCS} sin(n\phi)\right]\right\} \tag{A.2}
$$

Before starting the connection I will describe some terms:

$$
t_{min} = -Q^2\frac{2\,(1-x_B)\left(1 - \sqrt{1+\epsilon^2}\right) + \epsilon^2}{4x_B((1-x_B) + \epsilon^2} \tag{A.3}
$$

$$
t_{max} = Q^2\frac{2\,(1-x_B)\left(1 + \sqrt{1+\epsilon^2}\right) + \epsilon^2}{4x_B((1-x_B) + \epsilon^2} \tag{A.4}
$$

$$
\widetilde{\mathcal{K}} = \sqrt{(1-x_B)x_B + \frac{\epsilon^2}{4}}\sqrt{\frac{(t_{min} - t)(t - t_{max})}{Q^2}} \tag{A.5}
$$

Let $\mathcal{F}$ be the general notation for twist-2 CFFs such that $\mathcal{F} \in [\ \mathcal{H}, \mathcal{E}, \widetilde{\mathcal{H}}, \widetilde{\mathcal{E}}\ ]$ and the term $\mathcal{F}_{ab}$ a and b represent the helicity of initial and final photon.

$$\mathcal{F}_{++} = \mathcal{F} + \mathcal{O}\left(\frac{1}{Q^2}\right) \tag{A.6}$$

$$\mathcal{F}_{,+} = \frac{\sqrt{2}\widetilde{K}}{\sqrt{1+\epsilon^2}Q\left(2 - x_B + \frac{x_B t}{Q^2}\right)}\mathcal{F}^{eff} + \mathcal{O}\left(\frac{1}{Q^2}\right) + \mathcal{O}(\alpha_s) \tag{A.7}$$

$$\mathcal{F}_{-+} = \frac{\widetilde{K}^2}{2M^2\left(2 - x_B + \frac{x_B t}{Q^2}\right)}\mathcal{F}^{T} + \mathcal{O}\left(\frac{1}{Q^2}\right) \tag{A.8}$$

with $\mathcal{F}_T$ is the twist-2 gluon transversity CFFs and $\mathcal{F}^{eff}$, the effective twist-3 CFFs such that:

$$\mathcal{F}^{eff} = -2\xi\left(\frac{1}{1+\xi}\mathcal{F} + \mathcal{F}_{+}^{twist-3} - \mathcal{F}_{-}^{twist-3}\right) + \mathcal{O}\left(\frac{1}{Q^2}\right) + \mathcal{O}\left(\frac{\alpha_s}{Q^2}\right) \tag{A.9}$$

$\mathcal{F}_{+}^{twist-3}$ and $\mathcal{F}_{-}^{twist-3}$ are twist-3 CFFs.

The harmonic coefficients c_n^{DVCS} and s_n^{DVCS} are defined as:

$$c_0^{DVCS} = 2\left(\frac{2-2y+y^2+\frac{\epsilon^2}{2}y^2}{1+\epsilon^2}\right)\mathcal{C}^{DVCS}(\mathcal{F}_{++},\mathcal{F}_{++}^{*}|\mathcal{F}_{-+},\mathcal{F}_{-+}^{*}) + 8\left(\frac{1-y-\frac{\epsilon^2}{4}y^2}{1+\epsilon^2}\right)\mathcal{C}^{DVCS}(\mathcal{F}_{,+},\mathcal{F}_{,+}^{*}) \tag{A.10}$$

$$\begin{bmatrix} c_1^{DVCS} \\ s_1^{DVCS} \end{bmatrix} = \frac{4\sqrt{2}\sqrt{1-y-\frac{\epsilon^2 y^2}{4}}}{1+\epsilon^2}\begin{bmatrix} 2-y \\ \lambda y\sqrt{1+\epsilon^2} \end{bmatrix}\begin{bmatrix} \mathcal{R}e \\ \mathcal{I}m \end{bmatrix}\mathcal{C}^{DVCS}(\mathcal{F}_{,+}|\mathcal{F}_{++}^{*},\mathcal{F}_{-+}^{*}) \tag{A.11}$$

$$c_2^{DVCS} = 8\left(\frac{1-y-\frac{\epsilon^2}{4}y^2}{1+\epsilon^2}\right)\mathcal{R}e\,\mathcal{C}^{DVCS}(\mathcal{F}_{-+},\mathcal{F}_{++}^{*}) \tag{A.12}$$

$s_2^{DVCS} = 0;$

where $\lambda = \pm 1$ corresponds to beam helicity and $\mathcal{C}^{DVCS}(\mathcal{F}_{++},\mathcal{F}_{++}^{*}|\mathcal{F}_{-+},\mathcal{F}_{-+}^{*})$ and $\mathcal{C}^{DVCS}(\mathcal{F}_{,+}|\mathcal{F}_{++}^{*},\mathcal{F}_{-+}^{*}$ are incoherent sum of transverse helicity-flip and non-flip CFFs.

$$\mathcal{C}^{DVCS}(\mathcal{F}_{++},\mathcal{F}_{++}^{*}|\mathcal{F}_{-+},\mathcal{F}_{-+}^{*}) = \mathcal{C}^{DVCS}(\mathcal{F}_{++},\mathcal{F}_{++}^{*} + \mathcal{C}^{DVCS}(\mathcal{F}_{-+},\mathcal{F}_{-+}^{*}) \tag{A.13}$$

$$\mathcal{C}^{DVCS}(\mathcal{F}_{\prime+}|\mathcal{F}^{*}_{++},\mathcal{F}^{*}_{-+}) = \mathcal{C}^{DVCS}(\mathcal{F}_{\prime+},\mathcal{F}^{*}_{++} + \mathcal{C}^{DVCS}(\mathcal{F}_{\prime+},\mathcal{F}^{*}_{-+}) \tag{A.14}$$

Now the bi-linear combination of CFFs $\mathcal{C}^{DVCS}(\mathcal{F},\mathcal{F})$ is given as:

$$\begin{aligned}
\mathcal{C}^{DVCS}(\mathcal{F},\mathcal{F}^{*}) \quad = \quad & \frac{4(1-x_B)(1+\frac{x_B t}{Q^2})}{2-x_B+\frac{x_B t}{Q^2}}[\mathcal{H}\mathcal{H}^{*}+\widetilde{\mathcal{H}}\widetilde{\mathcal{H}}^{*}] + \frac{2+\frac{t}{Q^2}\epsilon^2}{(2-x_B+\frac{x_B t}{Q^2})^2}\widetilde{\mathcal{H}}^{*} + \frac{t}{4M^2}\mathcal{E}\mathcal{E}^{*} \\
& - \frac{x_B^2}{(2-x_B+\frac{x_B t}{Q^2})^2}\left[\left(1+\frac{t}{q^2}\right)[\mathcal{H}\mathcal{E}^{*}+\mathcal{E}\mathcal{H}^{*}+\mathcal{E}\mathcal{E}^{*}] + \widetilde{\mathcal{H}}\widetilde{\mathcal{E}}^{*} + \widetilde{\mathcal{E}}\widetilde{\mathcal{H}}^{*}\right. \\
& \left. + \frac{t}{4M^2}\widetilde{\mathcal{E}}\widetilde{\mathcal{E}}^{*}\right]
\end{aligned}$$

APPENDIX B: EXCLUSIVE π^0PRODUCTION CROSS-SECTION ANALYSIS

As discussed in chapter 4, cross-section terms for exclusive π^0 production are extracted by minimizing the χ^2 from the Equation 5.22. Data are divided into 5 different $t_{min} - t$ bins and for each $t_{min} - t$ bin there are 12 different ϕ, angle between leptonic and hadronic plane, bins. In this section, I will show the result from the minimization for each $t_{min} - t$ bin as the function of ϕ in degree. The left panel is comparison between the number of events from data, the black points, and simulation, the red bars. The right panel is the extracted total cross-section, the blue points, as the function of ϕ in degree, the red line is fit to the extracted cross-section. The value of reduced χ^2 are fairly good ranging between 0.8 -2.83.

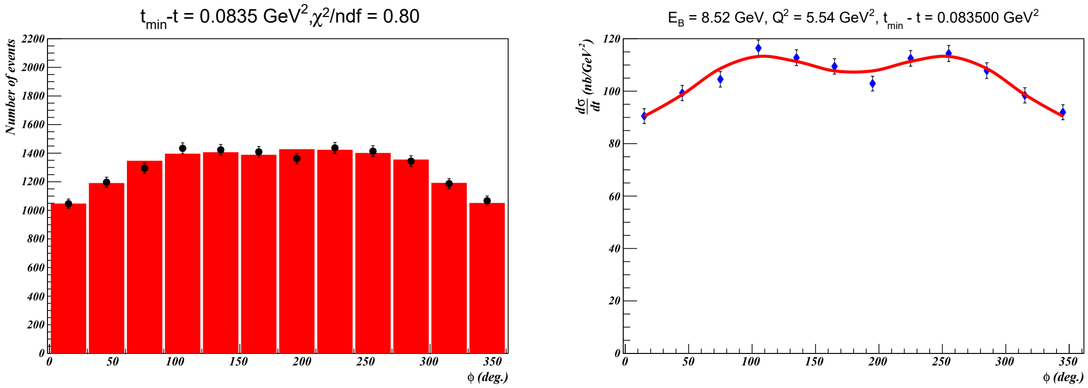

Figure B.1: For 1st $t_{min} - t$ bin at 0.0835 GeV^2

Table B.1: The experimental extracted cross-section terms for 60-1 and 60-3. For unseparated parameter both statistical (first) and systematic (second) errors are quoted. But for other cross-section parameters statistically error is quoted as it is larger relative to systematic error.

$\langle t_{min} - t \rangle$ (GeV^2)	$\frac{d(\sigma_{\mathrm{T}}+\epsilon\sigma_{\mathrm{L}})}{dt}$ (nb GeV^{-2})	$\frac{d\sigma_{\mathrm{TL}}}{dt}$ (nb GeV^{-2})	$\frac{d\sigma_{\mathrm{TT}}}{dt}$ (nb GeV^{-2})	$\frac{d\sigma_{\mathrm{TL'}}}{dt}$ (nb GeV^{-2})
Kinematic 60-1				
0.084	108.53 ± 0.75 ± 5.53	-6.71 ± 0.78	-8.43 ± 2.42	-1.19 ± 1.48
0.250	100.37 ± 0.87 ± 5.11	-9.78 ± 0.89	-19.29 ± 2.15	-1.12 ± 1.33
0.422	88.02 ± 1.13 ± 4.48	-12.91 ± 1.23	-23.23 ± 2.62	0.68 ± 1.36
0.630	83.81 ± 1.67 ± 4.27	-10.39 ± 1.82	-8.85 ± 3.57	-0.19 ± 1.38
0.885	66.94 ± 2.72 ± 3.41	-19.67 ± 2.75	-17.26 ± 5.79	2.01 ± 1.88
Kinematic 60-3				
0.084	30.24 ± 0.30 ± 1.54	-1.64 ± 0.38	-3.67 ± 1.25	0.41 ± 0.54
0.25	25.34 ± 0.33 ± 1.29	-2.90 ± 0.42	-4.83 ± 1.07	0.71 ± 0.47
0.42	22.71 ± 0.46 ± 1.16	-2.94 ± 0.60	-3.93 ± 1.37	1.62 ± 0.49
0.63	18.88 ± 0.66 ± 0.96	-2.85 ± 0.86	-6.14 ± 1.86	1.56 ± 0.50
0.89	14.27 ± 1.31 ± 0.73	-4.49 ± 1.52	-4.67 ± 3.63	-0.16 ± 0.70

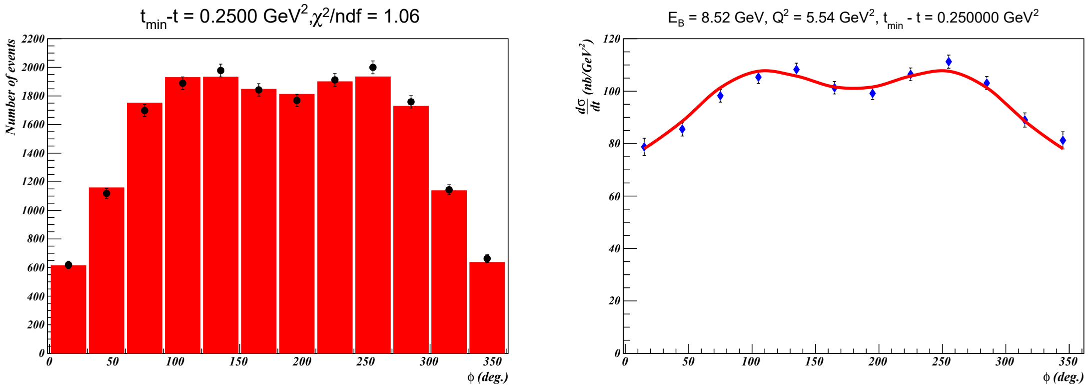

Figure B.2: For 2^{nd} $t_{min} - t$ bin at 0.2500 GeV^2

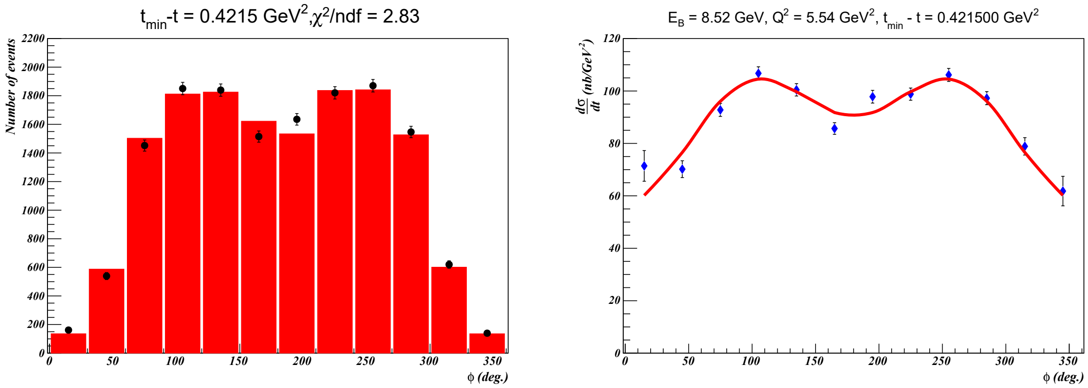

Figure B.3: For 3^{rd} $t_{min} - t$ bin at 0.4215 GeV^2

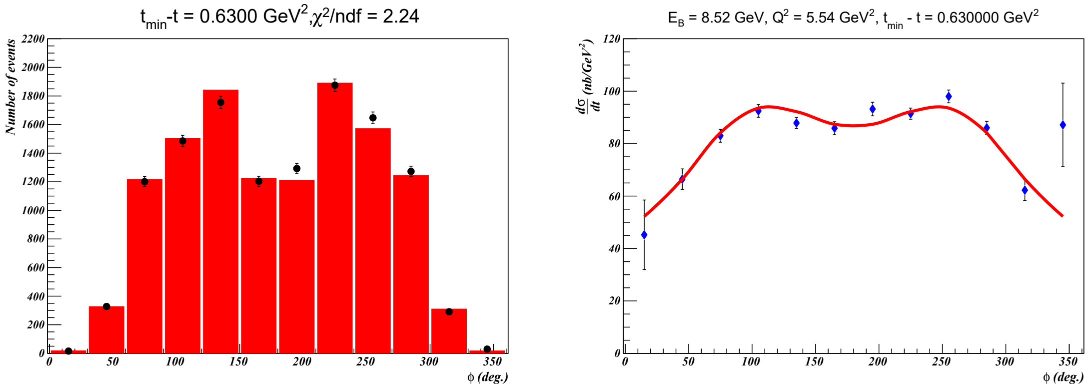

Figure B.4: For 4th $t_{min} - t$ bin at 0.6300 GeV^2

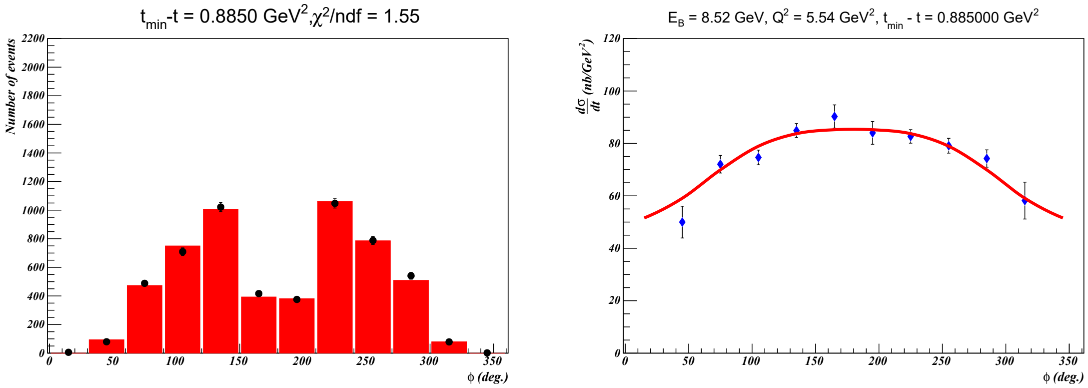

Figure B.5: For 5th $t_{min} - t$ bin at 0.8850 GeV^2

Now I will present the fitting result for Kinematic 603. For kinematic 603, the obtained χ^2 is fairly good.

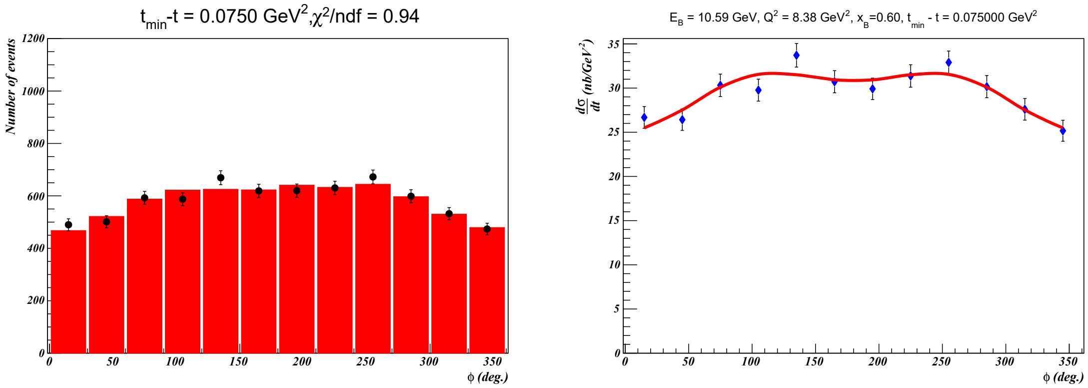

Figure B.6: For 1^{st} $t_{min} - t$ bin at 0.0750 GeV^2

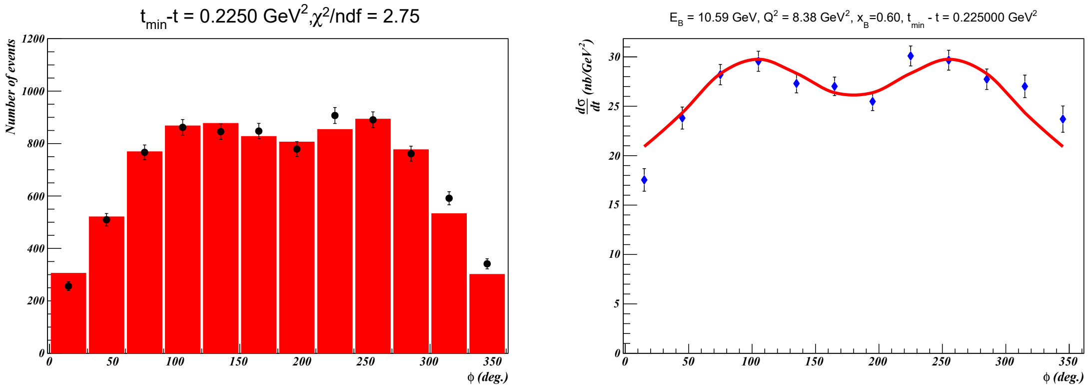

Figure B.7: For 2^{nd} $t_{min} - t$ bin at 0.2250 GeV^2

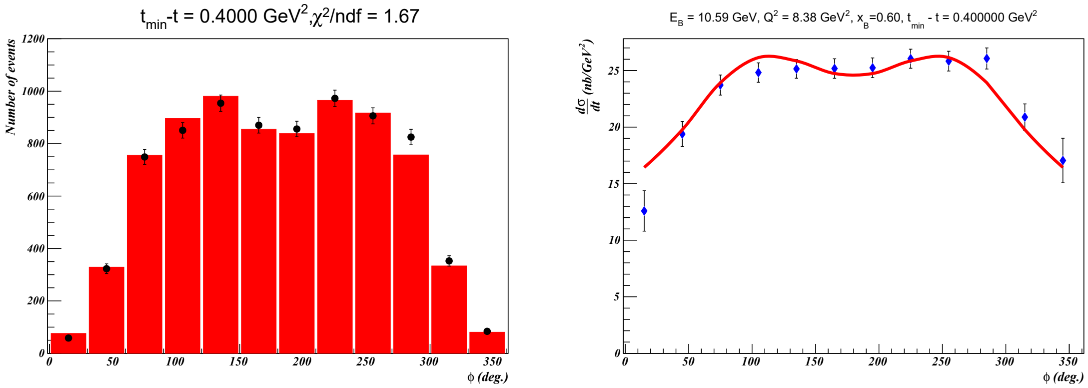

Figure B.8: For 3^{rd} $t_{min} - t$ bin at 0.4000 GeV^2

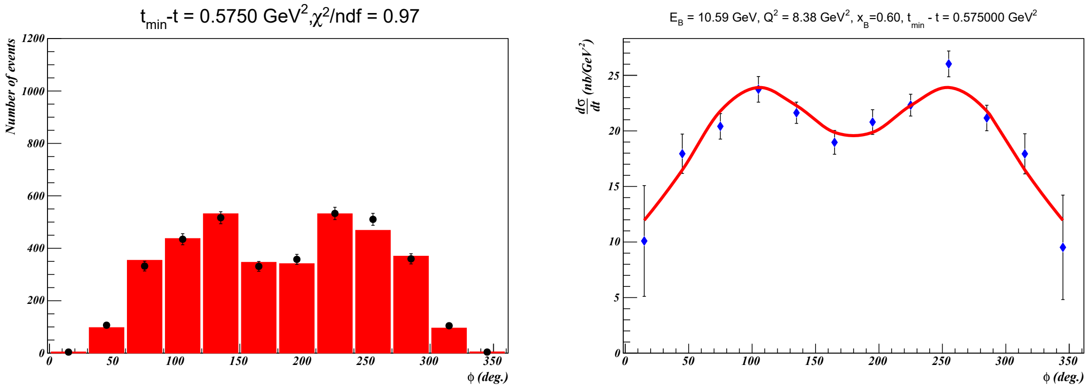

Figure B.9: For 4^{th} $t_{min} - t$ bin at 0.5750 GeV^2

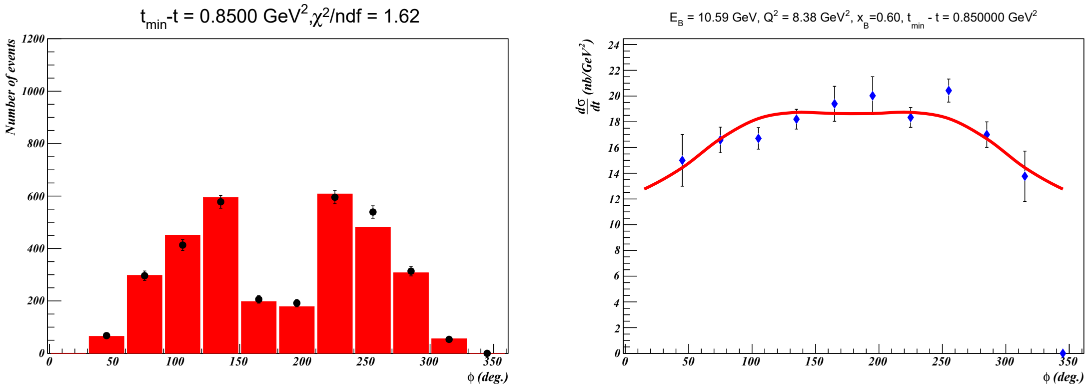

Figure B.10: For 5th $t_{min} - t$ bin at 0.8500 GeV^2

APPENDIX C: REPRINT PERMISSION AND LICENSES

1. Figure 1.4, DOI:10.1103/PhysRevD.93.114017, License date: 11-Nov-2019, License Number: **RNP/19/NoV/020234**

2. Figure 1.10, DOI:10.1103/PhysRevD.70.117504, License date: 11-Nov-2019, License Number: **RNP/19/NoV/020233**

3. Figure 1.11, Elsevier/Nuclear Phys B Proceedings, License date: 16-Feb-2020, License Number: **4771001027278**

4. Figure 1.12, Nature/Springer Nature, License date: 16-Feb-2020, License Number: **4771011123945**

5. Figure 1.13, DOI:10.1103/PhysRevLett.117.262001, License date: 20-Nov-2019, License Number: **RNP/19/NoV/020480**

6. Figure 1.14, Springer Nature, Journal of High Energy Physics, License date: 21-Nov-2019, License Number: **4713711116442**

7. Figure 1.15, DOI:10.1103/PhysRevC.95.035202, License date: 21-Nov-2019, License Number: **RNP/19/NoV/020514**

8. Figures 2.4, 3.1, Elsevier, Nuclear Instruments and Methods in Physics Research Section A, License date: 11-Dec-2019, License Number: **4726090892423**

Figure 1.4

Proton and neutron electromagnetic form factors and uncertainties

Author: Zhihong Ye,John Arrington,Richard J. Hill,Gabriel Lee
Publication: Physics Letters B
Publisher: Elsevier
Date: 10 February 2018

© 2017 Elsevier B.V.

Creative Commons Attribution-NonCommercial-No Derivatives License (CC BY NC ND)

This article is published under the terms of the Creative Commons Attribution-NonCommercial-No Derivatives License (CC BY NC ND).
For non-commercial purposes you may copy and distribute the article, use portions or extracts from the article in other works, and text or data mine the article, provided you do not alter or modify the article without permission from Elsevier. You may also create adaptations of the article for your own personal use only, but not distribute these to others. You must give appropriate credit to the original work, together with a link to the formal publication through the relevant DOI, and a link to the Creative Commons user license above. If changes are permitted, you must indicate if any changes are made but not in any way that suggests the licensor endorses you or your use of the work.

Permission is not required for this non-commercial use. For commercial use please continue to request permission via Rightslink.

© 2020 Copyright - All Rights Reserved | Copyright Clearance Center, Inc. | Privacy statement | Terms and Conditions
Comments? We would like to hear from you. E-mail us at customercare@copyright.com

Figure C.1: Permission to re-use the the Figure 1.2 which contains the Sach Form Factors

APPENDIX D: BCM CALIBRATION COEFFICIENTS

While experiment E12-06-114 was running I was the responsible for the BCM calibration. As stated in Chapter 2 the BCM calibration is two step process: the Unser calibration and BCM calibration. The Unser calibration coefficients during the different run period of the experiment E12-06-114 is reported in Table D.1. During the run period, Fall 2016 BCM, was calibrated two different times. The BCM calibration runs were 14252 and 14545. The combined analysis of these two BCM calibration runs was performed to extract the gains and offsets of each BCM receiver. Table D.2 shows the gains and coefficient for Fall 2016 run period.

Table D.1: Unser calibration coefficients for different run periods. In the Spring of 2016 and Fall of 2014 run periods, a part of Unser output was used for commissioning purpose of the upcoming experiment and rest part was sent to the electronic readout. But during Fall of 2016, the total output from Unser was sent to electronic readout. Due to this reason the gain of the Unser changed about 10% from Spring of 2016 to Fall of 2016.

Gain (10^{-6} μA/Hz)	Offset (μA)
Fall 2014	
2755 ± 7.25	0.17 ± 0.11
Spring 2016	
2753 ± 6.1	0.15 ± 0.12
Fall 2016	
2505 ± 4.59	0.16 ± 0.10

In case of Fall 2014, Hall A had only analog BCM receivers. The Fall 2014 run period was very small about 15 day, so BCM was only calibrated once. The BCM calibration run

Table D.2: The BCM calibration coefficients for six different receivers for Fall 2016 run period. The coefficients were extracted with combined analysis of two BCM calibration runs 14252 and 14545.

BCM	Gain (10^{-6} μA/Hz)	Offset (μA)
U1	384.84 ± 1.86	1.10 ± 0.11
D1	328.77 ± 1.59	0.62 ± 0.11
D3	97.05 ± 0.32	0.19 ± 0.06
D10	33.72 ± 0.22	0.3 ± 0.08
Dnew	224.23 ± 0.74	0.1 ± 0.06
Unew	255.50 ± 0.85	0.05 ± 0.06

for Fall 2014 is 10505. Table D.3 gives the gains and offsets for different BCM receivers during Fall 2014.

Table D.3: The BCM calibration coefficients for four different BCM receivers for Fall 2014 run period. The coefficients was extracted with BCM calibration run 10505.

BCM	Gain (10^{-6} μA/Hz)	Offset (μA)
U1	515.9 ± 9.99	0.56 ± 0.29
D1	454.53 ± 8.8	0.55 ± 0.22
D3	127.4 ± 1.6	0.39 ± 0.17
D10	45.65 ± 0.57	0.31 ± 0.17

For Spring 2016, the BCM was calibrated 4 different times. The gains of analog receivers were fairly stable so combined analysis using 4 BCM calibration runs: 12514,

Table D.4: The gain of the digital receivers were not stable, in order to use digital receiver the gains and offsets corresponding the specific calibration run should be used.

Run period	BCM calibration run used
12508-13015	12514 and 12916
13100-113261	13220
13279-13418	13447

12916, 13220, and 13447 was done. But in case of digital receiver, the gain were not stable so in order to use the digital receiver one need to use run specific calibration coefficients. Table D.4 gives the run interval and corresponding calibration run to be used for gain and offsets of digital receivers. The gain and offset of BCM receivers for Spring 2016 run period is given in Table D.5.

Table D.5: The BCM calibration coefficients for six different receivers for Spring 2016 run period. The coefficients were extracted with combined analysis of 4 different BCM calibration runs 12514, 12916, 13220, and 13447. However, digital BCMs were not stable, so global calibration would not be appropriate.

BCM	Gain (10^{-6} μA/Hz)	Offset (μA)
U1	351.17 ± 0.72	0.75 ± 0.06
D1	319.28 ± 0.65	0.41 ± 0.06
D3	93.09 ± 0.18	0.30 ± 0.05
D10	32.14 ± 0.18	0.19 ± 0.06
Digital receivers, calibration runs 12514 & 12916		
Dnew	172.15 ± 0.66	0.19 ± 0.06
Unew	199.25 ± 0.76	0.20 ± 0.06
Digital receivers, calibration run 13220		
Dnew	249.95 ± 1.41	0.10 ± 0.12
Unew	295.64 ± 1.66	0.20 ± 0.12
Digital receivers, calibration run 13447		
Dnew	42.94 ± 0.25	0.04 ± 0.12
Unew	50.05 ± 0.29	0.05 ± 0.12